Fluctuations Enhanced Sensing
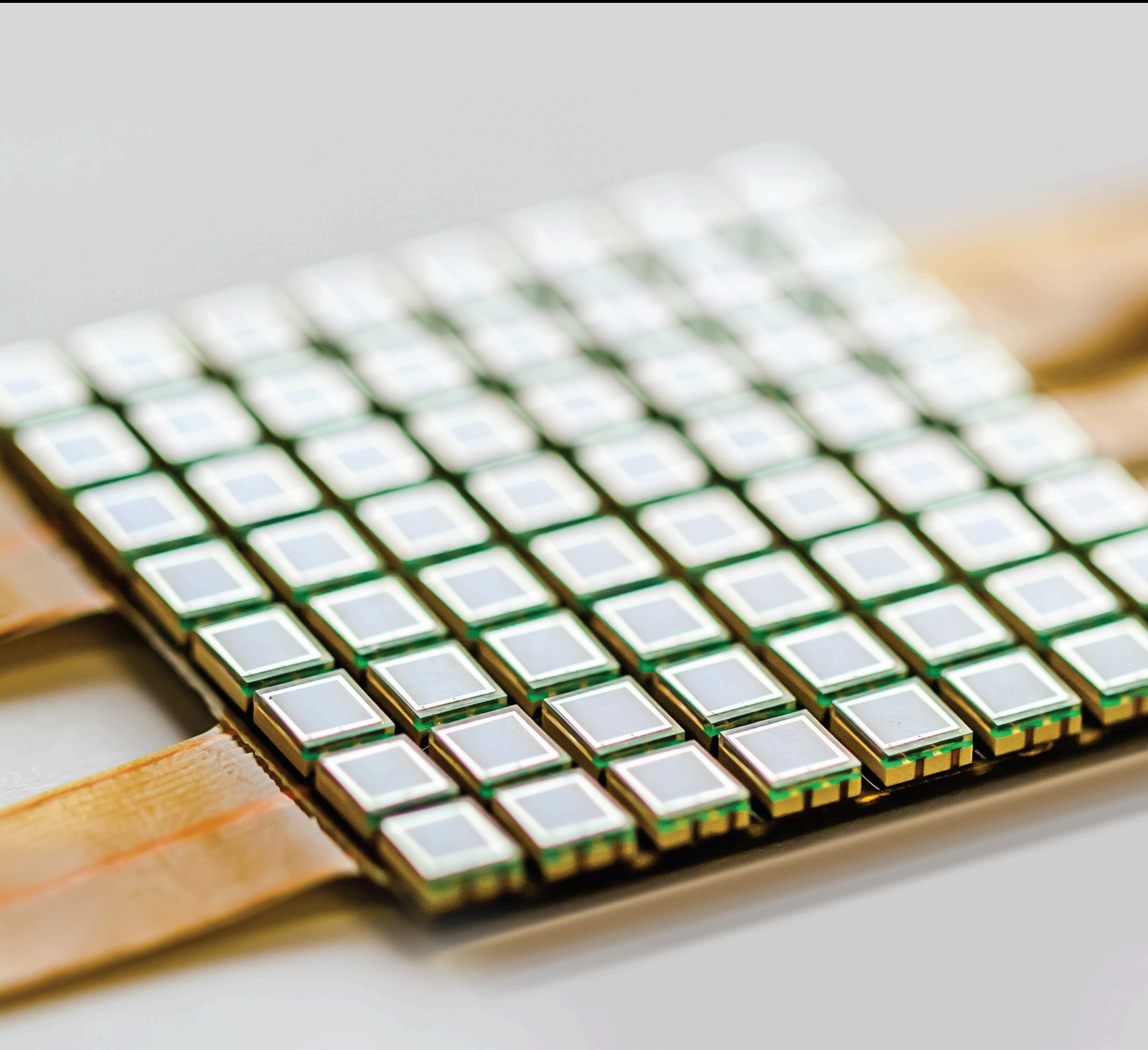
Lead Guest Editor: Graziella Scandurra
Guest Editors: Laszlo B. Kish and Janusz Smulko
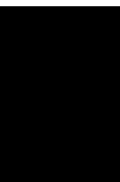
Fluctuations Enhanced Sensing

Fluctuations Enhanced Sensing

Lead Guest Editor: Graziella Scandurra
Guest Editors: Laszlo B. Kish and Janusz Smulko

Jerome Rossignol, France
Carlos Ruiz, Spain
Ylias Sabri, Australia
José P. Santos, Spain
Sina Sareh, United Kingdom
Isabel Sayago, Spain
Andreas Schütze, Germany
Praveen K. Sekhar, USA
Sandra Sendra, Spain
Pietro Siciliano, Italy
Vincenzo Spagnolo, Italy
Sachin K. Srivastava, India
Grigore Stamatescu, Romania
Stefano Stassi, Italy
Vincenzo Stornelli, Italy
Salvatore Surdo, Italy
Guiyun Tian, United Kingdom
Vijay Tomer, USA
Abdellah Touhafi, Belgium
Hoang Vinh Tran, Vietnam
Aitor Urrutia, Spain
Hana Vaisocherova - Lisalova, Czech
Republic
Everardo Vargas-Rodriguez, Mexico
Xavier Vilanova, Spain
Luca Vollero, Italy
Tomasz Wandowski, Poland
He Wen, China
Qihao Weng, USA
Penghai Wu, China
Qiang Wu, United Kingdom
Aijun Yin, China
Chouki Zerrouki, France

Contents

Editorial

Fluctuation-Enhanced Sensing

Graziella Scandurra [iD],[1] **Janusz Smulko** [iD],[2] **and Laszlo B. Kish** [iD][3]

[1]*Department of Engineering, University of Messina, Messina I-98166, Italy*
[2]*Department of Metrology and Optoelectronics, Gdańsk University of Technology, Gdańsk 80-233, Poland*
[3]*Department of Electrical and Computer Engineering, Texas A&M University, College Station, TX 77843-3128, USA*

Correspondence should be addressed to Graziella Scandurra; gscandurra@unime.it

Fluctuation-enhanced sensing (FES) is an exciting and relatively new research field that promises to extend the range of information that can be extracted from a single sensor. In FES, the stochastic fluctuations of the sensor signal, rather than its average value, are recorded and analyzed. Typical components of such fluctuations are due to interactions at the microscopic level. Proper statistical analysis provides optimum sensory information.

FES was used for the first time in the 90s, but it has not been commercially available yet because of the relatively limited amount of test data and the requirement of a special measurement setup. Sensor interface and instrumentation in a FES system have to be specifically designed to extract and amplify the low-frequency stochastic signal components, which are usually orders of magnitude weaker than the classical, deterministic sensor signal. Then, selected statistical properties of the amplified noise are analyzed in order to generate a corresponding pattern as a "stochastic fingerprint" of the sensed agent. The power spectral density of the noise signal is often used as an output pattern, but FES has been proven effective with higher-order statistics and other more advanced methods as well.

Many open questions must be addressed before FES can become a commercially available technique. Such issues include the design of highly sensitive instrumentation and the most effective data analysis, the development of working physical models for the interpretation of the stochastic data involving the sensor structure and sensing mechanisms, the selection of proper materials and structures, and finding sensing configuration for optimized sensitivity and selectivity.

Despite the challenges, FES exhibits a sensitivity of orders of magnitude higher than that of conventional electronic noses and tongues. Moreover, a single sensor can act as a complex high-dimensional electronic nose or tongue.

Therefore, it is important to enhance research activities and interactions in this subject. The purpose of this special issue is to turn the attention to the potentials of FES and to bring specialists together to reach the critical mass for a breakthrough in this field.

Because of the complexity of the topic, special attention was given to the papers including experimental data or results actually relevant for the future development of FES. After a rigorous peer-review process, 4 papers were accepted for publication in this special issue.

The paper by M. Piotto et al. proposes an original approach to model the noise density in sensors based on a single hot wire or pairs of thermally coupled wires. Since hot wires are used in a large variety of sensing devices and instruments, this study could give an important contribution to advanced sensor design. The model presented in this paper consists of an original combination of a previous electrothermal model of the wire with well-established assumptions on the thermal noise in conductors that carry moderate current densities. The model parameters can be easily determined by means of small-signal impedance measurements as a function of frequency. The effects of the electrothermal feedback of both hot wires and hot-wire pairs on flicker noise are also intrinsically covered by the proposed approach. The results showed in this work should contribute to widen the knowledge of noise in out-of-equilibrium electrical systems.

The paper by M. Macucci and P. Marconcini is focused on the noise properties of graphene, which is one of the principal materials for the realization of modern sensors whose ultimate performance is often right determined by the flicker noise of graphene. Indeed, graphene exhibits, compared to the vast majority of ordinary semiconductors, a peculiar behaviour of the flicker noise power spectral density as a function of the charge carrier density. In this paper, this difference is addressed and explained, and a comparison between graphene and other semiconducting materials is carried out. The conducted analysis, which clarifies the mechanisms that cause or prevent a reduction, at proper bias conditions, of the intrinsic sensor flicker noise, can be useful for the design of low-noise devices and in particular of high-sensitivity sensors.

The paper by G. Scandurra et al. proposes a new approach for the extraction of the equivalent parameters of quartz tuning forks (QTF) used as sensors by means of noise measurements. By means of spectral analysis, noise is used as the test signal for the determination of the frequency response of a circuit including the quartz tuning fork whose parameters need to be determined. A new approach for the analysis of strongly peaked noise spectra was developed in order to allow the correct measurement of the strongly peaked noise spectrum at the output of the system, which is the result of the high-quality factor of any quartz tuning fork-based sensor. With the proposed approach, the best compromise in terms of accuracy and measurement time can be obtained in a single measurement run. The ability to accurately estimate the PSD over a narrow bandwidth across the resonance frequency of a QTF-based sensor may facilitate the exploration of fluctuation-enhanced sensing (FES) with QTF-based sensors.

The paper by J. Smulko et al. presents experimental results of fluctuation-enhanced gas sensing by low-cost resistive sensors based on a mixture of graphene flakes and TiO_2 nanoparticles, both photocatalytic and activated by UV light. The sensors' response to two UV LEDs of different wavelengths was observed in an ambient atmosphere of synthetic air and toxic NO_2 at selected concentrations. It was observed that flicker noise changes its frequency dependence at different UV light wavelengths, thereby providing additional information about the ambient atmosphere, and that the power spectral density changes by a few times as a result of UV light irradiation. The sensors were operated at different temperatures, and the effect of UV light on gas sensing was most apparent at low operating temperature. In conclusion, UV light activates the gas sensing layer and improves gas detection at low concentrations of NO_2. This result is desirable for the detection of the components of gas mixtures, and the modulated sensor can replace an array of independent resistive sensors which would consume much more energy for heating. It is also suggested in the paper that a more advanced technology for preparing the gas sensing layer, by use of spin coating, will produce corresponding layers with thickness of about a few μm, which is about ten times less than that for the tested samples, and consequently, the effects induced by the applied UV light, having a penetration depth of only a few μm, would then be amplified. The presented results open a new perspective on enhanced gas sensing for emerging gas sensing materials.

Graziella Scandurra
Janusz Smulko
Laszlo B. Kish

Conflicts of Interest

The authors declare that there is no conflict of interest regarding the publication of this paper.

Research Article

UV Light-Modulated Fluctuation-Enhanced Gas Sensing by Layers of Graphene Flakes/TiO$_2$ Nanoparticles

Janusz Smulko [ID],[1] **Tomasz Chludziński,**[1] **Umut Çindemir,**[2] **Claes G. Granqvist,**[2] **and He Wen**[3]

[1]*Faculty of Electronics, Telecommunications and Informatics, Gdańsk University of Technology, Gdańsk 80-233, Poland*
[2]*Department of Materials Sciences and Engineering, The Ångström Laboratory, Uppsala University, SE-75121 Uppsala, Sweden*
[3]*College of Electrical and Information Engineering, Hunan University, Changsha, China*

Correspondence should be addressed to Janusz Smulko; janusz.smulko@pg.edu.pl

We present experimental results of fluctuation-enhanced gas sensing by low-cost resistive sensors made of a mixture of graphene flakes and TiO$_2$ nanoparticles. Both components are photocatalytic and activated by UV light. Two UV LEDs of different wavelengths (362 and 394 nm) were applied to modulate the gas sensing of the layers. Resistance noise was recorded at low frequencies, between 8 Hz and 10 kHz. The sensors' response was observed in an ambient atmosphere of synthetic air and toxic NO$_2$ at selected concentrations (5, 10, and 15 ppm). We observed that flicker noise changed its frequency dependence at different UV light wavelengths, thereby providing additional information about the ambient atmosphere. The power spectral density changed by a few times as a result of UV light irradiation. The sensors were operated at 60 and 120°C, and the effect of UV light on gas sensing was most apparent at low operating temperature. We conclude that UV light activates the gas-sensing layer and improves gas detection at low concentrations of NO$_2$. This result is desirable for the detection of the components of gas mixtures, and the modulated sensor can replace an array of independent resistive sensors which would consume much more energy for heating. We also suggest that a more advanced technology for preparing the gas-sensing layer, by use of spin coating, will produce corresponding layers with thickness of about a few μm, which is about ten times less than that for the tested samples. The effects induced by the applied UV light, having a penetration depth of only a few μm, would then be amplified.

1. Introduction

Resistive gas sensors are of much current interest because of their low-cost production and simple applications to detect a range of gases [1, 2]. A large variety of metal oxide semiconductors (MOSs)—such as SnO$_2$, WO$_3$, ZnO, TiO$_2$, MoO$_3$, NiO, and Fe$_2$O$_3$—exhibit different gas-sensing characteristics and can be used to detect various gases. The resistance is altered upon exposure to the ambient atmosphere. The change depends on the reducing or oxidizing ability of the gas molecules and can be employed to determine gas concentration.

The sensors are activated for gas detection at elevated temperature, and the operating temperature determines the selectivity and sensitivity of the MOS sensors. Nanoparticles,

typically of noble metals such as Au and Pt, can also dope the sensors and induce catalytic effects so as to further improve selectivity and sensitivity [3]. For some applications, a complicating aspect is that the gas mixture may contain different amounts of humidity, which is the case, e.g., for exhaled breath analysis for medical check-ups, in office environments, etc. One can improve gas detection by applying an array of MOS gas sensors with selectivity optimized for chosen gases, but this solution leads to additional costs of preparing the set of gas sensors and their operation during practical use. Furthermore, an array of gas sensors requires additional energy to operate at elevated temperature. Consequently, novel gas-sensing methods are desired for enhancing gas detection by low-cost MOS sensors and need to be applied beyond measuring the sensors' DC resistance.

One method for enhancing gas sensing utilizes low-frequency (low-f) resistance noise and was proposed about two decades ago [4, 5]. Specifically, this method was found to be efficient for improving selectivity and sensitivity; it makes use of power spectral densities of recorded resistance noise as an additional source of information about the ambient atmosphere of the gas sensor [5, 6]. This method is referred to as fluctuation-enhanced sensing (FES) [5]. Moreover, recorded $1/f$ noise can be easily modified by changing the operating temperature or by UV light irradiation onto photocatalytic materials [7].

Power spectral density is a function of frequency; its slope can change locally around a characteristic corner frequency $f_c = 1/2\pi\tau_c$ by adsorption-desorption events, of specific time constants τ_c, induced by the gas molecules present in the ambient atmosphere. A similar mechanism leading to $1/f$ noise is well known for generation-recombination (G-R) events in semiconductors. Each G-R event is described by a Lorentzian having a power spectral density of $S(f) = S_0/\{1 + (2\pi\tau f)^2\}$, where S_0 determines the noise intensity at frequencies $f < (2\pi\tau)^{-1}$ and τ is the time constant of the trapping state. The $1/f$ spectrum is given by summing up the independent events having time constants τ and distributed logarithmically between the limits τ_1 and τ_2 [8]. Any deviation from the assumed logarithmically distributed τ—e.g., due to scattering from charged impurities with specific properties—results in a local deviation from the $1/f$ dependence. The difference is usually observed as a plateau at a given corner frequency. Its intensity and position in the frequency domain may be characteristic for the adsorbed gas molecules and utilized for their identification by low-frequency noise measurements.

Experimental studies on a single-layer-graphene field-effect transistor (FET) have reported different corner frequencies of the plateau characteristic for a set of gases [9]. The corner frequency of the plateau was repeatable for a batch of specimens, thus demonstrating the potential of high gas selectivity for the FES method [10]. It was also observed that the graphene layer could be modulated—e.g., cleaned after gas exposure to remove adsorbed gas molecules [9]—by UV light. These results imply that one can use graphene for gas sensing and UV light irradiation to enhance its sensing properties.

In two-dimensional materials, such as graphene, the gas molecules adsorbed on the surface change the surface potential, whereas in resistive gas sensors, the gas molecules alter the potential barrier between grains. This barrier differs among the grains of various sizes which jointly form the resistive gas-sensing layer. Single-layer-graphene has stable physical properties, and therefore, one can expect high repeatability of the corner frequency for different gases. However, a back-gated FET with single-layer-graphene in its channel requires complicated and expensive technology. Therefore, we propose to study layers made of two-dimensional material and assuring more homogenous properties than the mixture of MOS grains of different sizes and various potential barriers between them.

In the present work, we explore gas sensing with layers made of graphene flakes and titanium dioxide (TiO$_2$) nano-particles. Both materials are photocatalytic and therefore can be easily modulated by UV light irradiation. The layers can be produced by low-cost technology, specifically by painting and subsequently backing the solution located between gold electrodes to form the gas-sensing layer [11]. Our experimental studies consider the effect of UV light irradiation on $1/f$ noise. Furthermore, we discuss how this technology can be advanced in order to accomplish enhanced gas sensing.

2. Materials and Methods for Sensor Preparation

Our sensors were prepared by an earlier presented technology [11]. The gas-sensing layer comprises a mixture of reduced graphene oxide (rGO) and TiO$_2$ nanoparticles. Graphene is sensitive to various gases of practical interest, and the generated $1/f$ noise depends on the ambient atmosphere [12, 13]. Graphene oxide and reduced graphene oxide have been used as templates for preparing graphene-metal particle nanocomposite in earlier work [14], but these composite materials (graphene sheets with attached metal particles) are new in the context of gas sensors and catalysts. In our exploratory studies, reported below, we investigated this type of mixture and demonstrated its high potential for gas-sensing applications.

An rGO honeycomb network deteriorates at high temperature, but this process can be impeded by introducing TiO$_2$ nanoparticles which are gas sensitive and exhibit a photocatalytic effect as well. TiO$_2$ is characterized by a large bandgap, about 3.2 eV, and therefore, adding graphene will decrease the resistance of the gas-sensing layer. It was necessary to establish an appropriate weight proportion between TiO$_2$ nanoparticles and graphene for assuring a reasonable conductivity for gas-sensing measurement (employing DC resistance and resistance fluctuations), high gas sensitivity, and time stability of the prepared material.

The gas-sensing layers were prepared by mixing the two ingredients, painting on the substrate (Figure 1), and subsequently baking at 50°C for 30 minutes to stabilize the structures by removing the solvents, viz., ethanol for diluting TiO$_2$ nanoparticles (Aeroxide TiO$_2$ P25) and n-butyl acetate for diluting graphene flakes (Graphene Supermarket UHC-NPD-100ML) [11]. Four-point gold contacts on silicon were used as electrodes; the distance between each gold strip was 300 μm. The gas-sensing layers were very porous and displayed a large active surface (Figure 2). The thickness of the layers was below 75 μm and, due to the deposition technology, varied even within a single substrate by as much as up to 25 μm with a concave cross-section. We prepared layers with different graphene/TiO$_2$ weight ratios in order to find the most promising composition for gas-sensing applications [15]. The gas-sensing layers exhibited some drift in the time domain, but this effect can be disregarded in our experimental studies limited to a few months. We are conscious that the considered technology is used to present the potential of gas sensing of the investigated layers, and any commercial applications require optimized technology.

(a)

(b)
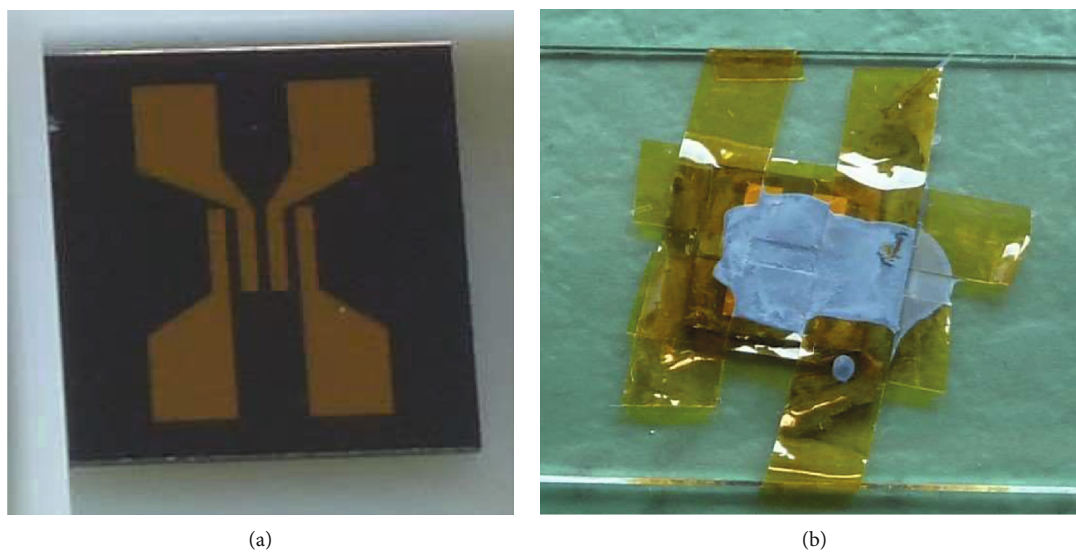
FIGURE 1: Preparation of the gas-sensing layer, showing (a) a silicon substrate with four gold electrodes and (b) the gas-sensing layer whose extent was confined by adhesive tape during painting.

(a)

(b)

(c)
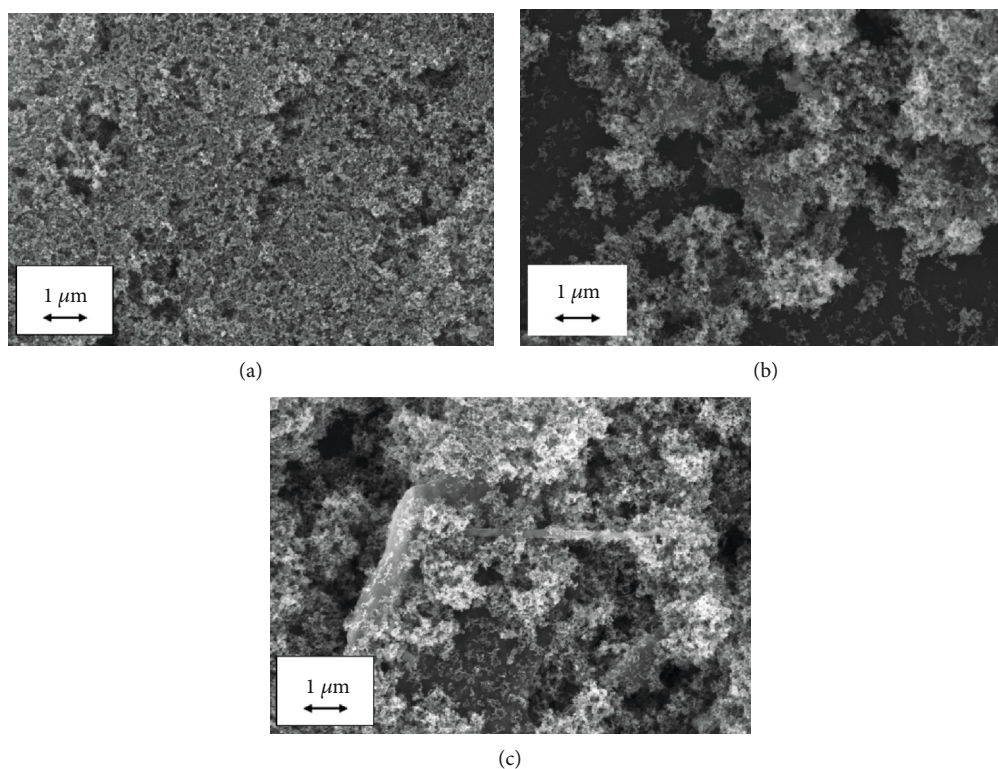
FIGURE 2: Scanning electron microscopy images of porous layers comprised of graphene flakes/TiO$_2$ nanoparticles with ratios being (a) 5, (b) 10, and (c) 20 wt%.

Noise measurements can be made on specimens whose DC resistance is no larger than hundreds of kΩ. The gas sensor is placed in a feed-back loop of a low-noise operational amplifier working as a current-voltage converter [16]. The RC filter embodying DC resistance and parasitic capacitance determines the frequency characteristic, and low-frequency noise cannot be measured appropriately when the DC resistance is too high. Thus, we selected for further studies three ratios of graphene flakes and TiO$_2$ nanoparticles, namely 5, 10, and 20 wt%. The resistance of these layers did not exceed about 20 kΩ at the chosen operating temperatures of 60 and 120°C. We also prepared sensors with 1 wt% of TiO$_2$ nanoparticles, but these samples had a DC resistance of up to tens of MΩ as well as low gas sensitivity and were therefore

excluded from detailed studies. The selected layers were investigated by scanning electron microscopy and showed porous structures comprised of graphene flakes decorated with TiO_2 nanoparticles (Figure 2).

3. Measurement Set-Up

Our gas-sensing layers were studied under exposure to selected ambient atmospheres by observing changes of DC resistance and resistance fluctuations at low frequencies. The sensors were placed in a metal gas chamber with a volume of one litre. The gas-sensing layers were sensitive to various gases, and in order to explore the potential of the FES method for gas detection, we used an ambient atmosphere of toxic NO_2 gas, which is of a large practical interest. Mass-flow meters (Analyt-MTC, GFC17 type) were used to establish the selected concentrations of NO_2 diluted in synthetic air. We mixed calibration gas (100 ppm of NO_2 in N_2 as carrying gas) with synthetic air (20% O_2, 80% N_2), and no humidity was present there. The gas mixture was introduced into the gas chamber at a flow rate below 200 ml/min in order to avoid gas turbulence, which might provide a spurious source of fluctuations not related to resistance fluctuations induced by adsorption-desorption events. The operating temperature was set by a DC voltage to a heater at the rear side of the silicon substrate and was monitored by a thermocouple.

The sensor was placed in a feed-back loop of a low-noise operational amplifier (Maxim Integrated MAX4478) working as a current-voltage converter. The output voltage was recorded by a precise data acquisition board (National Instruments, model PCI-4474 with 24-bit resolution of the A/D converter). The output voltage was determined by DC biasing the gas-sensing layer. This voltage had two components: a DC voltage depending on the resistance R of the gas-sensing layer and a random element proportional to resistance fluctuations. We confirmed that the recorded $1/f$ noise was dominated by noise generated within the gas-sensing structure, i.e., not by contact noise generated between the gold electrodes and the gas-sensing layer. This was verified by the square dependence between the DC voltage U across the sensor and the power spectral density of the voltage noise $S(f)$ [16]. Thus, there was no need to use a four-point contact method to reduce eventual contact noise. Our measurement set-up ensured that the normalized power spectral density, $S(f)/U^2$, was equal to the normalized power spectral density of resistance fluctuations, $S_R(f)/R^2$ [17].

The metal gas chamber was used for shielding against external electromagnetic interference. UV LEDs were placed at a distance of 1.5 cm from the gas-sensing layer. Two UV LEDs were applied, designated LED 1 (type T5F, Seoul Optodevice) and LED 2 (type OSV4YL5451B, OptoSupply). The bias currents I_D of the UV LEDs were set so as to assure the same maximum optical power emitted at different wavelengths λ (LED 1: $I_D = 8.3$ mA, $\lambda = 362$ nm; LED 2: $D = 10$ mA, $\lambda = 394$ nm). This arrangement enabled us to see how the wavelength of the UV light affected the generated low-frequency noise and the ability for gas detection.

4. Experimental Results and Discussion

Experimental data confirmed the usefulness of $1/f$ noise measurements on the low-cost gas-sensing layers. An $1/f$ noise component dominated up to a few kHz, which implies that the FES method can be utilized for these sensors by applying a low-noise measurement set-up. The voltage across the gas-sensing layer was recorded at a sampling frequency f_s of 20 kHz. We estimated the power spectral density of voltage fluctuations across the sensor by averaging over 512 spectra, and each spectrum was estimated by using 4096 voltage noise samples. The product of power spectral density and frequency was then normalized with the DC voltage, and $S(f) f/U^2$ was evaluated to expose any discrepancy from a $1/f$ dependence (Figure 3). This product presents a $1/f$ noise component as a flat line in the low-frequency range. Deviations from $1/f$ noise is represented as a local maximum. We did not give spectral data at frequencies close to the maximum frequency $f_s/2 = 10$ kHz when the antialiasing filter of the data acquisition board attenuated the signal.

Apart from the $1/f$ noise component, dominating within a frequency range up to a few kHz, we identified a Lorentzian at a corner frequency of 70 Hz under dark conditions and at an operating temperature T of 60°C (Figure 3(a)). The maximum of the Lorentzian is about twice larger than the $1/f$ noise recorded under UV light irradiation. The Lorentzian shifted to another frequency range upon irradiation of UV light. We observed that LED 1, with a short-wavelength emission, increased the white-noise component as compared with the effect induced by irradiation from LED 2. It appears that the higher energy at the shorter wavelengths generated shot noise. This effect is not so vivid at a higher operating temperature of 120°C (Figure 3(b)), and we can state that shot noise induced by UV light is not so intense when compared with the thermal noise of the sensing layer at $T = 120$°C. The experimental results suggest that the second temperature is too high to be used together with UV light irradiation.

We observed a similar change of the slope of $1/f$ noise when the sensor was in an ambient atmosphere of NO_2 gas (Figure 4). The presence of the gas shifted the Lorentzian (Figure 4(a)) at low concentration (5 ppm) in a similar way as UV light irradiation but did not increase the white-noise component as observed when the LED 1 was used (Figure 3(a)). Higher concentrations of NO_2 (10, 15 ppm) induced an increase of $1/f$ noise and white-noise components by up to a few times. The white-noise component is related to shot noise and thermal noise and, at high concentrations of NO_2, its increase is also related to a change of the DC resistance.

When we irradiated the gas-sensing layer by UV light in an ambient atmosphere with a low concentration of NO_2 (5 ppm), we observed amplification of $1/f$ noise at low frequencies (below 10 Hz) for the LED 2 only (Figure 4). The LED 2 emitted light at longer wavelengths (maximum at 394 nm) and supplied smaller energy as compared with the LED 1 (maximum at 362 nm). This fact explains why the LED 2 induced intense $1/f$ noise at frequencies below 10 Hz (Figure 4(c)) whereas the LED 1 did not (Figure 4(b)).
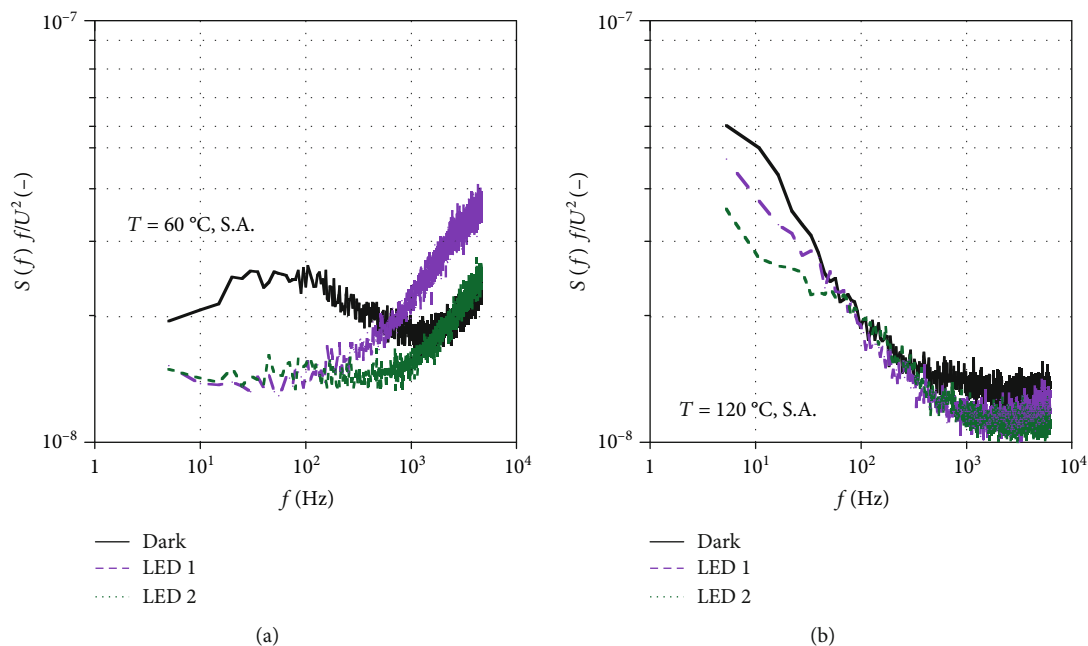
(b)

Figure 3: Normalized product $S(f)\,f/U^2$ of frequency f and power spectral density $S(f)$ of voltage fluctuations across a gas sensor biased by a DC voltage U when the sensor is in an ambient atmosphere of synthetic air (S.A.) and operating at (a) $T = 60°C$ and (b) $T = 120°C$. The sensing layer (graphene flakes/TiO$_2$ ratio 10 wt%) was working in the dark and under UV light supplied by LEDs with emission wavelengths of 362 nm (LED 1) and 394 nm (LED 2).

We should underline that the power spectral densities changed by up to a few times, and these differences are much larger than the observed changes of the DC resistance induced by UV light irradiation or by the ambient atmosphere of NO$_2$. Moreover, the Lorentzian is characterized by a corner frequency whose value is very informative for gas detection algorithms. This result can be explained by the activation mechanism of UV light irradiation on gas sensing. It is known that UV light generates ions O$_2^-$(g) covering the surface of gas-sensing grains [18]. These ions have much weaker binding to the grains than the chemisorbed ions O$_2^-$. Therefore, any changes in fluctuation phenomena induced by the introduced gas can be more intense due to lower binding energy. Moreover, corner frequencies $f_c = 1/2\pi\tau_c$ for G-R events can be higher due to lower energy and visible at higher frequencies, as observed in our experimental studies.

The DC resistance depended on operating temperature and graphene flakes/TiO$_2$ ratio. When UV light, irradiating the sensor or toxic NO$_2$ gas, was introduced, we observed a drop of the DC resistance. Relative change of DC resistance was about 60% of the initial value for the lowest investigated graphene flakes/TiO$_2$ ratio of 5 wt%. The sensor with a graphene flakes/TiO$_2$ ratio of 20 wt% had a DC resistance of about a few hundred Ω only, and the observed drop did not exceed 30% at the highest concentration of 15 ppm of NO$_2$. The layers with the graphene flakes/TiO$_2$ ratio of 10 wt% had a DC resistance of some tens of kΩ. Slightly higher DC resistance was exhibited for the gas-sensing layer with a graphene flakes/TiO$_2$ ratio of 5 wt%. The DC resistances of the gas-sensing layers varied because of different graphene fla-

kes/TiO$_2$ ratios and because of differences in the thicknesses of the tested specimens. All recorded DC resistances and time series of voltage across the sensor, and the detailed description of the files, were saved as data sets in MATLAB workspace format (the files *.mat) and are available for further use at https://drive.pg.edu.pl/s/G4R5w0CMzjJpRIA.

It should be noted that graphene is sensitive to irradiation at the wavelengths of the applied UV light, and it has been experimentally confirmed that UV light at a wavelength of 280 nm can damage and alter the characteristics of a single-layer-graphene sensing device [9]. Thus, the combination of operating temperature and UV light wavelengths determines the frequency position of the Lorentzian and its presence. We observed that at the operating temperature of 120°C, and in an ambient atmosphere of SA, the UV light intensified the 1/f noise at low frequencies (Figure 5(a)). At the same operating temperature and under dark conditions, but at an ambient atmosphere of 15 ppm of NO$_2$, there was a Lorentzian at a corner frequency of 100 Hz (Figure 5(b)). The corner frequency shifted when UV light was applied.

We conclude that the presented results are very promising with regard to practical applications of the FES method implemented with low-cost gas-sensing layers. We observed for a few sets of working conditions that the Lorentzians occurred at different corner frequencies. Their presence can be easily utilized to enhance gas detection even when the ambient atmosphere is a gas mixture. The results are similar to those observed for a back-gated field-effect transistor with single-layer-graphene in its channel [9], and the identified corner frequencies, characteristic for different investigated gases, were in a range similar to the frequencies observed in

(a)

(b)

(c)

FIGURE 4: Normalized product $S(f)f/U^2$ of frequency f and power spectral density $S(f)$ of voltage fluctuations across a gas sensor biased by a DC voltage U when the sensor, operating at $T = 60°C$, was in an ambient atmosphere of synthetic air (S.A.) and in the shown concentrations of NO_2. The sensing layer (graphene flakes/TiO_2 ratio 10 wt%) was working in the dark and under UV light supplied by LEDs with emission wavelengths of 362 nm (LED 1) and 394 nm (LED 2).

the present work. We suppose that the addition of TiO_2 nanoparticles, which decreases the bandgap, makes the graphene flakes more sensitive to gas detection. Unfortunately, the introduced nanoparticles change the $1/f$ noise and alter its intensity between the various samples of gas-sensing layers as a result of unavoidable imperfections induced on the graphene surface. The results suggest that the considered low-cost technology utilizing a two-dimensional material (graphene flakes) can give acceptable gas-sensing properties.

Our results are close to those for very selective, and certainly more sensitive, sensors utilizing single-layer-graphene, which offer highly repeatable sensing parameters but are very fragile and expensive.

There are still problems associated with our technology, which require further in-depth studies, and we do not know how repeatable and durable the technology is with the investigated gas-sensing layers. The layers were rather thick and as a consequence of the simple, and very cheap, technology,
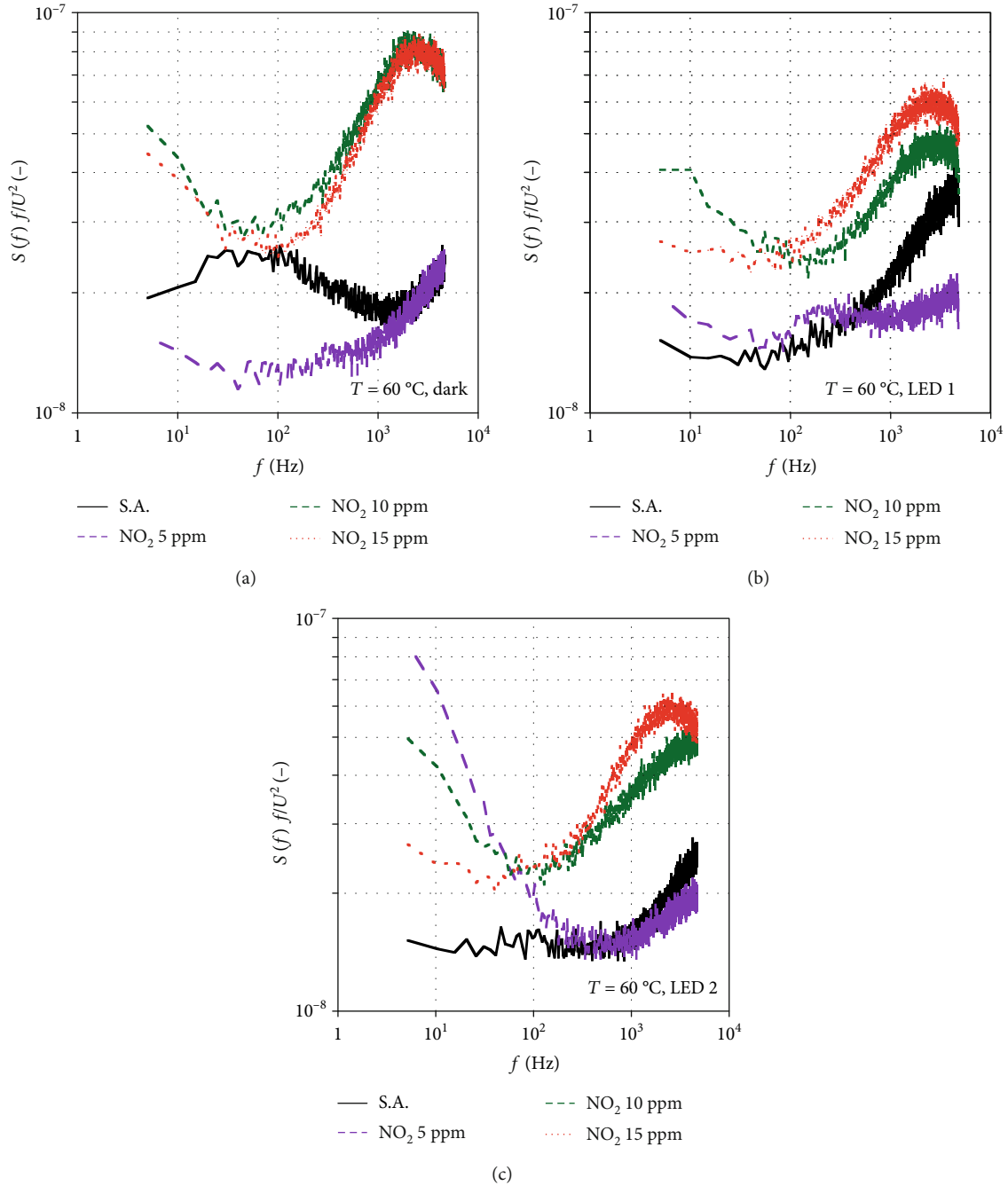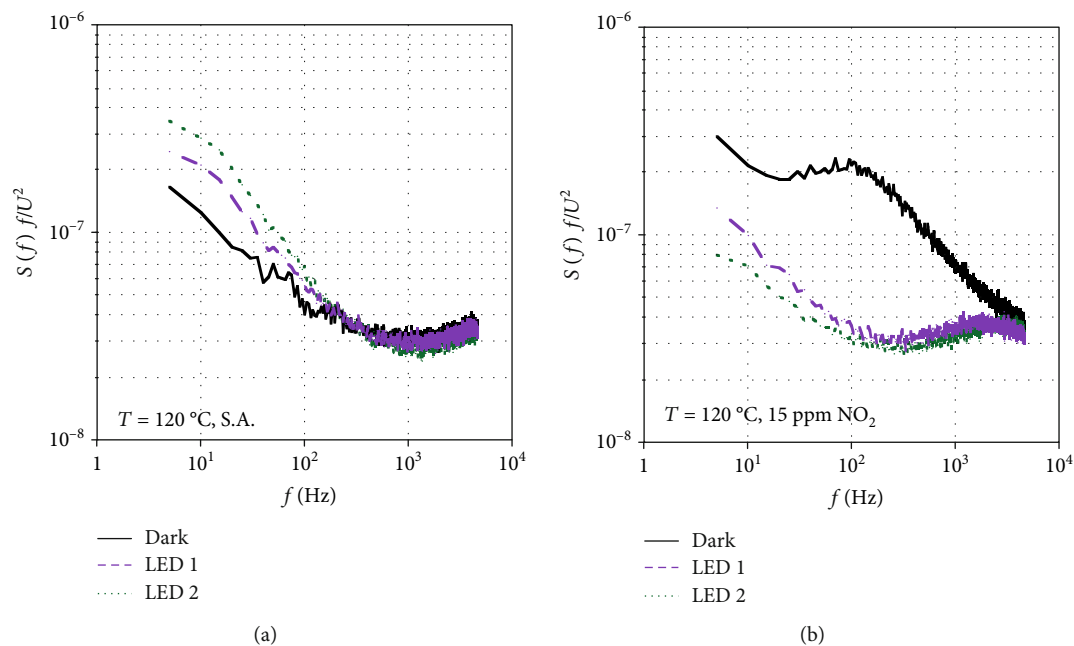
FIGURE 5: Normalized product $S(f) f/U^2$ of frequency f and power spectral density $S(f)$ of voltage fluctuations across a gas sensor biased by a DC voltage U when the sensor was in an ambient atmosphere of (a) synthetic air (S.A.) and (b) 15 ppm of NO_2 diluted in S.A. The operating temperature was $T = 120°C$. The sensing layer (graphene flakes/TiO_2 ratio 10 wt%) was working in the dark and under UV light supplied by LEDs with emission wavelengths of 362 nm (LED 1) and 394 nm (LED 2).

their thicknesses vary significantly. We are confident that much better results could be reached the by spin coating technology. Sensing parameters would then be more reproducible, and the sensing layers could be as thin as a few μm only. Then, we expect an even more significant impact of UV light irradiation on the sensing properties. In fact, the penetration depth of UV light in the graphene flake/TiO_2 layer does not exceed a few μm; its value depends on the morphology of the layer and is determined by the specific graphene flakes/TiO_2 ratio. This issue has to be studied experimentally in order to ascertain optimal technical parameters. Moreover, a very thin layer would decrease the response time and make gas detection more facile and measurement time much shorter than for the experiments reported above. A decrease of the response time would require advanced signal processing to account for differential values for gas detection in order to remove unavoidable drifts in practical measurements. It would also be possible to apply some drift removal algorithms [19] in order to reduce this detrimental effect, and the same solution could be used to reduce effects of sensor ageing. In future work, the selected detection algorithm should be applied to detect gases in the ambient atmosphere [20]. Some of these algorithms were designed specifically for the FES method and utilize changes of the estimated power spectral densities [21].

5. Conclusions

We presented experimental results of NO_2 sensing by low-cost gas-sensing layers made from graphene flakes/TiO_2 nanoparticles mixtures. The layers were modulated by UV light irradiation using two LEDs with different emitted wave-lengths. The FES method was applied to detect an ambient gas, and the recorded $1/f$ noise exhibited Lorentzians at different corner frequencies. The Lorentzians were modulated by UV light and can be used to detect the ambient gas. Preliminary work indicated that optimum properties were obtained when the graphene flakes/TiO_2 nanoparticles ratio was 5 wt%. The DC resistance of the sensing layer was about tens of kΩ and allowed accessible low-frequency noise measurements by applying low-cost technology embodying a low-noise operational amplifier and A/D converter.

In addition, we proposed to advance the technology by applying spin coating to reduce the thickness of the gas-sensing layer, which would enhance the modulation by UV light. Our preliminary results suggest that low-cost gas detection can be sensitive to selected gases in a manner similar to that with much more expensive sensors based on a single-layer-graphene FET transistor. This result is promising for the detection of the components of gas mixtures when the modulated sensor replaces an array of independent resistive sensors, which consume much more energy for heating and require significant maintenance costs. The proposed sensors can be potentially applied in wearable applications as a consequence of their low cost and their low operating temperature which requires little energy for heating. In principle, temperature-activated adsorption-desorption of gas molecules was replaced by UV light modulation to produce similar effects. However, more thorough studies are needed to determine the repeatability of the sensitivity and gas selectivity for the sensors discussed in the present work.

The same remark is valid for determining the gas sensors' response at various humidity levels and optimal selection of operating temperature for detected gases. The reported

results for relatively low temperatures (60°C, 120°C) are important for practical applications since the energy consumed by the sensors is small.

It is worth mentioning that various two-dimensional materials (composite of rGO and TiO_2 [22], a few layers of MoS_2 [23]), decorated with nanoparticles of Au, exhibit photocatalytic effect and enhance their gas sensing under UV light irradiation. The observed changes of DC resistances are more profound when UV light activates adsorption-desorption processes. We can expect even better results for the FES method when applied for these materials. It means that our presented results open a new perspective on enhanced gas sensing for emerging gas-sensing materials.

We should underline that there are new proposals of physical phenomena that can be utilized to enhance gas sensing, including triboelectric effect [24] or even triboelectric-photoelectric coupling effect [25]. These proposals improve gas sensing and suggest self-powered sensors for wearable applications. We hope that such sensors applied for monitoring human activities can also utilize the FES method and introduce new sensing operations.

Data Availability

The data used to support the findings of this study using MATLAB workspace format (∗.mat) have been deposited in the local repository (https://drive.pg.edu.pl/s/G4R5w0CMzjJpRIA) and are available for further use.

Conflicts of Interest

The authors declare that there is no conflict of interest regarding the publication of this paper.

Acknowledgments

References

[1] G. Korotcenkov, "Gas response control through structural and chemical modification of metal oxide films: state of the art and approaches," *Sensors and Actuators B: Chemical*, vol. 107, no. 1, pp. 209–232, 2005.

[2] P. Heszler, R. Ionescu, E. Llobet et al., "On the selectivity of nanostructured semiconductor gas sensors," *Physica Status Solidi (b)*, vol. 244, no. 11, pp. 4331–4335, 2007.

[3] S. Vallejos, P. Umek, T. Stoycheva et al., "Single-Step deposition of Au- and Pt-nanoparticle-functionalized tungsten oxide nanoneedles synthesized via aerosol-assisted CVD, and used for fabrication of selective gas microsensor arrays," *Advanced Functional Materials*, vol. 23, no. 10, pp. 1313–1322, 2013.

[4] A. Dziedzic, B. Licznerski, and A. Kolek, "Noise and nonlinearity of gas sensors: preliminary results," in *Proc. 22nd International Spring Seminar on Electronics Technology*, pp. 99–104, Dresden-Freital, Germany, May 1999.

[5] L. B. Kish, R. Vajtai, and C. G. Granqvist, "Extracting information from noise spectra of chemical sensors: single sensor electronic noses and tongues," *Sensors and Actuators B: Chemical*, vol. 71, no. 1–2, pp. 55–59, 2000.

[6] Ł. Lentka, J. M. Smulko, R. Ionescu, C. G. Granqvist, and L. B. Kish, "Determination of gas mixture components using fluctuation enhanced sensing and the LS-SVM regression algorithm," *Metrology and Measurement Systems*, vol. 22, no. 3, pp. 341–350, 2015.

[7] M. Trawka, J. Smulko, L. Hasse, C. G. Granqvist, F. E. Annanouch, and R. Ionescu, "Fluctuation enhanced gas sensing with WO_3-based nanoparticle gas sensors modulated by UV light at selected wavelengths," *Sensors and Actuators B: Chemical*, vol. 234, pp. 453–461, 2016.

[8] J. Smulko, "Advanced operating methods," in *Advanced Nanomaterials for Inexpensive Gas Microsensors*, E. Llobet, Ed., pp. 189–208, Elsevier, 2020.

[9] S. Rumyantsev, G. Liu, R. A. Potyrailo, A. A. Balandin, and M. S. Shur, "Selective sensing of individual gases using graphene devices," *IEEE Sensors Journal*, vol. 13, no. 8, pp. 2818–2822, 2013.

[10] S. Rumyantsev, G. Liu, M. S. Shur, R. A. Potyrailo, and A. A. Balandin, "Selective gas sensing with a single pristine graphene transistor," *Nano Letters*, vol. 12, no. 5, pp. 2294–2298, 2012.

[11] Z. Ye, H. Tai, C. Liu et al., "The investigation of reduced graphene oxide/titanium dioxide-based sensor for formaldehyde detection at room temperature," in *2015 IEEE SENSORS*, pp. 731–734, Busan, South Korea, November 2015.

[12] M. Donarelli and L. Ottaviano, "2D materials for gas sensing applications: a review on graphene oxide, MoS_2, WS_2 and phosphorene," *Sensors*, vol. 18, no. 11, p. 3638, 2018.

[13] A. A. Balandin, "Low-frequency 1/ _f_ noise in graphene devices," *Nature Nanotechnology*, vol. 8, no. 8, pp. 549–555, 2013.

[14] C. Xu, X. Wang, and J. Zhu, "Graphene–metal particle nanocomposites," *Journal of Physical Chemistry C*, vol. 112, no. 50, pp. 19841–19845, 2008.

[15] J. Smulko, M. Trawka, U. Cindemir, C. G. Granqvist, and C. Duran, "Resistive gas sensors: perspectives on selectivity and sensitivity improvement," in *Presented at the Conf. NANOfIM 2016*, Chemnitz, Germany, 8-9 September 2016URN: urn:nbn:se:uu:diva-302554.

[16] M. Kotarski and J. Smulko, "Noise measurement set-ups for fluctuations-enhanced gas sensing," *Metrology and Measurement Systems*, vol. 16, no. 3, pp. 457–464, 2009.

[17] B. Ayhan, C. Kwan, J. Zhou et al., "Fluctuation enhanced sensing (FES) with a nanostructured, semiconducting metal oxide film for gas detection and classification," *Sensors and Actuators B: Chemical*, vol. 188, pp. 651–660, 2013.

[18] S. Zhang, T. Lei, D. Li, G. Zhang, and C. Xie, "UV light activation of TiO_2 for sensing formaldehyde: how to be sensitive, recovering fast, and humidity less sensitive," *Sensors and Actuators B: Chemical*, vol. 202, pp. 964–970, 2014.

[19] Ł. Lentka and J. Smulko, "Methods of trend removal in electrochemical noise data - Overview," *Measurement*, vol. 131, pp. 569–581, 2019.

[20] R. Gutierrez-Osuna, "Pattern analysis for machine olfaction: a review," *IEEE Sensors Journal*, vol. 2, no. 3, pp. 189–202, 2002.

[21] H.-C. Chang, L. Kish, M. King, and C. Kwan, "Binary fingerprints at fluctuation-enhanced sensing," *Sensors*, vol. 10, no. 1, pp. 361–373, 2010.

[22] Y. Zhou, X. Li, Y. Wang, H. Tai, and Y. Guo, "UV illumination-enhanced molecular ammonia detection based on a ternary-reduced graphene oxide–titanium dioxide–Au composite film at room temperature," *Analytical Chemistry*, vol. 91, no. 5, pp. 3311–3318, 2018.

[23] Y. Zhou, C. Zou, X. Lin, and Y. Guo, "UV light activated NO2gas sensing based on Au nanoparticles decorated few-layer MoS2thin film at room temperature," *Applied Physics Letters*, vol. 113, no. 8, article 082103, 2018.

[24] S. Wang, Y. Jiang, H. Tai et al., "An integrated flexible self-powered wearable respiration sensor," *Nano Energy*, vol. 63, p. 103829, 2019.

[25] Y. Su, M. Yao, G. Xie et al., "Improving sensitivity of self-powered room temperature NO2sensor by triboelectric-photoelectric coupling effect," *Applied Physics Letters*, vol. 115, no. 7, article 073504, 2019.

Research Article

Accurate QTF Sensing Approach by Means of Narrow Band Spectral Estimation

Graziella Scandurra [ID]**, Gino Giusi, and Carmine Ciofi**

Department of Engineering, University of Messina, Messina 98166, Italy

Correspondence should be addressed to Graziella Scandurra; gscandurra@unime.it

We propose a new approach for the extraction of the equivalent parameters of quartz tuning forks used as sensors by means of noise measurements. Noise is used as the test signal for the determination, by means of spectral analysis, of the frequency response of a circuit including the quartz tuning fork whose parameters need to be determined. A new approach for the analysis of strongly peaked noise spectra was developed in order to allow the correct measurement of the strongly peaked noise spectrum at the output of the system, which is the result of the high-quality factor of any quartz tuning fork-based sensor. With the approach we propose, the best compromise in terms of accuracy and measurement time can be obtained in a single measurement run. The performances of the approach we propose are discussed in comparison with those that can be obtained from a swept spectrum approach in the same operating conditions.

1. Introduction

AT-cut crystals operating in the MHz range dominate the field of quartz crystal microbalance (QCM) applications, but quartz tuning fork- (QTF-) based sensors have also been demonstrated [1, 2]. Notwithstanding that the geometrical shape of QTFs makes their functionalization more challenging with respect to AT-cut crystals, the fact that they operate at much lower frequencies can be advantageous in terms of hardware requirements. While in some cases only a few relevant parameters, such as the resonance frequency f_S and the quality factor Q, are taken into consideration for sensing applications, full information on the QFT response may require the extraction of the values of all parameters in the equivalent circuit in Figure 1.

The extraction of all parameters in Figure 1 can be obtained starting from the measurement of the response of circuits such as the one in Figure 2 where assuming the transconductance gain A_R to be constant, the voltage gain V_O/V_I is proportional to the QTF admittance Y_Q:

$$H_V(f) = \frac{V_O}{V_I} = A_R Y_Q \qquad (1)$$

However, if we require high accuracy, with the circuit in Figure 2, we face two major challenges. In the first place, deviation of the amplifier response from ideality should be minimized or at least recognized and corrected; in the second place, the frequency response measurement must be carried out ensuring that no artifacts are introduced as a result of the strongly peaked response due to the high-quality factor Q of the QTF.

To address the first issue, we recently proposed an approach, based on a variant of the circuit in Figure 2, that allows to easily detect and correct nonidealities in the frequency response of the amplifier without requiring any adjustment on the circuit [3]. As for the second challenge, there are typically two approaches for the determination of the frequency response of a system such as the one we are concerned with: swept spectrum measurements and input-output cross correlation. In the case of swept spectrum measurements, V_I in Figure 2 is a sinusoidal signal whose instantaneous frequency is linearly changed with time. Under proper conditions (sufficiently small frequency change rate), the amplitude and phase response of the system can be extracted from the analysis of the sinusoidal signals at

$$f_S = \frac{1}{2\pi \sqrt{L_S C_S}}$$
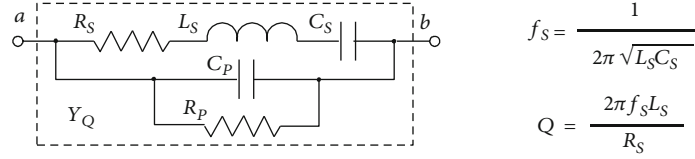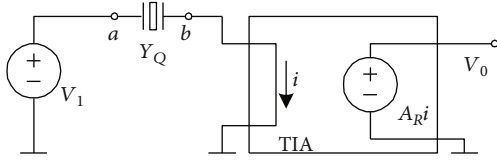
$$Q = \frac{2\pi f_S L_S}{R_S}$$

FIGURE 1: Equivalent circuit of a quartz tuning fork.

FIGURE 2: Simplified schematic of the circuit that can be used for obtaining a frequency response proportional to the QTF admittance; TIA is an ideal transimpedance amplifier with a constant gain A_R.

the input and at the output. In the case of cross correlation-based measurement, the input signal is a wide band noise and the frequency response is obtained by evaluating the cross spectrum between the input and the output signals. In the case of swept spectrum measurements, errors in the determination of the frequency response may arise from excessive frequency change rates while in the case of cross correlation measurements, window leakage may be responsible for systematic errors [4]. For a common wristwatch QTF exposed to air, the quality factor Q is in the order of 10^4, resulting in a peaked frequency response, when introduced in the circuit in Figure 2, centered at about 32.7 kHz with a half power bandwidth B of a few Hz. According to the criteria used in swept spectrum measurements [4], systematic errors arise unless the sweep rate is less than 1 Hz/s, leading to long measurement times for exploring a significant bandwidth across the resonance frequency. In the same way, when FFT-based cross correlation measurement approaches are used, the resolution bandwidth Δf should be much smaller than the bandwidth of the peaked response in order to avoid significant spectral leakage [4, 5]. Since the length of a time record for conventional spectral estimation using FFT is $1/\Delta f$, in order to improve accuracy, the measurement time must be increased. In order to better appreciate the type of systematic errors that are the result of an incorrect selection of measurement parameters, we report in Figures 3 and 4 the result of simulated measurements with the circuit in Figure 2 in the case of swept spectrum and cross correlation approaches, respectively. In order to simplify the discussion, we have assumed $R_P \rightarrow \infty$ and $C_P = 0$. We have also assumed that $A_R = R_S$, so that at the resonance frequency we have, from Equation (1), $H_V(f_S) = Y_Q(f_S)R_S = 1$.

The results in Figure 3 refer to the case of $Q = 104$ (virgin QTF exposed to air) with frequency change rates (FCR) for the frequency sweeps ranging from 80 Hz/s down to 1 Hz/s. As it can be clearly verified, the larger the FCR, the larger is the error in the maximum amplitude of the response and in the frequency at which it occurs. If, in actual measurements,

we assumed the frequency of the maximum of the response (f_{MAX}) as an estimate of the QTF resonance frequency f_S, we would obtain an estimation error $f_{ERR} = f_S - f_{MAX}$ which would depend on FCR (inset in Figure 3). When the QTF is functionalized, Q generally decreases, and the same FCR would result in a smaller error. Conversely, for the same tolerable error, faster sweep rates (larger FCRs) can be used for lower values of Q, thus potentially reducing the time required for the measurement. In actual measurements, however, the problem lies in the fact that, especially in sensing applications, it is not easy to know, beforehand, the measurement conditions that allow to obtain accurate results (within a given maximum error) in the shortest possible time. Of course, reducing the measurement time without affecting the accuracy is particularly important in sensing application as this reflects on the ability of the sensor system to follow rapid changes in the environment. In the case of swept spectrum measurements, comparing the results of repeated measurements obtained with different sweep rates (i.e., different values of FCRs) can provide a way to assess the presence of systematic errors. However, repeated measurements take time and therefore, if possible, they should be avoided.

Figure 4 refers to the case of the (simulated) determination of the frequency response in Figure 2 by means of the cross spectrum approach when using a conventional FFT spectrum analyzer. As mentioned before, the relevant parameter, in this case, is the resolution frequency Δf in comparison with the bandwidth $B = f_S/Q$. As it can be noticed in Figure 4, the estimated response is characterized by a significant error unless $\Delta f << B$. For a given sampling frequency f_C, the frequency resolution is determined by the number of samples N used for the estimation of the FFT on each single signal record ($\Delta f = f_C/N$), with $1/\Delta f$ being the duration of a record. Clearly, a smaller Δf corresponds to a longer record length, resulting therefore in an overall longer measurement time. As can be deduced from Figure 4, in the case $Q = 104$, with $f_C = 200$ kHz, we need N in excess of 2^{20} ($\approx 10^6$) in order to ensure minimum error, with a corresponding record duration in excess of 5 s. Moreover, in order to reduce the statistical error, the PSD estimation must be averaged over several records, leading to an overall measurement time in the order of minutes. Similar to the case of the swept spectrum approach, if the value of Q is reduced, Δf can be made larger and the measurement time is proportionally reduced. As before, however, in actual measurements, we do not know beforehand the actual value of Q and therefore it is not easy to set the correct value of Δf for optimizing accuracy and measurement time. In actual measurement sessions, we could proceed by starting with a relatively large Δf (short measurement
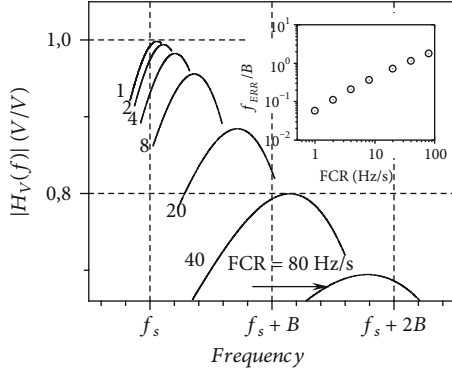
FIGURE 3: Simulated measurement of the frequency response $H_V(f)$ with the swept spectrum approach assuming an ideal TIA with $A_R = R_S$, $f_S = 32.7$ kHz, $Q = 104$, and $C_P = 0$; $R_P \to \infty$. FCR is the frequency change rate, ranging from 1 Hz/s up to 80 Hz/s. The error f_{ERR} in assuming the frequency of the maximum of the response as the resonance frequency is reported in the inset, normalized with respect to $B = f_S/Q$, as a function of the FCR.
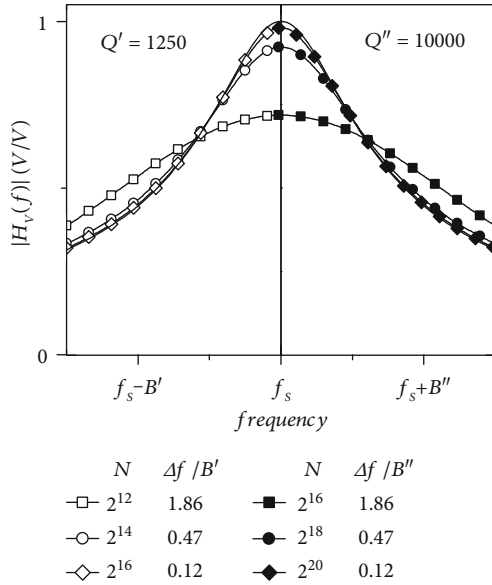

N	$\Delta f / B'$		N	$\Delta f / B''$
□ 2^{12}	1.86		■ 2^{16}	1.86
○ 2^{14}	0.47		● 2^{18}	0.47
◇ 2^{16}	0.12		◆ 2^{20}	0.12

FIGURE 4: Simulated results of the effect of the choice of the resolution bandwidth Δf on the measurement of the response $H_V(f)$ of the circuit in Figure 2 by means of the cross spectrum approach (with $C_P = 0$, $R_P \to \infty$). The ideal response is represented by the thick black curve.

time) and reducing it in successive measurement runs until no significant change is observed in the measured curve, a situation that would indicate that Δf has reached a sufficiently small value for not introducing systematic errors.

The important difference with respect to the case of the swept spectrum approach is that while in that case there is no way to perform measurements with different FCRs at the same time, it is possible, in principle, to set up a measurement configuration in which the cross spectrum approach is applied with a number of different values of Δf at the same time, i.e., in a single measurement run. Indeed, one could send the signals V_I and V_O in Figure 2 to a set of FFT spec-

trum analyzers (SAs), all working in parallel but with a different Δf setting from one another. In this way, on the SA with the largest Δf, we would obtain, in a very short time, an estimate of the response of the system; with a delay, due to the longer time record required, the SA with the next smaller Δf would provide its estimate: if it coincided with the first one, there would be no need to wait any further, otherwise, we wait for the estimate of the SA with the next smaller Δf and so on. Clearly, notwithstanding this potential advantage, resorting to several actual conventional SAs operating in parallel would be unpractical and expensive.

In the case of measurements on QTFs, however, all the information about the device response can be extracted from measurements in a quite limited bandwidth across the resonance frequency. With this observation in mind, we have been able to develop an approach for the correct estimation of the response of a system like the one in Figure 2 (where we expect a strongly peaked response in a limited bandwidth) that is functionally equivalent to the one we have described above (several SAs in parallel) but that can be implemented efficiently and with quite limited hardware resources. The theory underlying such an approach and the measurements demonstrating its effectiveness will be discussed in the following sections.

1.1. Proposed Approach. Conventional spectral estimation can be performed by resorting to the modified periodogram method described by Welch in 1967 [6]. The analog signal whose PSD needs to be estimated is low-pass filtered in order to allow correct sampling at frequency f_C (sampling period $\Delta t = 1/f_C$). The sequence of samples $x_i = x(i\Delta t)$ obtained from the filtered input $x(t)$ is divided into records of length N, and each record is multiplied by a proper window function $w_j (j = 0, \cdots, N - 1)$ obtaining a new set of records $y_{h,l}$:

$$y_{h,l} = x_{hN+l} w_l, \quad l = 0, 1, \cdots, N - 1, \tag{2}$$

where we have assumed that the first element of each record is x_{hN} ($h = 0, 1, \ldots$) so that the records are adjacent and non-overlapping. The Discrete Fourier Transform (DFT) of each record is calculated obtaining

$$z_{h,k} = \sum_{l=0}^{N-1} y_{h,l} e^{-j2\pi \frac{kl}{N}}; \quad k = 0, 1, \cdots, N - 1 \tag{3}$$

with $|z_{h,k}|^2$ representing an estimate, for $k < N/2$, of the power of the input signal after being filtered by a bandpass filter centred at $f_k = k f_{CK}/N$ whose equivalent noise bandwidth (ENB) and detailed frequency response depend on f_C, N, and on the window function w. If the window function satisfies the normalization condition

$$\sum_{l=0}^{N-1} |w_l|^2 = 1, \tag{4}$$

and if we assume that the PSD of the input signal can be considered approximately constant within the bandwidth of the

filter (white noise approximation), the quantity $|z_{h,k}|^2/\text{ENB}$ can be regarded as an estimate of the PSD of the input signal at f_k as obtained from the elaboration of the hth record. The estimate from a single record, however, is quite a crude one, as the standard deviation of the error in the estimate can be as large as the PSD to be estimated. It is for this reason that the results from M records need to be averaged as this reduces the statistical error by a factor $\sqrt{M}$ (assuming that the estimates obtained from nonoverlapping records are uncorrelated). It must be noted that while the ENB changes depending on the shape of the window, for the most common window types it ranges from f_C/N up to $1.5 f_C/N$ [7] so that, in a first approximation, it essentially coincides with the frequency resolution $\Delta f = f_C/N$. The success of the approach outlined above mostly depends on the fact that if N is chosen as a power of 2, the DFT in Equation (3) can be calculated by resorting to the very efficient fast Fourier transform (FFT) algorithm [8]. As we have noted before, in the case of the measurements on QTF, we should be working with $\Delta f << f_s/Q$ that may correspond to record lengths in the order of 10^6 for the largest expected values of Q. On the other hand, if we are interested in the extraction of the QTF parameters from the measurement of its admittance, we do not need to explore the entire frequency range from 0 to $f_C/2$, but we can limit our focus to a few bandwidths B ($B = f_S/Q$) across the resonance frequency. The chirp Z-transform (CZT) algorithm initially developed by Rabiner et al. [9] can be set up for evaluating the DFT of the input sequence of N samples at N equally spaced frequency values with an arbitrary frequency start and arbitrary frequency step at the cost of 3 FFT computations on sequences of length $2N$ (only 2 FFT calculations are required in the case of repeated estimations). Note, however, that the ENB still depends on N and therefore, the chirp-z transform cannot, in itself, provide any advantage for the problem at hand. To work around this issue, we have devised an approach for obtaining an arbitrarily small ENB by a proper elaboration of the DFTs calculated on adjacent input records regardless of the record length N. When this approach is employed together with the CZT, we can efficiently elaborate records of N samples at a time obtaining the desired frequency resolution close to f_S and combine the results of the elaboration on the DFTs on adjacent records in order to obtain any (and more than one at the same time) ENB we may require. In order to better understand the approach we propose, it can be useful to refer to Figure 5.

The block diagram in Figure 5 can be regarded as the idealized continuous time counterpart of the process that in the modified periodogram method leads to the estimation of the power of the process when filtered by a bandpass filter centered at f_k. The output of the filter is sampled at intervals $N\Delta t$, and the squared moduli of the samples are averaged for obtaining an estimation of the PSD of the process at f_k. In the conventional modified periodogram approach, the filter is a finite response filter (window) with an impulse response lasting exactly $N\Delta t$. This property ensures, in the numerical domain, that only the last N signal samples are required for each new estimation of the quantities $z_{h,k}$. At the same time, as noted before, the length of the impulse response sets a limit to the selectivity of the filter. Suppose now that we maintain
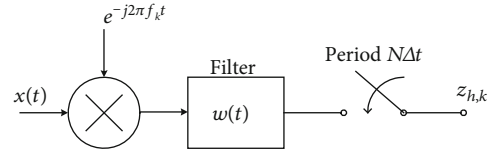
FIGURE 5: Continuous time equivalent of the approach used for the estimation of the PSD in DFT spectrum analyzers.
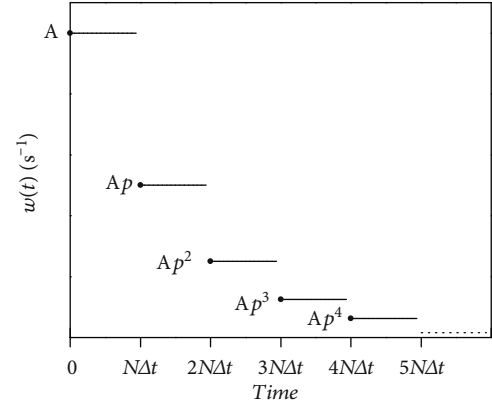
FIGURE 6: Impulse response of the continuous time domain filter from which the actual window function used in the proposed approach is derived. The parameter p ranges from 0 to 1.

the configuration in Figure 5, still sampling the output of the filter at intervals $N\Delta t$, but no longer enforcing a limit for the impulse response duration of the filter and, hence, for the selectivity that can be obtained. While in principle we can use any impulse response, for the computation algorithm to remain efficient, we must maintain the condition, if possible, that each new power estimate (sampled value at the output of the filter) can be obtained by maintaining in memory only a finite (an possibly small) number of sampled input values. A filter with the impulse response $w(t)$ sketched in Figure 6 does indeed satisfy this constraint since, as we shall presently demonstrate, the power estimate at the end of each interval of duration $N\Delta t$ can be obtained as a function of the power estimate in the preceding interval and of the last N sampled input values. In the discrete time domain, we replace the impulse response $w(t)$ with its sampled counterpart $w_i = \alpha w (i\Delta t)$. Note that the parameter α has the physical dimension of a time, and it is required in order to obtain a dimensionless w_i. Note that the values of α and of the parameter A defining the amplitude of $w(t)$ in Figure 6 must be chosen so that their product allows to satisfy the normalization condition with ($N \to \infty$) in Equation (4). In order to simplify the discussion, assume that $x_i = 0$ for $i < 0$. In the discrete time domain, the output $z_{h,k}$ of the filter in Figure 6 at $i = (h + 1)N\Delta t$ is

$$z_{h+1,k} = \sum_{l=0}^{(h+1)N-1} x_l w_{(h+1)N-1-l} e^{-j2\pi\frac{k}{N}l} == \sum_{l=0}^{hN-1} x_l w_{(h+1)N-1-l} e^{-j2\pi\frac{k}{N}l}$$
$$+ + \sum_{l=hN}^{(h+1)N-1} x_l w_{(h+1)N-1-l} e^{-j2\pi\frac{k}{N}l}.$$

$$(5)$$

With the index change $m = l - hN$ in the last sum and exploiting the following property for w_i,

$$w_{i+N} = p w_i, \quad (6)$$

we have

$$z_{h+1,k} = p \sum_{l=0}^{hN-1} x_l w_{(h+1)N-1-l} e^{-j2\pi \frac{k}{N} l}$$
$$+ + e^{-j2\pi kh} \sum_{m=0}^{N-1} x_{hN+m} w_{N-1-m} e^{-j2\pi \frac{k}{N} m} == p z_{h,k} \quad (7)$$
$$+ \alpha A e^{-j2\pi kh} \sum_{m=0}^{N-1} x_{hN+m} e^{-j2\pi \frac{k}{N} m}.$$

Note that the last sum over m, except for a normalization factor, is nothing but the DFT of the sequence of the last N samples when a uniform window is used. Equation (7), therefore, offers a quite efficient approach for evaluating $z_{h,k}$ recursively, starting from the evaluation of the DFT over the last N samples. What makes the function w_i especially useful is the fact that the values of p ($0 \le p < 1$) is set the bandwidth of the filter and hence the ENB for spectral estimation.

Using quite standard mathematical techniques, it can be easily demonstrated that, in the continuous time domain, the frequency response $W(f)$ corresponding to the impulse response $w(t)$ is

$$W(f) = AT \frac{\sin(\pi f T)}{\pi f T} \frac{e^{-j\pi f T}}{1 - p e^{-j2\pi f T}} ; T = N\Delta t = \frac{N}{f_C}, \quad (8)$$

with an *ENB*:

$$ENB = \frac{1-p}{1+p} \frac{f_C}{N}. \quad (9)$$

From Equation (7), we notice that the same DFT computed over the last N samples can be used for updating the values of as many $z_{h,k}$ as desired (each one corresponding to a different p and, hence, to a different ENB) with a very small computational overhead. In short, thanks to the combination of the chirp z-transform and the approach we have just described, we are now in the condition to implement the multiple spectrum analyser approach discussed at the end of the previous section with acceptable cost in terms of memory allocation and computational complexity. We can proceed as follows:

(1) We start by setting the number of frequency points that are required (N)

(2) We set up the parameters of the chirp z-transform algorithm in such a way as to obtain the spectra estimation at N closely spaced frequencies across the (expected) series resonance frequency

(3) We set up a number of values for p leading to geometrically decreasing values of ENB (typically with a common ratio of 2)

(4) Each time a new input record (length N) is acquired, we perform a chirp-z transform on such a record in order to obtain the rightmost sum in Equation (7). Note that this transform needs to be calculated only once, regardless of the number of selected values for p

(5) For each value of p, we update the corresponding vectors of values $z_{h,k}$ (one vector of N complex values for each value of p)

(6) The values of $z_{h,k}$ corresponding to each p are used for spectral and cross spectral estimation

About the 6th step, it must be remarked the fact that while the $z_{h,k}$ corresponding to different p are all updated at time intervals equal to the duration of the input record, subsequent values of $z_{h,k}$ for a given p are strongly correlated over time distances shorter that the inverse of the corresponding ENB and therefore, in power spectra estimation or in cross spectra estimation, we obtain a reduction of the statistical uncertainty (according to the inverse of the number of averages law) only if the corresponding $z_{h,k}$ are sampled at time intervals at least equal to the inverse of the ENB.

In order to have an estimate of the resources required to perform the elaboration we propose, let us assume $N = 8192$. With $f_{CK} = 100\,\text{kHz}$, the ENB corresponding to $p = 0$ is about 12 Hz. Assuming $Q_{MAX} = 10000$, we should be able to obtain a minimum ENB significantly smaller than $f_s/Q_{MAX} \approx 3\,\text{Hz}$. Let us assume that we require to reach a minimum ENB of 0.1 Hz. It follows that 7 different values of p (including $p = 0$) are sufficient to cover the entire range of ENB values form 12 Hz down to less than 0.1 Hz in geometric progression with a common ratio of 2. Since we operate with two channels and we want to estimate the power spectra of each channel and the cross spectra for all values of p, it follows that, assuming 8 bytes for the storage of a double precision value (one complex value is equivalent, in terms of memory occupation, to two double precision values), the total memory occupation is less than 10 Mbytes, that is almost negligible for modern standards. As far as the computational cost is concerned, the most time-consuming operation is by far the calculation of the two chirp z-transforms on both channels, with all the other computations (including the $z_{h,k}$ update for all ps and spectral averaging) having a negligible impact. The computational cost, therefore, reduces to that of the calculation of 4 FFT (2 for each channel) of length $2N$ for each record of length N. Such computational cost is completely manageable even by low-end CPUs by today's standards.

In order to favour the experimentation of the proposed approach, we extended the public domain QLSA library [10] that now includes all the required data structures and computation algorithms for the implementation of narrow band spectral estimation approach discussed above. While developed with specific reference to the application in this
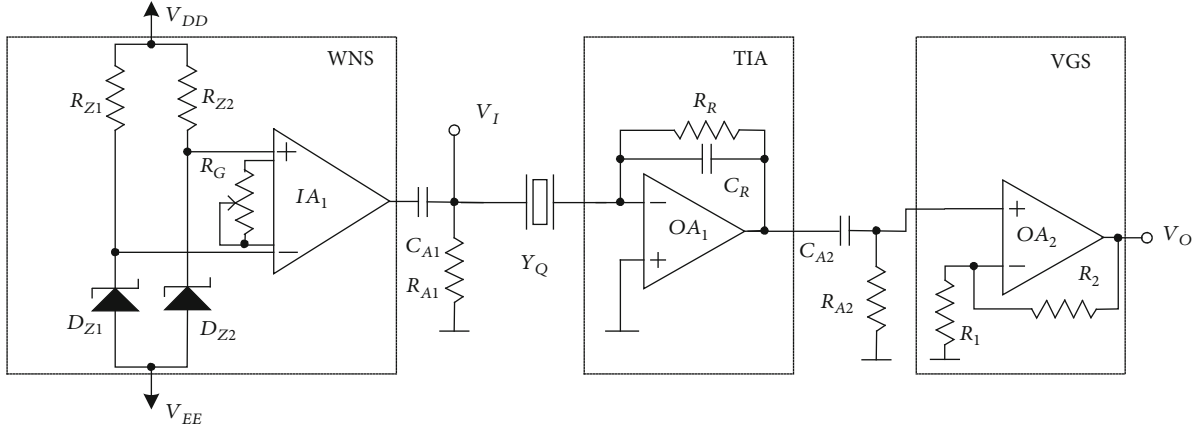
FIGURE 7: Detailed schematic of the circuit used for testing the approach we propose. The main blocks are a white noise source (WNS), a transimpedance amplifier (TIA) with capacitive feedback, and a voltage gain stage (VGS).

paper, the implementation in QLSA allows to extend the approach we propose to the estimation of narrow band spectra and cross spectra involving any number of channels [11]. A link to the web page where the library QLSA is described, with indications on how it can be obtained, is reported in Data Availability.

1.2. Experimental Results. In order to test the proposed approach, we resorted to the circuit configuration in Figure 7. The complete list of the components is reported in Table 1. The first block in Figure 7 is a white noise source (WNS) obtained starting from two nominally identical 10V Zener diodes (D_{Z1}, D_{Z2}) biased in breakdown with nominally identical currents ($V_{DD} = -V_{EE} = 12$ V; $R_{Z1} = R_{Z2} = 200$ kΩ). I_{A1} is an instrumentation amplifier (INA128) that rejects the (nominally) identical DC voltages at the cathodes of D_{Z1} and D_{Z2} and amplifies the uncorrelated noise signals across R_{Z1} and R_{Z2}. Note that notwithstanding that the Zener diodes and the resistances R_Z are mounted in direct thermal contact with each other, a DC voltage difference in the order of few mV is present at the input of I_{A1}, so that a high-pass filter (C_{A1}, R_{A1}) is used in order to reject the DC before the connection to the QTF and to the first input (V_I) of the data acquisition system. The transimpedance amplifier (TIA) stage in Figure 5 is the same as the one used in [3]. The resistance R_R, required to provide DC coupling to the inverting input of O_{A1}, is such that at frequencies close to the resonance of the QTF, it can be completely neglected with respect to the effect of the feedback capacitor C_R. By including the voltage gain stage (VGS), the overall transimpedance gain, from the inverting input of O_{A1} to the output V_O, close to the QTF resonance frequency, is

$$A_R = -\frac{A_V}{j2\pi f C_R}, A_V = 11. \tag{10}$$

As discussed in [3], this solution has the advantage of allowing a quite straightforward recognition and correction of the deviation of the gain of the system from the approximated expression in Equation (10) obtained in the assump-

TABLE 1: Component list for the circuit in Figure 5.

Component	Type	Value
I_{A1}	Instrumentation amplifier	IF3601
O_{A1}, O_{A2}	Operational amplifiers	OP27
Y_Q	QTF under test	—
R_{Z1}, R_{Z2}	0.1% metallic film resistor	200 kΩ
R_G	Multi turn trimmer	20 kΩ
R_{A1}	1% resistor	10 kΩ
C_{A1}	Polyester, 66 V	4.7 μF
R_{A2}	1% resistor	10 kΩ
C_{A2}	Polyester, 66 V	1 μF
R_R	1% resistor	10 MΩ
C_R	1%	100 pF
R_1	0.1% metallic film resistor	1 kΩ
R_2	0.1% metallic film resistor	10 kΩ

tion of virtual ground at the input of O_{A1}. In particular, in the assumption of the ideal response in Equation (10) for the amplifying chain, the overall frequency response H_V from V_I to V_O would be

$$H_V(f) = \frac{V_O}{V_I} = Y_Q A_R = H_R + jH_I, \tag{11}$$

where [3]

$$H_R(f) = -A_V \left\{ c_{PR} + c_{SR} \times \frac{Q^2 \left[1 - (f/f_S)^2 \right]}{Q^2 \left[1 - (f/f_S)^2 \right]^2 + (f/f_S)^2} \right\},$$

$$H_{IF}(f) = fH_I(f) = A_V Q f_S c_{SR} \left\{ r_{SP} + c_{SR} \times \frac{(f/f_S)^2}{Q^2 \left[1 - (f/f_S)^2 \right]^2 + (f/f_S)^2} \right\},$$
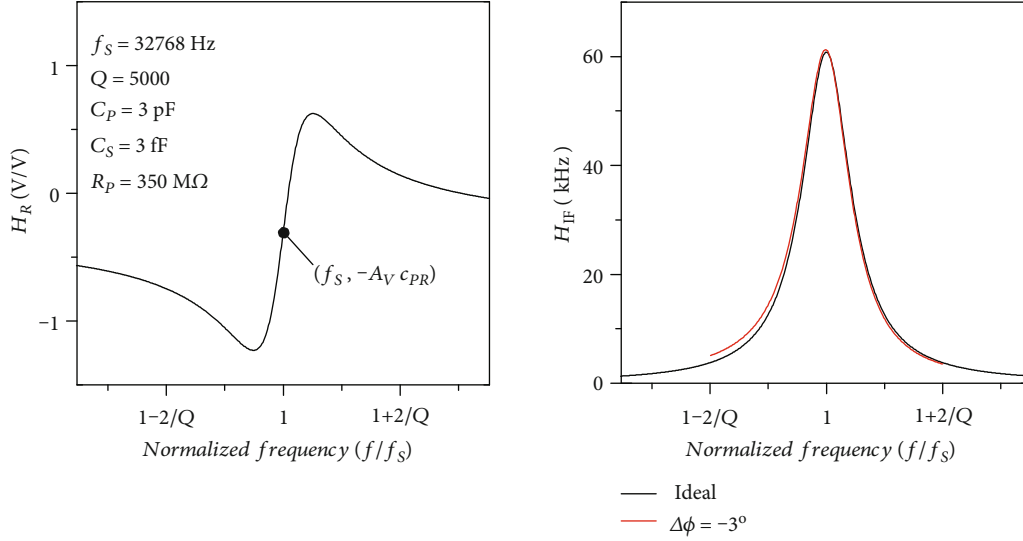
$$\tag{12}$$

FIGURE 8: Simulated behaviour of H_R and H_{IF} for a QTF operating at 32.8 kHz. The red curve is obtained in the presence of a phase error of -3 degrees in the frequency response.

with

$$c_{PR} = \frac{C_P}{C_R} \; ;$$

$$c_{SR} = \frac{C_S}{C_R} \; ; \qquad (13)$$

$$r_{SP} = \frac{R_S}{R_P} .$$

Note that H_{IF}, as defined in Equation (12), has the physical dimensions of a frequency. Thanks to the peculiar circuit configuration used in Figure 7, H_R and H_{IF} have the following symmetry properties:

$$H_{IF}\left(\frac{f}{f_S}\right) = H_{IF}\left(\frac{f_S}{f_S}\right), \qquad (14)$$

$$H_R(f/f_S) + A_V c_{PR} = -H_R\left(\frac{f_S}{f}\right) - A_V c_{PR}. \qquad (15)$$

From a graphical point of view, on a log scale for the frequency, Equation (14) corresponds to an even symmetry of H_{IF} with respect to f_S, while Equation (15) corresponds to an odd symmetry with respect to the point $(f_S, -A_V c_{PR})$ as shown in Figure 8 (solid lines). As mentioned before, Equation (10) is an approximation of the actual response obtained in the assumption of virtual ground. When high accuracy is required, however, the full response of the amplifying chain must be taken into account, which requires accounting for the effects of poles at higher frequencies [12]. As an example, suppose that a pole is present in the actual response at a frequency of, say, 20 times the resonance frequency of the QTF. This pole would introduce, at frequencies close to f_S, a gain error of less than 0.2% in the response amplitude and a phase error in the order of -3°. While the amplitude error can be usually neglected, the phase error may have a significant

impact in the extraction of the QTF parameters [13]. The presence of a phase error is especially apparent with reference to H_{IF}, as shown in Figure 8 (red curve) and can be corrected by introducing (numerically) the phase shift required for restoring symmetry in the measured response H_{IF} [4]. The way in which the QTF parameters can be obtained from the measured H_R and H_{IF}, once symmetry is restored, is discussed in [3]. Here, we are interested in demonstrating how the new method we propose for spectra estimation can help in reaching, in a short time and in a reliable way, an estimate of the response $H_V(f)$ by means of noise measurements. In order to do so, we will mostly focus on the properties of H_{IF} and on the values of the resonance frequency f_S and of the quality factor Q, which are the most important parameters that are taken into consideration in sensing applications.

When employing cross correlation, the frequency response H_V is obtained as

$$H_V(f) = \frac{S_{IO}(f)}{S_{II}(f)}, \qquad (16)$$

where S_{II} is the PSD of the noise at the input V_I and S_{IO} is the cross spectrum between the noise at the input V_I and the noise at the output V_O in Figure 7. In our experiments, signal acquisition was performed using a National Instruments PCI-4462 four-channel dynamic signal acquisition board while a dedicated software was developed for PSD estimation according to the approach we propose. As we mentioned above, the software we have developed is based on an upgraded version of the public domain library QLSA [10]. Acquisition frequency was set to 204.8 kHz, and the record length was 8192 (2^{13}). We employed a wristwatch QTF exposed to air as a DUT to work with the highest possible Q (functionalization for sensing applications is expected to reduce the quality factor). A set of 10 different values of p was used in order to obtain geometrically decreasing (with a factor of 2) ENB from 12.5 Hz down to about 24 mHz in
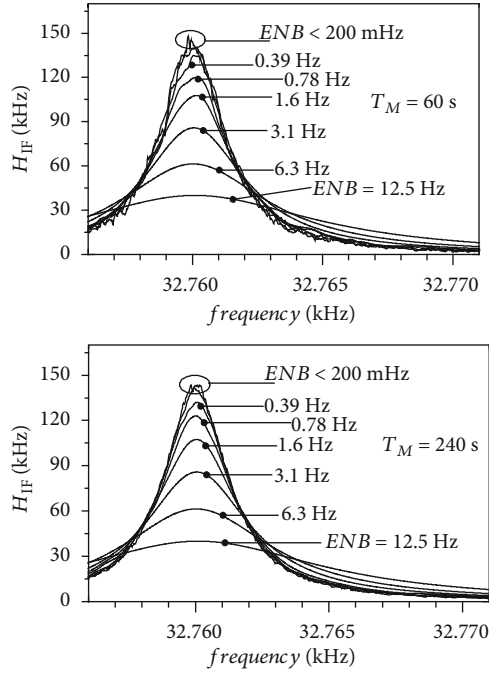
FIGURE 9: Result of the estimation of H_{IF} at $T_M = 60\,s$ and at $T_M = 240\,s$ since the measurement was started. All curves are obtained simultaneously in real time.

FIGURE 10: Values of the quality factor Q extracted from the curves in Figure 9 as a function of the ENB. The values of Q (together with all other parameters) are obtained by fitting each curve in Figure 9 against the function H_{IF} in Equation (12) in a frequency interval of 100 Hz centered across 32760 Hz.

FIGURE 11: Values of resonance frequency f_S extracted from the estimate of H_{IF} with ENB = 195 mHz vs measurement time. The values of f_S (together with all other parameters) are obtained by fitting the estimated H_{IF} against the function H_{IF} in Equation (12) in a frequency interval of 100 Hz centered across 32760 Hz.

a frequency range of 100 Hz across the resonance frequency (expected to be about 32760 Hz). A phase correction is performed in order to compensate for the distortion introduced by the nonideal behaviour of the amplifier. The correction, as discussed before, is performed numerically, and the correction angle is chosen as the one that ensures the best symmetry (Equations (14) and (15)). Figure 9 represents the situation for H_{IF} after 60 s (top graph) and 240 s (bottom graph) since the measurement was started. As we have discussed before, curves corresponding to different values of ENB are all obtained at the same time.

The fact that the curves corresponding to ENB down to about 400 mHz do not superimpose to one another is a clear indication that these curves cannot represent the actual H_{IF}. On the other hand, curves obtained with ENB below 200 mHz appear to be superimposed to one another, a clear indication that the corresponding ENB is sufficiently small not to induce systematic error in the estimate of H_{IF}. As it was expected, the curves corresponding to larger ENBs appear smoother because a large number of uncorrelated averages were accumulated in the available time. As we move toward smaller and smaller ENBs, fewer uncorrelated averages were possible resulting in larger residual statistical errors. Note that, for the same ENB, as the measurement time increases, more uncorrelated averages are accumulated and the statistical fluctuations in the estimates are reduced, as it is apparent by comparing the situation after 60 s and after 240 s in Figure 9. When looking at a representation like the one in Figure 9 in real time (during experiments), the measurement can be stopped as soon as one detects the situation in which a curve from a given ENB superimposes to the one corresponding to the next smaller ENB. To evidence the effect of an incorrect (i.e., too large) ENB on the extraction
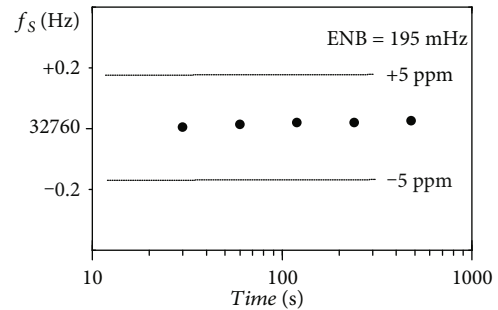
of the QTF parameters, we fitted all the curves in Figure 9 against the expression of H_{IF} in Equation (12). Because of the symmetry of H_{IF} (once the phase error is compensated), distortion due to large ENBs has a small or no effect on the frequency at which H_{IF} reaches its maximum (the resonance frequency). However, as it is apparent from Figure 10, a consistent (and therefore correct) estimate of the quality factor can only be obtained with ENBs below 200 mHz. As observed before, the threshold of 200 mHz for obtaining, in our test experiment, the correct estimate of Q is clearly detectable by observing the plots in Figure 9 in real time during measurements: all plots obtained with ENBs below 0.39 Hz essentially superimpose.

It is worth noticing that while curves obtained with low ENBs require longer measurement time for assuming a stable and highly regular shape, the error due to the low number of averages is statistical in nature. Therefore, if curve fitting over a frequency range is used for the estimation of the parameters we are interested in, such statistical errors tend to cancel out, even if they are still quite evident as in the plots in Figure 9. This is clearly demonstrated by the results reported in Figure 11, where the estimated value of f_S, obtained from fitting the measured H_{IF} for ENB = 195 mHz against the expression in Equation (12), is reported vs the measurement

FIGURE 12: Values of the resonance frequency f_S extracted from the curves in Figure 9 as a function of the ENB. The values of f_S (together with all other parameters) are obtained by fitting each curve in Figure 9 against the function H_{IF} in Equation (12) in a frequency interval of 100 Hz centered across 32760 Hz.
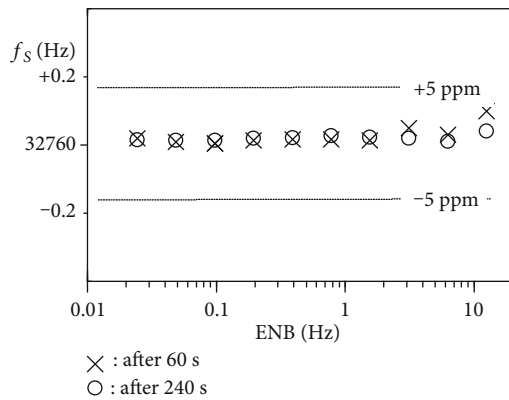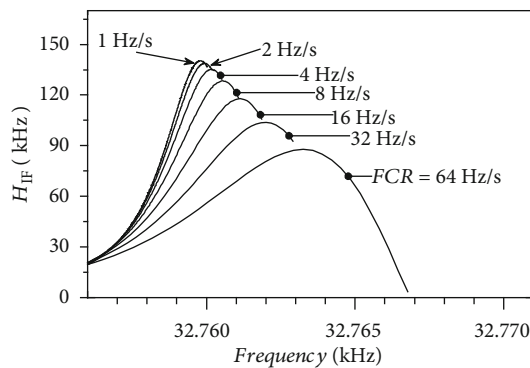

FIGURE 13: Estimation of H_{IF} obtained with the swept spectrum approach with different sweep speeds (FCR). For these measurements, the WNS block in Figure 7 was replaced with a swept sinusoidal source.

time. As it can be observed, the estimate changes by less than 1 ppm from 30 s up to 480 s.

We have already observed that the distortion due to spectral leakage preserves the symmetry of the estimated H_{IF}. Indeed, when we plot the results of the extraction of f_S for curves with different ENBs, as in Figure 12, we obtain that the estimated values of fs are almost the same (within a few ppm) regardless of the systematic error introduced by large values of ENBs. This is a clear advantage over the swept spectrum approach. If we indeed plot the results of the estimation of H_{IF} as can be obtained with the swept spectrum approach on the very same QTF used for obtaining the results in Figure 9, we obtain the plots in Figure 13, where it is clear that even with a FCR of 1 Hz/s we still cannot conclude, with an uncertainty comparable to what is obtained in Figure 12, that the correct value of fs is obtained at the frequency for which the curve has a maximum.

When dealing with functionalized QTF in sensing applications, a significant reduction of Q is generally expected. A lower Q, as observed before, translates into a large bandwidth B. Since, as a consequence of a larger B, the ENB below which

the curves in Figure 9 will superimpose increase, this means that the required measurement time for accurate results will decrease as well, so that a complete characterization of the QTF parameters can be typically obtained in a matter of a few seconds or, at most, a few tens of seconds.

2. Discussion and Conclusions

We have developed an effective approach for the accurate determination of QTF parameters based on noise measurements. In order to reach this goal, we had to address and solve the problem of the accurate estimation of the spectra of noise signals whose PSD changes significantly over a narrow bandwidth. The approach we have developed relies on a proper elaboration of the sampled noise signals that allows spectral and cross spectral estimation to be performed using several values of ENB at the same time. This allows the user to easily select the maximum ENB that do not cause systematic errors and that can therefore lead to the correct estimate of the QTF parameters in the shortest time possible. Since the results corresponding to each ENBs are all available at the same time, the need for repeated measurements is eliminated. A software library for the easy integration of the approach we propose in virtual instrumentation applications has been developed, and it is part of the QLSA public domain package [10]. While we used a high-end signal acquisition board for the measurements reported in this paper, low-cost sound boards for PC are widely available that may allow the implementation of the approach we propose at a very low cost [13]. We believe that the ability to accurately estimate the PSD over a narrow bandwidth across the resonance frequency of a QTF-based sensor may facilitate the exploration of fluctuation enhanced sensing (FES) with QTF-based sensors. Evidence of the potentialities of FES approaches in the case of quartz crystal microbalances (QCM) based on AT-cut quartz crystals can be found in the literature. In [14], for instance, it is stipulated that part of the noise observed in a 10 MHz oscillator driven by a functionalized crystal is due to the interaction of the sensing material with the chemicals in the environment. In this context, the availability of the library we have developed may contribute to the development of sensitive experiments for the exploration of FES approaches in QTF-based sensors.

Data Availability

The data used to support the findings of this study are in part included within the article and available from the corresponding author upon request. Details on the operation and usage of QLSA can be found online at http://iee1.unime.it/QLSA.

Conflicts of Interest

The authors declare that there is no conflict of interest regarding the publication of this paper.

Acknowledgments

References

[1] X. Su, C. Dai, J. Zhang, and S. J. O'Shea, "Quartz tuning fork biosensor," *Biosensors & Bioelectronics*, vol. 17, no. 1-2, pp. 111–117, 2002.

[2] M. Ren, E. S. Forzani, and N. Tao, "Chemical sensor based on microfabricated wristwatch tuning forks," *Analytical Chemistry*, vol. 77, no. 9, pp. 2700–2707, 2005.

[3] G. Scandurra, G. Cannatà, G. Giusi, and C. Ciofi, "A PC based platform for accurate quartz tuning fork characterization and sensing applications," in *2017 IEEE Sensors*, Glasgow, UK, October-November 2017.

[4] Keysight Technologies, "Spectrum Analysis Basics," *Application Note 150*, pp. 9–31, 2016, https://www.keysight.com/main/editorial.jspx?id=459160&lc=cht&cc=TW.

[5] G. Giusi, G. Scandurra, and C. Ciofi, "Estimation errors in 1/f$^{\gamma}$ NOISE spectra when employing DFT spectrum analyzers," *Fluctuation and Noise Letters*, vol. 12, no. 1, article 1350007, 2013.

[6] P. Welch, "The use of fast Fourier transform for the estimation of power spectra: a method based on time averaging over short, modified periodograms," *IEEE Transactions on Audio and Electroacoustics*, vol. 15, no. 2, pp. 70–73, 1967.

[7] G. Heinzel, A. Rüdiger, and R. Schilling, "Spectrum and spectral density estimation by the Discrete Fourier transform (DFT), including a comprehensive list of window functions ans some new flat-top windows," Internal Report, Max-Planck-Institut für Gravitationsphysik, Hannover, 2002.

[8] J. W. Cooley and J. W. Tukey, "An algorithm for the machine calculation of complex Fourier series," *Mathematics of Computation*, vol. 19, no. 90, pp. 297–301, 1965.

[9] L. Rabiner, R. Schafer, and C. Rader, "The chirp z-transform algorithm," *IEEE Transactions on Audio and Electroacoustics*, vol. 17, no. 2, pp. 86–92, 1969.

[10] C. Ciofi, G. Scandurra, and G. Giusi, "QLSA: a software library for spectral estimation in low-frequency noise measurements applications," *Fluctuation and Noise Letters*, vol. 18, article 194004, 2019.

[11] G. Scandurra, G. Giusi, and C. Ciofi, "Multichannel amplifier topologies for High-Sensitivity and reduced measurement time in voltage noise measurements," *IEEE Transactions on Instrumentation and Measurement*, vol. 62, no. 5, pp. 1145–1153, 2013.

[12] G. Giusi, G. Cannatà, G. Scandurra, and C. Ciofi, "Ultra-low-noise large-bandwidth transimpedance amplifier," *International Journal of Circuit Theory and Applications*, vol. 43, no. 10, pp. 1455–1473, 2015.

[13] G. Scandurra, G. Cannatà, G. Giusi, and C. Ciofi, "A simple and effective testbench for quartz tuning fork characterization and sensing applications," in *2015 IEEE International Instrumentation and Measurement Technology Conference (I2MTC) Proceedings*, Pisa, Italy, May 2015.

[14] L. Hasse, M. Kotarski, J. Smulko et al., "Comparison of effectiveness of gas sensing by low frequency fluctuations in resistance and microbalance quartz gas sensors," in *2011 21st International Conference on Noise and Fluctuations*, Toronto, ON, Canada, June 2011.

Research Article

Theoretical Comparison between the Flicker Noise Behavior of Graphene and of Ordinary Semiconductors

Massimo Macucci and **Paolo Marconcini**

Dipartimento di Ingegneria dell'Informazione, Universita di Pisa, Via Girolamo Caruso 16, 56122 Pisa, Italy

Correspondence should be addressed to Paolo Marconcini; p.marconcini@iet.unipi.it

Graphene is a material of particular interest for the implementation of sensors, and the ultimate performance of devices based on such a material is often determined by its flicker noise properties. Indeed, graphene exhibits, with respect to the vast majority of ordinary semiconductors, a peculiar behavior of the flicker noise power spectral density as a function of the charge carrier density. While in most materials flicker noise obeys the empirical Hooge law, with a power spectral density inversely proportional to the number of free charge carriers, in bilayer, and sometimes monolayer, graphene a counterintuitive behavior, with a minimum of flicker noise at the charge neutrality point, has been observed. We present an explanation for this stark difference, exploiting a model in which we enforce both the mass action law and the neutrality condition on the charge fluctuations deriving from trapping/detrapping phenomena. Here, in particular, we focus on the comparison between graphene and other semiconducting materials, concluding that a minimum of flicker noise at the charge neutrality point can appear only in the presence of a symmetric electron-hole behavior, a condition characteristic of graphene, but which is not found in the other commonly used semiconductors.

1. Introduction

In the actual operation of electronic devices, random fluctuations (the "noise") are always superimposed to the deterministic electrical quantity (the "signal") which conveys the desired information. Such fluctuations derive from underlying microscopic phenomena and in sensors they may limit the achievable sensitivity or, as in the case of fluctuation-enhanced sensing [1], contribute to the improvement of sensor performance, in particular in terms of selectivity. Several forms of random electrical fluctuations may exist in electronic devices: shot noise, thermal noise, generation-recombination noise, burst noise, and $1/f$ (flicker) noise, just to cite the main ones [2–9]. They differ for their physical origin and for the dependence of their power spectral density on the physical parameters characterizing the device operation, such as temperature, frequency, bias current, charge density, and material resistivity.

In particular, understanding the physical mechanisms that govern the intrinsic noise of electronic devices, and in particular of sensors, can significantly help the designer in the choice of the best material for their fabrication and of the optimal bias point for their operation.

Here, we focus on $1/f$ (flicker) noise, so called from the behavior of its power spectral density, which is inversely proportional to the frequency. This type of noise mainly originates from trapping and detrapping of charge carriers, due to impurities (traps) located inside or near the channel where the device current flows. In general, its amplitude is therefore proportional to the trap concentration.

The power spectral density of the $1/f$ current noise is often approximated with the empirical Hooge formula [10]:

$$S_I = \frac{\alpha_{\mathrm{H}} I^2}{N f},\tag{1}$$

where α_H is Hooge's constant, I is the mean bias current, N is the number of carriers in the device, and f is the frequency. According to this formula, $1/f$ noise should be greater when the number N of carriers in the device is lower. This is actually what is generally observed in ordinary semiconductors [11, 12], such as silicon or gallium arsenide. However, a different behavior has been observed in measurements performed on graphene samples.

Monolayer graphene is a recently isolated material [13] made up by a planar hexagonal lattice of carbon atoms. It is a semiconductor with a zero energy gap [14–19], even though an energy gap can be introduced, for example, by lateral confinement [20–22], strain [23, 24], doping [25–27], functionalization [28, 29], or introducing a lattice of antidots in the material layer [30, 31]. Its dispersion relations around the degeneration points between conduction and valence bands (the so-called Dirac points, i.e., the charge neutrality points) are linear and thus in graphene charge carriers present a zero effective mass. Since its isolation from graphite, it has been the focus of a large research effort (which has more recently extended to a wider family of two-dimensional materials [32–34]), because it possesses very attractive electrical, thermal, optical, and mechanical properties [35–47]. Moreover, graphene exhibits very uncommon physical phenomena [48–50], typical of relativistic mechanics, because its effective mass transport equation coincides with the Dirac equation [18, 51, 52] (the wave equation which describes relativistic spin-1/2 particles). Bilayer graphene is instead made up of two coupled graphene layers [14, 15, 53–56]. Bilayer graphene with Bernal stacking has nonlinear dispersion relations with a zero gap; however, an energy gap can be easily induced applying an orthogonal electric field, which introduces a shift between the electrochemical potentials of the two layers.

Graphene is of particular interest for the implementation of sensors because of its quasi-two-dimensional nature, which leads to a very large surface-to-volume ratio: since the interaction of a sensor with an analyte mainly occurs as a result of surface adsorption, while conduction is a bulk property, a large surface-to-volume ratio will lead to a large relative variation of resistance when the sensor interacts with the analyte.

In graphene, measurements of flicker noise power spectral density as a function of the charge density (usually tuned adjusting a gate voltage) have shown a variety of different behaviors [57–70]. While in most monolayer samples a "Λ"-shaped behavior was observed [60–63], analogous to that of common semiconductors, in suspended monolayer graphene and in most bilayer samples an "M"-shaped (or "V"-shaped) behavior was measured, with a local minimum of flicker noise near the Dirac point, where the carrier density is lowest [58, 59, 61–69], in contrast with what would be expected from Hooge's formula. Several explanations have been proposed to understand this behavior [61, 62, 64–66, 68].

An interesting theory [71] exploited the electrostatic screening of the trapped carriers and the peculiar properties of the graphene band structure to explain the observed features. We have developed a different approach [72] that leads to analogous results, exploiting a model based on the conservation of charge neutrality and on the mass action law (which has to be satisfied if the main fluctuations in flicker noise are slow compared to the generation-recombination times of carriers).

Here, we extend this model to the case of generic semiconductors, and we use it to explain the origin of this discrepancy between the behavior observed in graphene samples and that typical of common semiconductors. In particular, we show that a minimum of the $1/f$ noise at the charge neutrality point is expected in materials (such as graphene) where electrons and holes have an identical mobility, in the presence of a quite low potential disorder. This is actually the case of suspended graphene or of bilayer graphene (where the electrostatic effect of randomly located charged impurities is strongly screened). In common semiconductors, where the electron and hole behavior is in general different [50, 73], this local minimum in the flicker noise power spectral density is much less apparent and is totally suppressed by the inevitable presence of potential disorder.

2. Simulation Model

In order to relate the (microscopic) phenomena, consisting in the motion of the charge carriers and their capture and reemission by the traps to the (macroscopic) currents at the terminals of the device, we can use the Ramo-Shockley theorem [74, 75] (then generalized by Pellegrini with the electrokinematics theorem [71, 76, 77]). We assume the scattering phenomena to take place on timescales much faster than the considered trapping/detrapping events, in such a way as to be able to actually define a drift current. The current at the terminals is given by

$$
\begin{aligned}
i &= \int_A q\left(-\vec{v}_n n(x,y) + \vec{v}_p p(x,y)\right) \cdot \vec{F}(x,y)dxdy \\
&= \int_A q\left(\mu_n n(x,y) + \mu_p p(x,y)\right)\vec{E}(x,y) \cdot \vec{F}(x,y)dxdy,
\end{aligned}
\tag{2}
$$

where q is the modulus of the elementary charge; $\vec{v}_n$ and $\vec{v}_p$ are the drift velocities of electrons and holes, respectively; $\vec{F}(x,y)$ is the electric field that would be produced in the point with coordinates (x,y) by a unit potential applied to the electrode for which we want to compute the current (while the other electrode is grounded and in the absence of mobile charges) [74]; $\vec{E}(x,y)$ is the electric field actually present in the device; μ_n (μ_p) and n (p) are the mobilities and surface densities of electrons (holes); and A is the area of the device, equal to the product of the width W and the length L. Since $\vec{F}(x,y)$ is an electric field per unit applied potential, thus the ratio of an electric field to the applied potential, it has the dimension of the reciprocal of a length. The actual functional dependence of $\vec{F}(x,y)$ is influenced by the details of the contacts and by the aspect ratio of the device. The

component of $\vec{F}(x, y)$ along the drift velocity of each charge (and thus along $\vec{E}(x, y)$) represents the weight with which the carrier motion in each point of the device contributes to the total current, thus being analogous to the sensitivity coefficient introduced by Vandamme et al. [78–80]. Since for the purpose of the present study the relative weight of the contributions from the different regions of the device is not essential, we will assume a constant $\vec{F}(x, y)$ (equal to $1/L$ and parallel to $\vec{E}(x, y)$), i.e., a uniform sensitivity coefficient.

In this approximation, the instantaneous current at the contacts is given by [72]

$$i = \frac{1}{L} \int_A q \left(\mu_n n + \mu_p p \right) E dx dy. \tag{3}$$

In the case of three-dimensional devices, this integral has to be replaced with an integral over the volume V, and n and p become volumetric densities (instead of surface densities). The average current can be written as

$$I = q \left(\mu_n n + \mu_p p \right) E W. \tag{4}$$

If, as it is usually the case [71], the effect of trapping and detrapping events on carrier densities is by far prevalent with respect to that on the mobilities and on the electric field, we can express the current fluctuations due to carriers being trapped and detrapped as

$$\Delta i = \frac{1}{L} \int_A q \left(\mu_n \Delta n + \mu_p \Delta p \right) E dx dy, \tag{5}$$

where Δn and Δp are the fluctuations of electron and hole concentrations, respectively. Therefore, the ratio of the current fluctuation to the average current is equal to

$$
\begin{aligned}
\frac{\Delta i}{I} &= \frac{1}{A} \frac{\int_A \left(\mu_n \Delta n + \mu_p \Delta p \right) E dx dy}{\left(\mu_n n + \mu_p p \right) E} \\
&\simeq \frac{\mu_n \int_A \Delta n dx dy + \mu_p \int_A \Delta p dx dy}{A \left(\mu_n n + \mu_p p \right)} \\
&= \frac{\mu_n \Delta N + \mu_p \Delta P}{\mu_n N + \mu_p P},
\end{aligned}
\tag{6}
$$

where the total number of electrons and holes in the area A have been defined as $N = \int_A n dx dy$ and $P = \int_A p dx dy$, respectively, while their variations as an effect of the trapping-detrapping phenomena have been indicated with ΔN and ΔP.

In order to compute ΔN and ΔP, we use the following approach [72] (which differs from that used in Ref. [71] but leads to similar results). Let us consider a single trap, and let us define χ the number (0 or 1) of electrons in the
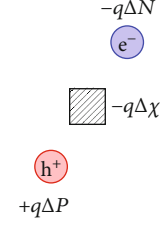

FIGURE 1: Variation $-q\Delta\chi$ of the charge in the considered trap (indicated with a square) and corresponding variations $-q\Delta N$ and $+q\Delta P$ of the charge due to the electrons and the holes in the surrounding region, which screen its electrostatic effect.

energy level of the impurity affected by the trapping events. In the following, we will indicate with Δ the variations with respect to the values with no trapped electron (i.e., when no electron is trapped all the variations Δ are zero). When an electron or a hole is trapped, the number of the corresponding charge carriers varies instantaneously by one, but, over time intervals exceeding the thermal generation-recombination time, the mass action law and electroneutrality must be satisfied. Therefore, for a generic variation $\Delta\chi$ of the number χ of electrons in the trap ($\Delta\chi = \chi$, since $\Delta\chi = 0$ if no electron is trapped, while $\Delta\chi = 1$ if one electron is trapped), the variations ΔN and ΔP of carriers in the device have to satisfy

$$
\begin{cases}
N\Delta P + P\Delta N = 0, \\
\Delta P - \Delta N - \Delta\chi = 0.
\end{cases}
\tag{7}
$$

The first relation of Equation (7) can be obtained differentiating the relation $PN = c$ (i.e., the mass action law with both members multiplied by the square of the area A). (Equivalently, it can be obtained noting that the mass action law has to be valid both before and after the examined trapping event. Therefore, both $(\Delta P + P)(\Delta N + N) = c$ and $PN = c$ have to be satisfied; subtracting the two equations and neglecting the second-order term $\Delta P \Delta N$ with respect to the other ones, the first relation of Equation (7) is obtained.) The quantity c is a constant which generally depends on the type of semiconductor and on the temperature, and thus, it does not change as a consequence of trapping events. Even in the case of graphene, in which c depends also on the position of the Fermi level [81], we can assume its variation due to a trapping event to be negligible.

The second relation of Equation (7) enforces the electroneutrality of the device: assuming that the overall device, including the bias electrodes, was neutral before the examined event, the total change of charge deriving from the trapping event has to be zero: $q\Delta P - q(\Delta N + \Delta\chi) = 0$ (see Figure 1), where we have included the variations in the number of free holes, of free electrons, and of electrons captured by the trap, which all contribute to the total charge.

The system of Equation (7) has the following solutions:

$$\Delta N = -\frac{N}{P+N}\Delta\chi,$$
$$\Delta P = \frac{P}{P+N}\Delta\chi. \tag{8}$$

In these solutions, the quantities N and P appear only through their ratio; therefore, the exact choice of the area where N and P are evaluated is irrelevant.

As can be seen from Equations (7) and (8), the necessity to satisfy both the mass action law and electroneutrality uniquely determines the values of the variations ΔN and ΔP deriving from a trapping event: these electron and hole fluctuations are therefore fully correlated.

Substituting these expressions into Equation (6), we obtain

$$\frac{\Delta i}{I} = \frac{\mu_n(\Delta N/\Delta\chi) + \mu_p(\Delta P/\Delta\chi)}{A\left(\mu_n n + \mu_p p\right)}\Delta\chi$$
$$= \frac{1}{A\left(\mu_n n + \mu_p p\right)}\frac{\mu_p P - \mu_n N}{P+N}\Delta\chi. \tag{9}$$

Therefore, for a single trap, we have (S_I is the flicker noise power spectral density):

$$\frac{S_I}{I^2} = \left(\frac{\mu_n(\Delta N/\Delta\chi) + \mu_p(\Delta P/\Delta\chi)}{A\left(\mu_n n + \mu_p p\right)}\right)^2 S_\chi$$
$$= \left(\frac{1}{A\left(\mu_n n + \mu_p p\right)}\frac{\mu_p P - \mu_n N}{P+N}\right)^2 S_\chi, \tag{10}$$

where, neglecting the contribution of the average value, S_χ has a Lorentzian dependence on frequency, with a characteristic relaxation time (since $\Delta\chi$ is a random telegraph signal) [82].

If we suppose the many traps present in the device to be reciprocally independent, the overall noise spectrum can be obtained summing up their spectra. The combination of the effects of traps with properly distributed time constants leads then to $1/f$ noise [83, 84]:

$$\frac{S_I}{I^2} = \frac{\eta}{A}\left(\frac{\mu_n(\Delta N/\Delta\chi) + \mu_p(\Delta P/\Delta\chi)}{\mu_n n + \mu_p p}\right)^2\frac{1}{f^\gamma}$$
$$= \frac{\eta}{A}\left(\frac{1}{\mu_n n + \mu_p p}\frac{\mu_p P - \mu_n N}{P+N}\right)^2\frac{1}{f^\gamma}, \tag{11}$$

with η being a coefficient which depends on the concentration, distribution, and properties of the traps, while γ is a number close to 1.

We will report the flicker noise power spectral density as a function of $n - p$ (i.e., the charge density divided by $-q$), which in actual experiments is the quantity that can be adjusted by tuning the bias voltage of a gate capacitively coupled to the device.

From Equation (8), we can observe that if the electron concentration is much larger than that of holes, i.e., when $N \gg P$, we have $\Delta N \approx -\Delta\chi$ while $\Delta P \approx 0$, i.e., the variation in the trap charge is completely screened by electrons. In a similar way, when the hole concentration strongly dominates (i.e., $P \gg N$), $\Delta P \approx \Delta\chi$ and $\Delta N \approx 0$, which means that the trap charge variation is completely screened by holes. In intermediate conditions, the variation in the trap charge is screened by variations of both electron and hole concentrations. In particular, at the neutrality point (when $N = P$), the trap charge is screened for a half by a variation of the hole number and for the other half by an opposite variation of the electron number: $\Delta N = -\Delta\chi/2$ and $\Delta P = \Delta\chi/2$.

From Equation (11), we observe that the flicker noise power spectral density S_I vanishes when $\mu_p P - \mu_n N = 0$. The behavior of S_I is symmetrical around this point if μ_n and μ_p coincide; otherwise, such a symmetry is absent. If $\mu_n = \mu_p$, the point in which S_I vanishes and around which S_I is symmetrical is the charge neutrality point (where $N - P = 0$); this condition is obtained for a Fermi energy corresponding to the middle of the gap between the conduction and valence bands if such bands are symmetric.

The quantities N and P depend, through the energy dispersion relations, on E_F, i.e., on the relative position of the Fermi energy with respect to the local value of the potential energy. However, the nonuniform distribution of charged dopants and impurities (including the randomly located charged traps themselves) introduces a potential disorder (i.e., a random spatial variation of the potential energy) which can substantially alter this result. In order to introduce the effect of this random spatial energy variation in our calculations, for each value E_F of the Fermi energy we average our results over a Gaussian distribution of energies around E_F:

$$\frac{\langle S_I\rangle}{I^2} = \frac{\eta}{Af^\gamma}\int_{-\infty}^{+\infty}\left(\frac{\mu_n((\Delta N/\Delta\chi)(E_\text{F}+\varepsilon)) + \mu_p((\Delta P/\Delta\chi)(E_\text{F}+\varepsilon))}{\mu_n n(E_\text{F}+\varepsilon) + \mu_p p(E_\text{F}+\varepsilon)}\right)^2 P(\varepsilon)\,d(\varepsilon)$$
$$= \frac{\eta}{Af^\gamma}\int_{-\infty}^{+\infty}\left(\frac{1}{\mu_n n(E_\text{F}+\varepsilon) + \mu_p p(E_\text{F}+\varepsilon)}\frac{\mu_p P(E_\text{F}+\varepsilon) - \mu_n N(E_\text{F}+\varepsilon)}{P(E_\text{F}+\varepsilon) + N(E_\text{F}+\varepsilon)}\right)^2 P(\varepsilon)\,d\varepsilon, \tag{12}$$

where

$$P(\varepsilon) = \frac{1}{\sqrt{2\pi\sigma^2}} \exp\left(-\frac{\varepsilon^2}{2\sigma^2}\right) \tag{13}$$

represents a normalized Gaussian distribution with null average and standard deviation σ.

The standard deviation σ of this Gaussian represents an estimation of the effect on the potential profile, and thus on the relative position E_F of the Fermi energy with respect to the potential energy, of the random charged impurities which represent the sources of the potential disorder. Therefore, the value of σ does not depend only on the "strength" of the disorder sources but also on the electrostatic screening efficiency of the material, which can be estimated through the derivative $\partial(n-p)/\partial E_F$ (or from the quantum capacitance, which is proportional to it [45]). If this derivative is larger, the same charged impurities induce a smaller variation of E_F (and thus a smaller σ), since this smaller variation of E_F is sufficient to screen the electrostatic effect of impurities through an opposite variation of the mobile charge density $-q(n-p)$.

When including potential disorder, we will report the flicker noise power spectral density as a function of $\langle n - p \rangle$, i.e., $n - p$ averaged over the same Gaussian distribution of energies:

$$\langle n - p \rangle = \int_{-\infty}^{+\infty} (n(E_F + \varepsilon) - p(E_F + \varepsilon))P(\varepsilon)d\varepsilon. \tag{14}$$

The average over the potential disorder (see Equation (12)) decreases the dependence of the noise spectrum on the charge density, with a smoothing effect which increases with the disorder strength.

3. Graphene

First of all, let us analyze the case of monolayer and bilayer graphene (with Bernal stacking). In this material, the electron and hole bands are approximately symmetric and $\mu_n = \mu_p$. Therefore, Equation (6) becomes

$$\frac{\Delta i}{I} = \frac{\Delta N + \Delta P}{N + P}. \tag{15}$$

Analogous simplifications can be performed in Equations (9)–(12); for example, Equation (11) becomes

$$\frac{S_I}{I^2} = \frac{\eta}{A}\left(\frac{1}{n+p}\frac{\Delta N + \Delta P}{\Delta \chi}\right)^2 \frac{1}{f^\gamma} = \frac{\eta}{A}\left(\frac{1}{n+p}\frac{P-N}{P+N}\right)^2 \frac{1}{f^\gamma}. \tag{16}$$

For graphene, we compute the carrier concentrations n and p by integrating the product of the density of
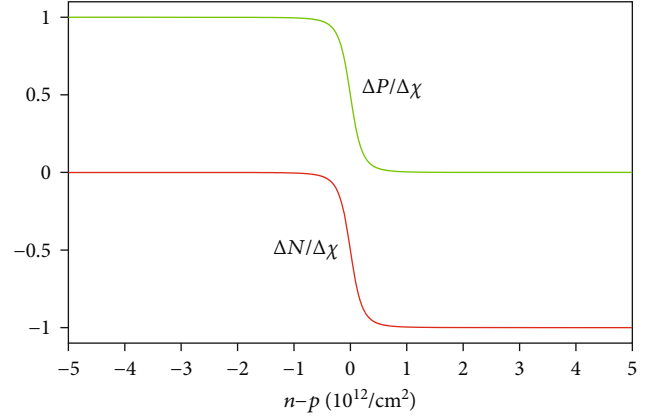

FIGURE 2: Behavior of $\Delta P/\Delta\chi$ and $\Delta N/\Delta\chi$ as a function of $n - p$, for monolayer graphene at 300 K.

states and of the occupation function over the whole energy range:

$$n = \int_0^\infty \mathrm{DOS}(E)f(E - E_F)dE,$$
$$p = \int_{-\infty}^0 \mathrm{DOS}(E)(1 - f(E - E_F))dE, \tag{17}$$

where DOS is the density of states and f is the Fermi-Dirac occupation function for electrons (therefore, $1 - f$ is the occupation function for holes). The DOS, in turn, depends on the dispersion relations of monolayer graphene or bilayer graphene, i.e. [14, 18, 53, 54]:

$$E_m(\kappa) = \pm\gamma\kappa,$$
$$E_b(\kappa) = \pm\left(\frac{\gamma_1^2}{2} + \frac{\Delta^2}{4} + \gamma^2\kappa^2 - \sqrt{\frac{\gamma_1^4}{4} + (\gamma_1^2 + \Delta^2)\gamma^2\kappa^2}\right)^{1/2}, \tag{18}$$

where κ is the difference between the wave vector and the Dirac point, $\gamma = \hbar v_F$ (with $\hbar$ the reduced Planck constant and $v_F = 8.73 \times 10^5$ m/s the Fermi velocity of graphene), $\gamma_1 = 0.39$ eV is the graphene interlayer coupling, and Δ (the term which is responsible of the possible band gap opening) is the difference between the on-site energies in the two layers, which is approximately proportional to the carrier concentration $n - p$ (more in detail, $\Delta \approx 1.4 \times 10^{-18}$ eV m$^2 \times (n - p)$).

In Figures 2–5, we report some results obtained for graphene at 300 K, without potential disorder averaging. Figures 2 and 3 refer to monolayer graphene, while Figures 4 and 5 refer to bilayer graphene.

In Figures 2 and 4, we report the quantities $\Delta P/\Delta\chi$ and $\Delta N/\Delta\chi$ (evaluated from Equation (8)) as a function of $n - p$ (for monolayer and bilayer graphene, respectively). As in the general case, the charge variation in the traps is mainly screened by holes when the holes are the dominant carriers, while it is mainly screened by electrons when the
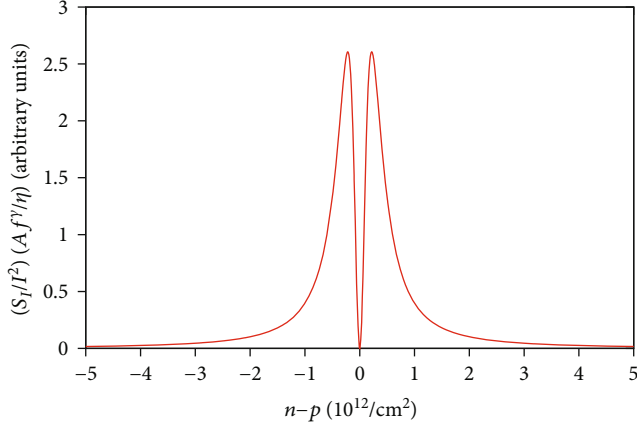
FIGURE 3: Behavior of $(S_I/I^2)(Af^\gamma/\eta)$ as a function of $n - p$, for monolayer graphene at 300 K, in the absence of potential disorder.
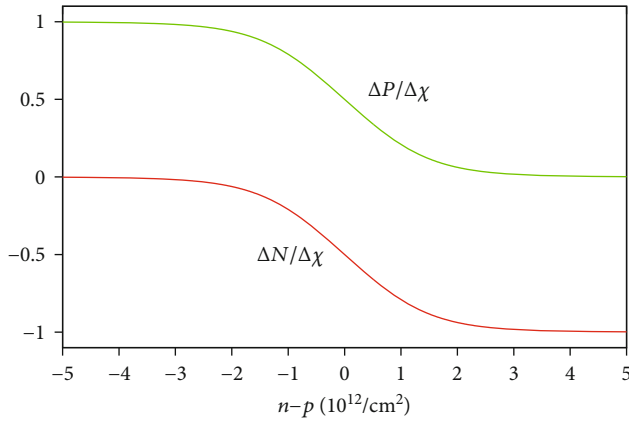

FIGURE 4: Behavior of $\Delta P/\Delta\chi$ and $\Delta N/\Delta\chi$ as a function of $n - p$, for bilayer graphene at 300 K.
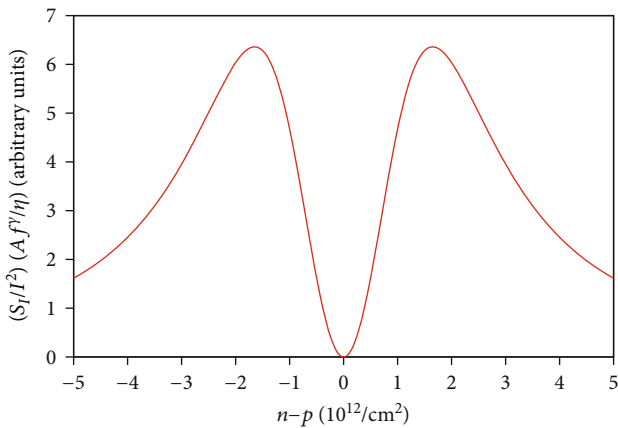

FIGURE 5: Behavior of $(S_I/I^2)(Af^\gamma/\eta)$ as a function of $n - p$, for bilayer graphene at 300 K, in the absence of potential disorder.

FIGURE 6: Behavior of $(\langle S_I \rangle/I^2)(Af^\gamma/\eta)$ as a function of $\langle n - p \rangle$, for monolayer graphene at 300 K. The averages have been performed over four Gaussian distributions of potential disorder with standard deviations $\sigma = 10, 20, 30$, and 40 meV, respectively.
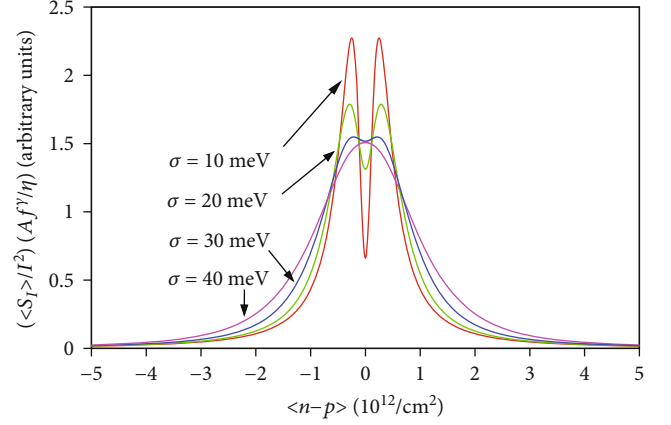

FIGURE 7: Behavior of $(\langle S_I \rangle/I^2)(Af^\gamma/\eta)$ as a function of $\langle n - p \rangle$, for bilayer graphene at 300 K. The averages have been performed over four Gaussian distributions of potential disorder with standard deviations $\sigma = 10, 20, 30$, and 40 meV, respectively.

In Figures 3 and 5, we report the quantity $(S_I/I^2)(Af^\gamma/\eta)$ (evaluated from Equation (11)) as a function of $n - p$ (for monolayer and bilayer graphene, respectively). Since in graphene $\mu_n = \mu_p$, the behavior of the flicker noise power spectral density is exactly symmetrical with respect to the neutrality point. In particular, in the charge neutrality point (Dirac point), where $\Delta N = -\Delta\chi/2$ and $\Delta P = \Delta\chi/2$, the fluctuation of the current (and therefore the noise power spectral density) completely vanishes (see Equation (16)). Comparing Figures 3 and 5, we notice that the dip around the Dirac point is wider in bilayer graphene than in monolayer graphene, as a consequence of their different dispersion relations.

In Figures 6 and 7, we show analogous results obtained averaging the spectrum of monolayer (Figure 6) and bilayer (Figure 7) graphene at 300 K over potential disorder. In particular, we report the value of $(\langle S_I \rangle/I^2)(Af^\gamma/\eta)$ (i.e., the integral appearing in Equation (12)) as a function of $\langle n - p \rangle$ (i.e., the charge density divided by the electron charge,

electrons are the dominant carriers. It is instead symmetrically screened by electrons and holes in the charge neutrality point.

averaged according to Equation (14)). Both for monolayer and bilayer graphene, we show the results for the following four different values of σ: 10, 20, 30, and 40 meV. In both cases, we observe that the minimum of the spectrum at the charge neutrality point tends to disappear increasing the strength of the disorder: therefore, the behavior of the flicker noise power spectral density evolves from an "M"-shaped one to a "Λ"-shaped one. However, as we can deduce from the corresponding values of $\partial(n - p)/\partial E_F$ (which in the charge neutrality point is equal to about 7×10^{12} cm^{-2} eV^{-1} in monolayer graphene and to about 44×10^{12} cm^{-2} eV^{-1} in bilayer graphene), the screening of potential fluctuations is about six times larger in bilayer graphene than in monolayer graphene. This is a consequence of the different dispersion relations of the two materials, with bilayer graphene characterized by flatter bands near the Dirac points [50]. Therefore, for similar impurity distributions, values of σ should be considered for monolayer graphene that are approximately six times larger than those considered for bilayer graphene. As a consequence, for realistic values of disorder, monolayer graphene does not usually exhibit a minimum of the flicker noise power spectral density at the charge neutrality point. On the contrary, in sufficiently clean samples of bilayer graphene, an "M"-shaped behavior is often observed, with a minimum at the Dirac point. A similar "M"-shaped behavior has been observed also in the case of suspended monolayer graphene, for which potential disorder is much weaker than for monolayer graphene on a substrate.

4. Ordinary Semiconductors

Let us now move on to the case of ordinary semiconductors, such as silicon and gallium arsenide, for which a minimum of the flicker noise power spectral density at the charge neutrality point has never been experimentally observed.

Also in this case, we can adopt the numerical procedure described in Section 2, substituting (in the case of 3-dimensional channels) areas with volumes. In order to simplify the calculations and to reach general results, we neglect the details of the band structure of the materials and, assuming a constant effective mass, we use the semiclassical expressions for the carrier concentrations [85, 86]:

$$
\begin{aligned}
n &= N_C \exp\left(-\frac{E_C - E_F}{k_B T}\right), \\
p &= N_V \exp\left(-\frac{E_F - E_V}{k_B T}\right),
\end{aligned}
\tag{19}
$$

where E_C is the conductance band minimum, E_V is the valence band maximum, k_B is the Boltzmann constant, and T is the absolute temperature.

In particular, we perform our calculations using the material parameters for silicon and for gallium arsenide.

For silicon, we consider the following parameters: $N_C = 2.82 \times 10^{19}$ cm^{-3}, $N_V = 1.04 \times 10^{19}$ cm^{-3}, $E_G = 1.12$ eV, $\mu_p = 450$ cm^2/(V s), and $\mu_n = 1400$ cm^2/(V s).

FIGURE 8: Behavior of $\Delta P/\Delta\chi$ and $\Delta N/\Delta\chi$ as a function of $n - p$, for silicon at 300 K.

FIGURE 9: Behavior of $(S_I/I^2)(Af^\gamma/\eta)$ as a function of $n - p$, for silicon at 300 K, in the absence of potential disorder.

Instead, for gallium arsenide, we assume the following: $N_C = 4.7 \times 10^{17}$ cm^{-3}, $N_V = 7.0 \times 10^{18}$ cm^{-3}, $E_G = 1.42$ eV, $\mu_p = 400$ cm^2/(V s), and $\mu_n = 8500$ cm^2/(V s).

In Figures 8 and 9, we report the results obtained for silicon at 300 K without potential disorder averaging. More in detail, in Figure 8, we show the ratios $\Delta P/\Delta\chi$ and $\Delta N/\Delta\chi$ (evaluated according to Equation (8)) as a function of $n - p$, while in Figure 9, we report the behavior of the quantity $(S_I/I^2)(Af^\gamma/\eta)$ (evaluated according to Equation (11)) as a function of $n - p$.

In Figures 10 and 11, we report the analogous results for gallium arsenide at 300 K without potential disorder averaging.

As we see from the reported parameters, contrary to graphene, these semiconductors have quite different mobilities for electrons and holes. This is the reason of the clear asymmetry observed in the results, with a larger noise spectrum in the region where transport is dominated by electrons, i.e., the carriers with higher mobility. We can also observe that the asymmetry is stronger in gallium arsenide, for which the difference between electron and hole mobility is larger. Due to

FIGURE 10: Behavior of $\Delta P/\Delta \chi$ and $\Delta N/\Delta \chi$ as a function of $n - p$, for gallium arsenide at 300 K.

FIGURE 11: Behavior of $(S_I/I^2)(Af^\gamma/\eta)$ as a function of $n - p$, for gallium arsenide at 300 K, in the absence of potential disorder.
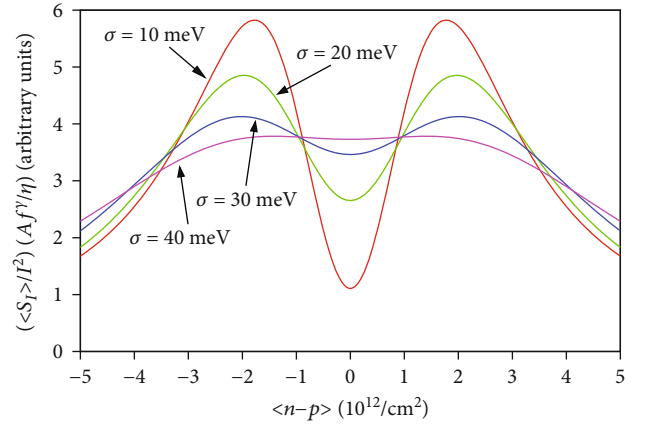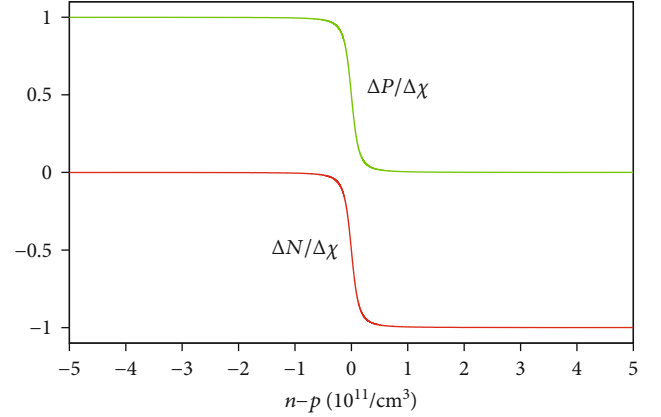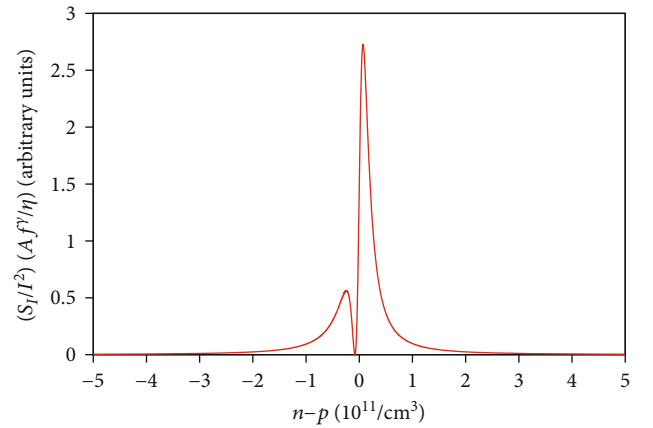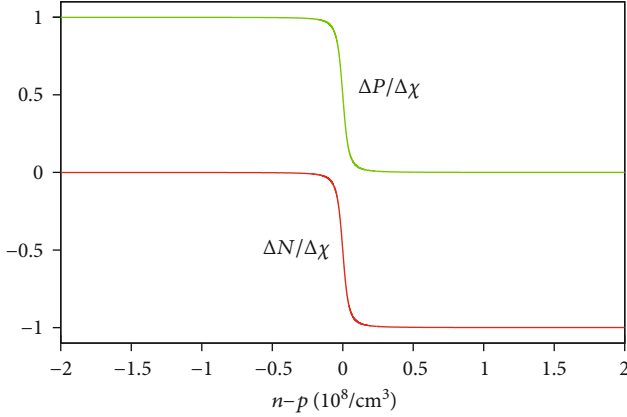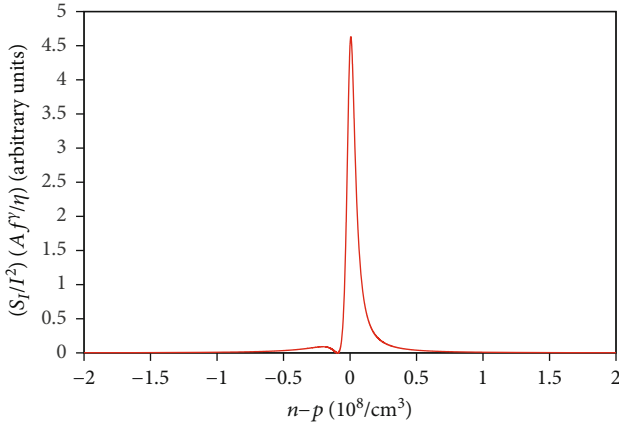

FIGURE 12: Behavior of $(\langle S_I \rangle/I^2)(Af^\gamma/\eta)$ as a function of $\langle n - p \rangle$, for silicon at 300 K. The averages have been performed over four Gaussian distributions of potential disorder with standard deviations $\sigma = 10$, 20, 30, and 40 meV, respectively.
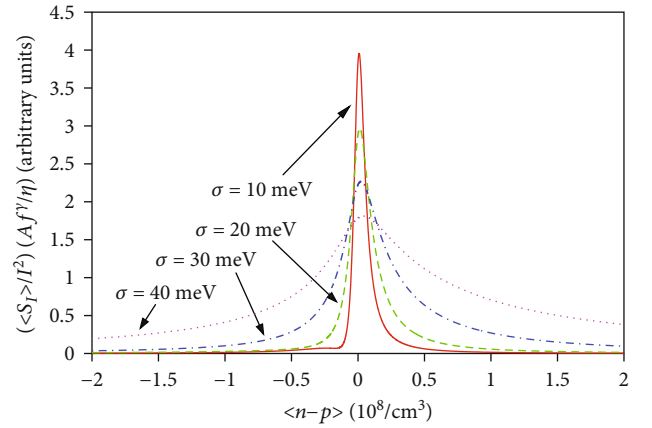
FIGURE 13: Behavior of $(\langle S_I \rangle/I^2)(Af^\gamma/\eta)$ as a function of $\langle n - p \rangle$, for gallium arsenide at 300 K. The averages have been performed over four Gaussian distributions of potential disorder with standard deviations $\sigma = 10$, 20, 30, and 40 meV, respectively.

the difference in mobility, the spectrum does not vanish any more at the charge neutrality point (where $n - p = 0$) but where $\mu_p P - \mu_n N = 0$. Moreover, with respect to graphene (for which, in the absence of disorder, this vanishing point presented a sharp reduction of the spectrum with respect to both the hole-dominated and the electron-dominated conduction regions), here, due to the spectrum asymmetry, the minimum point is much less prominent. Indeed, especially in the case of gallium arsenide, it is nearly indistinguishable from the hole-dominated region, where the spectrum is already very low.

Therefore, when the effect of potential disorder is introduced, by averaging over a Gaussian energy distribution with standard deviation σ according to Equation (12), the local minimum of the spectrum completely disappears and the spectrum exhibits a "Λ" shape, with a maximum centered in the electron-dominated region, where the mobility is larger. The behavior of $(\langle S_I \rangle/I^2)(Af^\gamma/\eta)$ (i.e., the integral appearing in Equation (12)) as a function of $\langle n - p \rangle$ (given by Equation (14)) is reported in Figures 12 and 13, at 300 K, for silicon and for gallium arsenide, respectively, for four different values of σ: 10, 20, 30, and 40 meV. The described behavior is observed for both semiconductors but

is even more apparent in the case of gallium arsenide, for which a minimum in the spectrum was already hard to recognize in the absence of disorder.

The fact that in a real three-dimensional material it is difficult, if not impossible, to modulate the position of the Fermi level uniformly in the whole volume, further prevents a perfect balance of electron and hole current fluctuations in the overall device and thus makes it impossible to experimentally observe a flicker noise cancellation analogous to that described for graphene.

5. Conclusions

Exploiting a model based on charge neutrality and on the mass action law, we have compared the flicker noise behavior of graphene and of more common semiconductors, such as silicon and gallium arsenide. We have concluded that a minimum of the flicker noise power spectral density can be

observed at the charge neutrality point only in materials where electrons and holes have a highly symmetric transport behavior, in particular have approximately the same mobility (the case of graphene), and only if the potential disorder is low. When these conditions are satisfied, the opposite variations of electron and hole concentrations induced by trapping phenomena reciprocally cancel, leading to no current fluctuations. Instead, in the presence of electron/hole asymmetry (the case of ordinary semiconductors) or of a significant degree of potential disorder, such a minimum disappears.

We believe that this analysis, clarifying the mechanisms that cause or prevent a reduction, at proper bias conditions, of the intrinsic device flicker noise, can be useful for the design of low-noise devices and in particular of high-sensitivity sensors.

Data Availability

The numerical data used to support the findings of this study are available from the corresponding author upon request.

Conflicts of Interest

The authors declare no conflict of interest.

Acknowledgments

References

[1] G. Schmera, C. Kwan, P. Ajayan, R. Vajtai, and L. B. Kish, "Fluctuation-enhanced sensing: status and perspectives," *IEEE Sensors Journal*, vol. 8, no. 6, pp. 714–719, 2008.

[2] A. Van der Ziel, *Noise in Solid State Devices and Circuits*, Wiley-Interscience, New York, NY, USA, 1986.

[3] A. Van der Ziel, *Noise in Measurements*, Wiley, New York, NY, USA, 1976.

[4] C. D. Motchenbacher and J. A. Connelly, *Low-Noise Electronic System Design*, Wiley-Interscience, New York, NY, USA, 1993.

[5] Y. M. Blanter and M. Büttiker, "Shot noise in mesoscopic conductors," *Physics Reports*, vol. 336, no. 1-2, pp. 1–166, 2000.

[6] F. N. Hooge, T. G. M. Kleinpenning, and L. K. J. Vandamme, "Experimental studies on 1/f noise," *Reports on Progress in Physics*, vol. 44, no. 5, pp. 479–532, 1981.

[7] M. Macucci and P. Marconcini, "Origin of shot noise in mesoscopic cavities," *Fluctuation and Noise Letters*, vol. 15, no. 3, p. 1640006, 2016.

[8] M. Macucci and P. Marconcini, "Shot noise suppression due to a magnetic field in disordered conductors," *Journal of Computational Electronics*, vol. 14, no. 1, pp. 107–113, 2015.

[9] P. Marconcini, M. Totaro, G. Basso, and M. Macucci, "Effect of potential fluctuations on shot noise suppression in mesoscopic cavities," *AIP Advances*, vol. 3, no. 6, article 062131, 2013.

[10] F. N. Hooge, "1/f noise is no surface effect," *Physics Letters A*, vol. 29, no. 3, pp. 139-140, 1969.

[11] A. Van der Ziel, "Flicker noise in electronic devices," in *Advances in Electronics and Electron Physics*, L. Marton and C. Marton, Eds., vol. 49, pp. 225–297, Academic Press, New York, NY, USA, 1979.

[12] F. Hofman and R. J. J. Zijlstra, "The validity of Hooge's law for 1/f noise," *Solid State Communications*, vol. 72, no. 12, pp. 1163–1166, 1989.

[13] K. S. Novoselov, A. K. Geim, S. V. Morozov et al., "Electric field effect in atomically thin carbon films," *Science*, vol. 306, no. 5696, pp. 666–669, 2004.

[14] A. H. Castro Neto, F. Guinea, N. M. R. Peres, K. S. Novoselov, and A. K. Geim, "The electronic properties of graphene," *Reviews of Modern Physics*, vol. 81, no. 1, pp. 109–162, 2009.

[15] M. I. Katsnelson, *Graphene: Carbon in Two Dimensions*, Cambridge University Press, Cambridge, UK, 2012.

[16] L. E. F. Foa Torres, S. Roche, and J.-C. Charlier, *Introduction to Graphene-Based Nanomaterials: From Electronic Structure to Quantum Transport*, Cambridge University Press, Cambridge, UK, 2014.

[17] T. Enoki and T. Ando, *Physics and Chemistry of Graphene: Graphene to Nanographene*, Pan Stanford, Boca Raton, FL, USA, 2014.

[18] P. Marconcini and M. Macucci, "The k·p method and its application to graphene, carbon nanotubes and graphene nanoribbons: the Dirac equation," *La Rivista del Nuovo Cimento*, vol. 34, no. 8-9, pp. 489–584, 2011.

[19] T. Ando, "Theory of electronic states and transport in carbon nanotubes," *Journal of the Physical Society of Japan*, vol. 74, no. 3, pp. 777–817, 2005.

[20] L. Brey and H. A. Fertig, "Electronic states of graphene nanoribbons studied with the Dirac equation," *Physical Review B*, vol. 73, no. 23, p. 235411, 2006.

[21] Y.-W. Son, M. L. Cohen, and S. G. Louie, "Energy gaps in graphene nanoribbons," *Physical Review Letters*, vol. 97, no. 21, p. 216803, 2006.

[22] D. Logoteta, P. Marconcini, C. Bonati, M. Fagotti, and M. Macucci, "High-performance solution of the transport problem in a graphene armchair structure with a generic potential," *Physical Review E*, vol. 89, no. 6, article 063309, 2014.

[23] G. Gui, J. Li, and J. Zhong, "Band structure engineering of graphene by strain: first-principles calculations," *Physical Review B*, vol. 78, no. 7, article 075435, 2008.

[24] Z. H. Ni, T. Yu, Y. H. Lu, Y. Y. Wang, Y. P. Feng, and Z. X. Shen, "Uniaxial strain on graphene: Raman spectroscopy study and band-gap opening," *ACS Nano*, vol. 2, no. 11, pp. 2301–2305, 2008.

[25] P. Marconcini, A. Cresti, F. Triozon et al., "Atomistic boron-doped graphene field-effect transistors: a route toward unipolar characteristics," *ACS Nano*, vol. 6, no. 9, pp. 7942–7947, 2012.

[26] P. Marconcini, A. Cresti, and S. Roche, "Effect of the channel length on the transport characteristics of transistors based on boron-doped graphene ribbons," *Materials*, vol. 11, no. 5, p. 667, 2018.

[27] D. Wei, Y. Liu, Y. Wang, H. Zhang, L. Huang, and G. Yu, "Synthesis of N-doped graphene by chemical vapor deposition and its electrical properties," *Nano Letters*, vol. 9, no. 5, pp. 1752–1758, 2009.

[28] D. W. Boukhvalov and M. I. Katsnelson, "Tuning the gap in bilayer graphene using chemical functionalization: density functional calculations," *Physical Review B*, vol. 78, no. 8, article 085413, 2008.

[29] D. C. Elias, R. R. Nair, T. M. G. Mohiuddin et al., "Control of graphene's properties by reversible hydrogenation: evidence for graphane," *Science*, vol. 323, no. 5914, pp. 610–613, 2009.

[30] J. A. Fürst, J. G. Pedersen, C. Flindt et al., "Electronic properties of graphene antidot lattices," *New Journal of Physics*, vol. 11, no. 9, article 095020, 2009.

[31] P. Marconcini and M. Macucci, "Envelope-function based transport simulation of a graphene ribbon with an antidot lattice," *IEEE Transactions on Nanotechnology*, vol. 16, no. 4, pp. 534–544, 2017.

[32] K. S. Novoselov, A. Mishchenko, A. Carvalho, and A. H. Castro Neto, "2D materials and van der Waals heterostructures," *Science*, vol. 353, no. 6298, p. aac9439, 2016.

[33] M. Xu, T. Liang, M. Shi, and H. Chen, "Graphene-like two-dimensional materials," *Chemical Reviews*, vol. 113, no. 5, pp. 3766–3798, 2013.

[34] L. Jiang, P. Marconcini, M. S. Hossian et al., "A tight binding and k · p study of monolayer stanene," *Scientific Reports*, vol. 7, no. 1, p. 12069, 2017.

[35] A. K. Geim and K. S. Novoselov, "The rise of graphene," *Nature Materials*, vol. 6, no. 3, pp. 183–191, 2007.

[36] K. S. Novoselov, V. I. Fal'ko, L. Colombo, P. R. Gellert, M. G. Schwab, and K. Kim, "A roadmap for graphene," *Nature*, vol. 490, no. 7419, pp. 192–200, 2012.

[37] Y. Zhu, H. Ji, H.-M. Cheng, and R. S. Ruoff, "Mass production and industrial applications of graphene materials," *National Science Review*, vol. 5, no. 1, pp. 90–101, 2018.

[38] S. Nazarpour and S. R. Waite, *Graphene Technology: From Laboratory to Fabrication*, Wiley-VCH, Weinheim, Germany, 2016.

[39] M. Sharon and M. Sharon, *Graphene: An Introduction to the Fundamentals and Industrial Applications*, John Wiley & Sons and Scrivener Publishing LLC, Hoboken, New Jersey, USA: Salem, Massachusetts, USA, 2015.

[40] F. Schwierz, "Graphene transistors: status, prospects, and problems," *Proceedings of the IEEE*, vol. 101, no. 7, pp. 1567–1584, 2013.

[41] L. Liao and X. Duan, "Graphene for radio frequency electronics," *Materials Today*, vol. 15, no. 7-8, pp. 328–338, 2012.

[42] P. Marconcini and M. Macucci, "Symmetry-dependent transport behavior of graphene double dots," *Journal of Applied Physics*, vol. 114, no. 16, p. 163708, 2013.

[43] E. D. Herbschleb, R. K. Puddy, P. Marconcini et al., "Direct imaging of coherent quantum transport in graphene p−n−p junctions," *Physical Review B*, vol. 92, no. 12, p. 125414, 2015.

[44] P. Marconcini and M. Macucci, "Numerical analysis of the resistance behavior of an electrostatically-induced graphene double junction," *Journal of Computational Electronics*, vol. 14, no. 3, pp. 653–660, 2015.

[45] M. Macucci and P. Marconcini, "Approximate calculation of the potential profile in a graphene-based device," *IET Circuits, Devices & Systems*, vol. 9, no. 1, pp. 30–38, 2015.

[46] P. Marconcini and M. Macucci, "Geometry-dependent conductance and noise behavior of a graphene ribbon with a series of randomly spaced potential barriers," *Journal of Applied Physics*, vol. 125, no. 24, p. 244302, 2019.

[47] M. Fagotti, C. Bonati, D. Logoteta, P. Marconcini, and M. Macucci, "Armchair graphene nanoribbons: PT-symmetry breaking and exceptional points without dissipation," *Phys. Rev. B*, vol. 83, no. 24, article 241406, 2011.

[48] M. I. Katsnelson and K. S. Novoselov, "Graphene: new bridge between condensed matter physics and quantum electrodynamics," *Solid State Communications*, vol. 143, no. 1-2, pp. 3–13, 2007.

[49] A. Shytov, M. Rudner, N. Gu, M. Katsnelson, and L. Levitov, "Atomic collapse, Lorentz boosts, Klein scattering, and other quantum-relativistic phenomena in graphene," *Solid State Communications*, vol. 149, no. 27-28, pp. 1087–1093, 2009.

[50] M. I. Katsnelson, K. S. Novoselov, and A. K. Geim, "Chiral tunnelling and the Klein paradox in graphene," *Nature Physics*, vol. 2, no. 9, pp. 620–625, 2006.

[51] K. S. Novoselov, A. K. Geim, S. V. Morozov et al., "Two-dimensional gas of massless Dirac fermions in graphene," *Nature*, vol. 438, no. 7065, pp. 197–200, 2005.

[52] D. P. DiVincenzo and E. J. Mele, "Self-consistent effective-mass theory for intralayer screening in graphite intercalation compounds," *Physical Review B*, vol. 29, no. 4, pp. 1685–1694, 1984.

[53] E. McCann, "Asymmetry gap in the electronic band structure of bilayer graphene," *Physical Review B*, vol. 74, no. 16, article 161403, 2006.

[54] E. McCann and M. Koshino, "The electronic properties of bilayer graphene," *Reports on Progress in Physics*, vol. 76, no. 5, p. 056503, 2013.

[55] A. V. Rozhkov, A. O. Sboychakov, A. L. Rakhmanov, and F. Nori, "Electronic properties of graphene-based bilayer systems," *Physics Reports*, vol. 648, pp. 1–104, 2016.

[56] M. R. Connolly, R. K. Puddy, D. Logoteta et al., "Unraveling quantum hall breakdown in bilayer graphene with scanning gate microscopy," *Nano Letters*, vol. 12, no. 11, pp. 5448–5454, 2012.

[57] A. A. Balandin, "Low-frequency 1/f noise in graphene devices," *Nature Nanotechnology*, vol. 8, no. 8, pp. 549–555, 2013.

[58] Y. Lin and P. Avouris, "Strong suppression of electrical noise in bilayer graphene nanodevices," *Nano Letters*, vol. 8, no. 8, pp. 2119–2125, 2008.

[59] Q. Shao, G. Liu, D. Teweldebrhan et al., "Flicker noise in bilayer graphene transistors," *IEEE Electron Device Letters*, vol. 30, no. 3, pp. 288–290, 2009.

[60] A. N. Pal, A. A. Bol, and A. Ghosh, "Large low-frequency resistance noise in chemical vapor deposited graphene," *Applied Physics Letters*, vol. 97, no. 13, p. 133504, 2010.

[61] S. Rumyantsev, G. Liu, W. Stillman, M. Shur, and A. A. Balandin, "Electrical and noise characteristics of graphene field-effect transistors: ambient effects, noise sources and physical mechanisms," *Journal of Physics: Condensed Matter*, vol. 22, no. 39, p. 395302, 2010.

[62] A. N. Pal, S. Ghatak, V. Kochat et al., "Microscopic mechanism of 1/f noise in graphene: role of energy band dispersion," *ACS Nano*, vol. 5, no. 3, pp. 2075–2081, 2011.

[63] A. N. Pal and A. Ghosh, "Ultralow noise field-effect transistor from multilayer graphene," *Applied Physics Letters*, vol. 95, no. 8, article 082105, 2009.

[64] G. Xu, C. M. Torres Jr., Y. Zhang et al., "Effect of spatial charge inhomogeneity on 1/f noise behavior in graphene," *Nano Letters*, vol. 10, no. 9, pp. 3312–3317, 2010.

[65] I. Heller, S. Chatoor, J. Männik et al., "Charge noise in graphene transistors," *Nano Letters*, vol. 10, no. 5, pp. 1563–1567, 2010.

[66] Y. Zhang, E. E. Mendez, and X. Du, "Mobility-dependent low-frequency noise in graphene field-effect transistors," *ACS Nano*, vol. 5, no. 10, pp. 8124–8130, 2011.

[67] A. N. Pal and A. Ghosh, "Resistance noise in electrically biased bilayer graphene," *Physical Review Letters*, vol. 102, no. 12, p. 126805, 2009.

[68] A. A. Kaverzin, A. S. Mayorov, A. Shytov, and D. W. Horsell, "Impurities as a source of 1/f noise in graphene," *Physical Review B*, vol. 85, no. 7, article 075435, 2012.

[69] M. Z. Hossain, S. Rumyantsev, M. S. Shur, and A. A. Balandin, "Reduction of 1/f noise in graphene after electron-beam irradiation," *Applied Physics Letters*, vol. 102, no. 15, p. 153512, 2013.

[70] G. Liu, S. Rumyantsev, M. S. Shur, and A. A. Balandin, "Origin of 1/f noise in graphene multilayers: surface vs. volume," *Applied Physics Letters*, vol. 102, no. 9, p. 093111, 2013.

[71] B. Pellegrini, "1/f noise in graphene," *The European Physical Journal B*, vol. 86, no. 9, p. 373, 2013.

[72] B. Pellegrini, P. Marconcini, M. Macucci, G. Fiori, and G. Basso, "Carrier density dependence of 1/f noise in graphene explained as a result of the interplay between band-structure and inhomogeneities," *Journal of Statistical Mechanics: Theory and Experiment*, vol. 2016, no. 5, article 054017, 2016.

[73] S. V. Vonsovsky and M. I. Katsnelson, *Quantum Solid-State Physics*, Springer, Berlin, Heidelberg, Germany, 1989.

[74] W. Shockley, "Currents to conductors induced by a moving point charge," *Journal of Applied Physics*, vol. 9, no. 10, pp. 635-636, 1938.

[75] S. Ramo, "Currents induced by electron motion," *Proceedings of the IRE*, vol. 27, no. 9, pp. 584-585, 1939.

[76] B. Pellegrini, "Electric charge motion, induced current, energy balance, and noise," *Physical Review B*, vol. 34, no. 8, pp. 5921–5924, 1986.

[77] B. Pellegrini, "Extension of the electrokinematics theorem to the electromagnetic field and quantum mechanics," *Il Nuovo Cimento D*, vol. 15, no. 6, pp. 855–879, 1993.

[78] L. K. J. Vandamme and W. M. G. van Bokhoven, "Conductance noise investigations with four arbitrarily shaped and placed electrodes," *Applied Physics*, vol. 14, no. 2, pp. 205–215, 1977.

[79] L. K. J. Vandamme and A. H. de Kuijper, "Conductance noise investigations on symmetrical planar resistors with finite contacts," *Solid State Electronics*, vol. 22, no. 11, pp. 981–986, 1979.

[80] G. Leroy, J. Gest, L. K. J. Vandamme, and A. P. J. van Deursen, "Analytical expressions for the conductance noise measured with four circular contacts placed in a square array," *Journal of Applied Physics*, vol. 101, no. 6, article 063710, 2007.

[81] T. Fang, A. Konar, H. Xing, and D. Jena, "Carrier statistics and quantum capacitance of graphene sheets and ribbons," *Applied Physics Letters*, vol. 91, no. 9, p. 092109, 2007.

[82] S. Machlup, "Noise in semiconductors: spectrum of a two-parameter random signal," *Journal of Applied Physics*, vol. 25, no. 3, pp. 341–343, 1954.

[83] A. L. McWhorter, "1/f noise and germanium surface properties," in *In Semiconductor Surface Physics*, R. H. Kingston, Ed., pp. 207–228, University of Pennsylvania Press, Philadelphia, PA, USA, 1957.

[84] B. Pellegrini, "A general model of 1/f$^\gamma$ noise," *Microelectronics Reliability*, vol. 40, no. 11, pp. 1775–1780, 2000.

[85] S. M. Sze and K. K. Ng, *Physics of Semiconductor Devices*, Wiley, Hoboken, NJ, USA, 2007.

[86] S. O. Kasap, *Principles of Electronic Materials and Devices*, McGraw-Hill, New York, NY, USA, 2018.

Research Article

Thermal Noise-Boosting Effects in Hot-Wire-Based Micro Sensors

Massimo Piotto [iD],[1,2] **Alessandro Catania,**[1] **Andrea Nannini,**[1] **and Paolo Bruschi** [iD][1,2]

[1]*Dipartimento di Ingegneria dell'Informazione, University of Pisa, 56122 Pisa, Italy*
[2]*IEIIT-PISA, CNR, 56122 Pisa, Italy*

Correspondence should be addressed to Paolo Bruschi; paolo.bruschi@unipi.it

This article proposes an original approach aimed at modelling the noise density in sensors based on a single hot wire or pairs of thermally coupled wires. The model consists in an original combination of a previous electrothermal model of the wire with well-established assumptions on the thermal noise in conductors that carry moderate current densities. A simple method for estimating the model parameters with simple impedance spectroscopy is suggested. The predicted power spectral densities of the wire thermal noise differ from the result of previously presented analytical models, stimulating further experimental studies. The effects of the electrothermal feedback of both hot wires and hot-wire pairs on flicker noise is also intrinsically covered by the proposed approach.

1. Introduction

Hot wires are used in a large variety of sensing devices and instruments. They consist of thin wires of an electrical conductor that, once biased with a sufficiently large current, reach a temperature that is significantly larger than ambient temperature. Hot wires are generally suspended at the extremities and immersed in a fluid. The category of hot-wire devices includes hot films, which consist of a thin or thick conducting stripe deposited over a thermally and electrically insulating substrate. The temperature difference between the wire and the fluid (overheating) is detected exploiting the dependence of the electrical resistance on temperature. Measuring the overheating, it is possible to detect several quantities of interest. Sensors based on hot wires gained significant importance since they can be easily fabricated using MEMS (Microelectromechanical Systems) technologies that allowed extreme miniaturization leading to reduction of the power consumption and response time of up to three orders of magnitude with respect to traditional macroscopic devices.

Among the sensors that exploit this principle are vacuum sensors [1–3], gas concentration sensors [4], thermal conductivity probes [5], and anemometers [6–8]. An evolution of the single hot wire is represented by the pair of thermally coupled wires. These devices are formed by two hot wires placed at micrometric distances from each other, so that substantial thermal exchange occurs between them. Such an arrangement allows detection of both the magnitude and direction of airflows [9]. Recently, wire pairs with thermal mass as small as to allow temperature variations with frequencies up to several kHz have been used to detect the local fluid displacement induced by an acoustic wave [10–13]. In particular, this new class of sensors is capable of directly detecting the acoustic particle velocity (APV), enabling interesting applications that cannot be easily achieved with standard microphones [14]. In all the mentioned applications of hot wires, it is of primary importance to model the electrical noise produced by the wire, in order to estimate the actual resolution of the sensors. This aspect is very critical for the APV sensors, which are marked by relatively low sensitivities resulting in low signal-to-noise ratios even in the presence of large sound intensities.

Noise in electrical conductors supplied with a dc current is due to two main phenomena, namely, thermal agitation of the charge carriers (Johnson-Nyquist noise or thermal noise) and resistance fluctuations, resulting in the well-known flicker noise. Thermal noise is universal and is related only to the wire resistance and temperature, while flicker noise is strongly material-dependent. Both types of noise cause

fluctuations of the current and voltage of the wire, resulting in small fluctuations of the heating power.

In hot wires, these power fluctuations have to be taken into account because they generate nonnegligible temperature fluctuations, due to the high thermal isolation of the conductor. The high TCR (temperature coefficient of resistance) of the wire material transforms the temperature fluctuations again into voltage and current variations, in a loop. The effect of this thermoelectrical feedback on the noise density has not been studied extensively so far, maybe because the thermal capacity of macroscopic hot wires allows development of temperature fluctuations only in the range of ultralow frequencies (typically sub-1 Hz). This is no more the case for MEMS sensors, where cut-off frequencies in the kHz range are common. This electrothermal feedback was described previously by Kohl et al. [15], highlighting its consequences on the sensitivity and noise of metal film resistance bolometers. The same phenomenon was observed earlier in bolometers based on superconductor materials [16].

It should be recalled that the temperature of a body is subjected to temperature fluctuation even when the cited electrothermal cause is not present. This type of "natural" temperature fluctuations is due to the so-called phonon noise and has a total mean square value equal to $<\delta T^2> = k_B T^2/C_{TH}$, where T is the body temperature, k_B the Boltzmann constant, and C_{TH} the thermal capacity of the body. Obviously, even these temperature fluctuations produce resistance fluctuations, resulting in voltage noise when the wire is biased with an electrical current. Furthermore, resistance fluctuations modulate the heating power, so that, in thermally insulated wires, the electrothermal feedback affects also phonon noise. This work is focused on the changes produced by the electrothermal feedback on thermal noise and flicker noise, with particular emphasis on the former. Therefore, analysis of phonon noise is out of the scope of this paper, although its contribution can be dominant in the case of materials with particularly high TCRs [17].

In Kohl et al.'s work [15], a model that implicitly takes into account the effects of the feedback on thermal noise was proposed. The limit of the approach proposed in [15] is, in our opinion, the use of an expression for the thermal noise voltage density that is valid only for electrical networks in perfect thermal equilibrium.

In this paper, we present an alternative noise model that starts from well-established assumptions on the very basic phenomena that generate current fluctuations in conductors and then applies the electrothermal feedback in a direct and rigorous way. Different noise expressions are found for both single hot wires and pairs of thermally coupled wires. Depending on the sign of the TCR and the type of biasing used for the wire (e.g., constant voltage or constant current), the model predicts significant modifications of the noise spectra with respect to the case of standard conductors, where the low thermal insulation prevents the development of significant self-heating, disrupting the quoted feedback mechanism. The main differences with respect to the previously proposed approach [15] are highlighted. This manuscript does not include experimental results but, on the other hand, intends to be a stimulus for the execution of
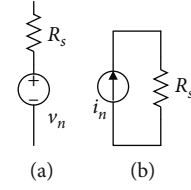

Figure 1: Thevenin (a) and Norton (b) representations of the noise in a resistor.

measurements that, if interpreted on the basis of the model prediction, could add useful information for the design of hot-wire sensors.

2. Electrothermal Model for Suspended Microwires

2.1. Noise in Wires out of Thermal Equilibrium. In thermal equilibrium, an electrical conductor will produce only thermal noise. In a Thevenin equivalent, a noiseless resistor is placed in series to a voltage noise source of PSD (Power Spectral Density) equal to $4k_B T R_S$, where k_B is the Boltzmann constant, T the absolute temperature, and R_S the conductor resistance. The Norton equivalent circuit consists of a noiseless resistor in parallel with a noise current source of PSD equal to $4k_B T G_S$, where $G = 1/R_S$. The two circuits are recalled in Figures 1(a) and 1(b). The first theoretical derivation of these noise models, developed by H. Nyquist using thermodynamic arguments, dates back to 1928.

Use of the above model to represent the noise in hot wires is not rigorous for two reasons. First, the voltage vs. current dependence (V-I curve) is not linear, due to self-heating and the relatively large TCR, so that defining the wire resistance is not straightforward. Second, a hot wire in operating conditions carries a nonzero electrical current and then is not in thermal equilibrium.

Let us start from the nonlinearity problem and consider Figure 2(a), where the V-I characteristics of a wire subjected to self-heating is sketched for the case of positive TCR.

For any given operating point, marked by current I and voltage V, we can define two resistances, namely, a large signal resistance, R, and a small-signal resistance, r_{DC}:

$$R = V/I, \tag{1}$$

$$r_{DC} = \left.\frac{dV}{dI}\right|_{I,V}. \tag{2}$$

As the current increases, so does the overheating and, due to the assumption of positive TCR, also R increases, producing the nonlinear behaviour of the V-I characteristic shown in Figure 2(a). On the other hand, r_{DC} is the small-signal equivalent resistance. This resistance is applicable for variations around the operating point that are either constant (dc components) or slow (low frequencies) so as to allow the overheating to follow the heating power. At high frequencies, the thermal mass of the wire dampens the temperature variations and the equivalent small-signal resistance asymptotically tends to R. In between, the magnitude of the small-
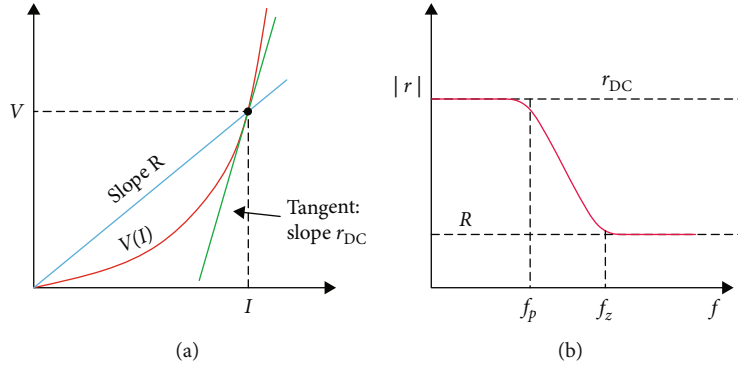
(a)

(b)

FIGURE 2: Sketched characteristics of a thermally insulated wire with positive TCR: (a) V-I plots; (b) magnitude of the small-signal impedance as a function of frequency.

signal (complex) impedance, indicated with r, should reasonably follow a bode plot like that depicted in Figure 2(b). The exact expression of the small-signal impedance, which is in agreement with this intuitive behaviour, was derived in a previous study [15], which deals with thermistor-based bolometers.

Since noise consists in small current and voltage variations around the operating point, the equivalent circuits of Figure 1 are applicable to the wire once R_s is replaced with the small-signal impedance r. What is less obvious is the expression of the spectral density to be assigned to v_n or i_n noise sources that appear in Figures 1(a) and 1(b), respectively, due to the mentioned nonequilibrium condition. It has been shown with either a semiclassical [18] or quantum mechanics [19] approach that the current fluctuation due to thermal agitation of the carriers has a spectral density that does not change when the conductor is subjected to a moderate dc current with respect to the case of thermal equilibrium. The reason is that the carrier drift velocity is much smaller than the thermal velocity in most practical cases of metallic conductors, so that the random walks of the carriers, from which the current fluctuation originates, are practically unaltered. These random walks depend on the same scattering mechanism from which the resistance R originates. Therefore, it is reasonable to consider that the current fluctuation has a spectral density equal to $4k_BT/R$. However, using this spectral density for the current source in the equivalent model of Figure 1(b) means neglecting the mentioned feedback effect that occurs in the hot wire. If the wire is biased with a constant voltage, a current change due to the random agitation of the carriers produces a variation of the heating power and, in turn, a change of the wire temperature and resistance R. The resulting resistance variation produces an additional current contribution that reinforces or diminishes the original current change depending on the sign of the TCR. Then, due to the wire self-heating, the actual current fluctuations seen from the wire terminals are different from those that would be predicted assigning the density $4k_BT/R$ to the current source in the circuit of Figure 1(b).

This electrothermal feedback effect was described in previous works on bolometers [15, 16], where the interest was mainly to model the effects on the device sensitivity. The feedback was also considered for its effect on thermal noise, and the authors simply propose to calculate the voltage noise power density as $4k_BT$ Re (r), where "Re (r)" indicates the real part of impedance r. This approach was demonstrated to be applicable to RLC (resistance, inductance, and capacitance) networks in thermal equilibrium, but there is no physical justification for use of it for out-of-equilibrium systems in the presence of electrothermal feedback.

The alternative approach proposed in this work starts from the following equation for the total current (I) through a conductor subjected to a voltage V, valid also in the presence of self-heating:

$$I = \frac{V}{R} - i_e \iff V = IR + Ri_e, \tag{3}$$

where i_e is the thermal noise component, marked by the usual spectral density $S_{IT} = 4k_BT/R$, and R is simply defined by the ratio V/I_{drift}, where I_{drift} is the current component due only to the electric field in the conductor. Notice that the temperature dependence of R is the cause of the electrothermal feedback. To complete the framework, we consider also that R is subjected also to random fluctuations that would be present also in the case of a perfectly constant temperature. These fluctuations, indicated with δR_e, are the cause of flicker noise and can be boosted by the feedback as thermal noise. These are the premises that will be used in the next subsections to derive a model of the noise in single hot wires and in thermally coupled pairs of hot wires. All the models used in this work are of the lumped-element type. Therefore, quantities such as the wire temperature will represent averages calculated along the wire length.

2.2. Electrothermal Model of a Single Hot Wire. Figure 3 schematically shows the elements of the single wire model.

In the electrical domain, the wire is represented by voltage V across its terminals and current I flowing through it. The two quantities are tied by the electrical resistance R, as shown by Equations (1) and (2). In the thermal domain, the wire is characterized by its absolute temperature T, by its thermal capacity C_{TH}, and by thermal conductivity θ from the wire to the environment, which is considered to be at
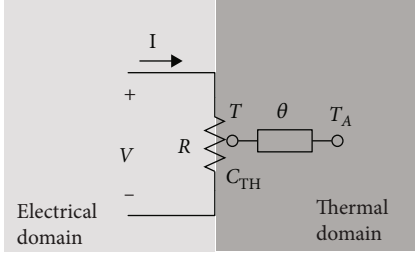
FIGURE 3: Elements of the electrothermal model for a single wire.

uniform temperature T_A. Thermal conductivity θ includes (i) heat conduction along the solid suspension elements, (ii) conduction and convection through the surrounding fluid, and (iii) radiation. We will consider that both R and θ are temperature-dependent quantities, while C_{TH} will be considered constant. Heat balance in the wire body will require that

$$C_{TH}\frac{dT}{dt} = W - \theta(T - T_A), \tag{4}$$

where W is the total heating power dissipated by the electrical current, simply given by

$$W = V \cdot I. \tag{5}$$

In order to calculate the effects of fluctuations i_e and δR_e, it is convenient to use a small-signal analysis of the wire around a static operating point (dc components). Then, we can write

$$\begin{aligned}
V &= V_0 + v, \\
I &= I_0 + i, \\
T &= T_0 + \delta T, \\
W &= W_0 + w,
\end{aligned} \tag{6}$$

where V_0, I_0, T_0, and $W_0 = V_0 I_0$ define the operating point (OP) and v, i, δT, and w are the corresponding variations around the OP. We use lower-case symbols for v, i, and w since it is customary in small-circuit analysis of electrical circuits. For all other variations, we have used the prefix "δ." Taking into account the temperature dependence of R and θ, their first-order approximations can be written as

$$\begin{aligned}
R &= R_0 + \alpha R_0 \delta T + \delta R_e, \\
\theta &= \theta_0 + \beta \theta_0 \delta T \text{ with } \alpha = \frac{1}{R}\frac{dR}{dT}, \\
\beta &= \frac{1}{\theta}\frac{d\theta}{dT},
\end{aligned} \tag{7}$$

where we have included also possible temperature independent fluctuations (δR_e) of R. Note that α is the TCR of the wire. Thermal equilibrium in the OP requires

$$W_0 = I_0 V_0 = \theta_0(T_0 - T_A). \tag{8}$$

With the above definitions, the following equation for variations in the Laplace domain can be derived from Equation (4):

$$sC_{TH}\delta T = w - \beta\theta_0(T - T_A)\delta T - \theta_0\delta T, \tag{9}$$

from which we find

$$\delta T = \gamma(s)w, \tag{10}$$

$$\gamma(s) = \frac{\gamma_0}{1 + s/\omega_g}, \tag{11}$$

$$\gamma_0 = \frac{1}{\theta_0[1 + \beta(T - T_A)]}, \tag{12}$$

$$\omega_g = \frac{1}{C_{TH}\gamma_0}. \tag{13}$$

In terms of variations, Equations (3) and (5) become

$$v = iR_0 + (\alpha R_0 \delta T + \delta R_e)I_0 + R_0 i_e, \tag{14}$$

$$w = iV_0 + vI_0. \tag{15}$$

Combining Equations (10)–(15), we can find with elementary algebraic passages

$$v = iR_0\frac{1 + \alpha V_0 I_0 \gamma(s)}{1 - \alpha R_0 I_0^2 \gamma(s)} + \frac{R_0}{1 - \alpha R_0 I_0^2 \gamma(s)}i_e + \frac{I_0}{1 - \alpha R_0 I_0^2 \gamma(s)}\delta R_e, \tag{16}$$

which can be synthetically written in the following way:

$$v = i \cdot r + i_e \cdot r_e + k_R \delta R_e, \tag{17}$$

where coefficients r, r_e, and k_R depend on the complex frequency s. This dependence can be made more explicit, by substituting the expression of $\gamma(s)$ from Equation (11) into Equation (16) obtaining

$$r = R_0\frac{1 + \alpha V_0 I_0 \gamma_0}{1 - \alpha V_0 I_0 \gamma_0} \cdot \frac{1 + s/\omega_z}{1 + s/\omega_p}, \tag{18}$$

$$r_e = R_0\frac{1}{1 - \alpha V_0 I_0 \gamma_0} \cdot \frac{1 + s/\omega_g}{1 + s/\omega_p}, \tag{19}$$

$$k_R = \frac{I_0}{1 - \alpha V_0 I_0 \gamma_0} \cdot \frac{1 + s/\omega_g}{1 + s/\omega_p}, \tag{20}$$

where the following angular frequencies have been introduced:

$$\omega_z = \omega_G(1 + \alpha W_0 \gamma_0), \tag{21}$$

$$\omega_p = \omega_G(1 - \alpha W_0 \gamma_0). \tag{22}$$

Equations (17)–(22) can be used to describe the small-signal behaviour of the wire. As far as the small-signal ac impedance of the wire is concerned, this is given by

parameter r. It can be easily shown that for a positive TCR, the magnitude of r depends on the frequency as in Figure 2(b), with $f_p = \omega_p/2\pi$ and $f_z = \omega_z/2\pi$. An equivalent expression was found in [15].

Equation (17) can be used to find Thevenin and Norton representations of the wire noise. Referring to Figures 1(a) and 1(b), obviously, we have to replace resistor R_S with the complex impedance r in both the Thevenin and Norton circuits, in order to correctly model the ac behaviour of the wire. In the case of the Thevenin equivalent circuit, the voltage of the equivalent source (V_n in Figure 1(a)) can be calculated by nulling the small-signal current through the wire terminals (i.e., we set $i = 0$ in Equation (17)). This represents the case of a wire biased with a constant current (zero variations). Then, the PSD of the Thevenin equivalent noise source is given by

$$S_{vn} = 4k_B \frac{T_0}{R_0} |r_e|^2 + S_{\delta R_e}(f)|k_R|^2, \qquad (23)$$

where $S_{\delta R_e}$ is the PSD of resistance fluctuations δR_e, while the PSD of i_e was assumed to be equal to $4k_B T_0/R_0$ as anticipated in the previous subsection. At high frequency, r_e tends to R_0, so that the thermal noise voltage contribution is simply $4k_B T_0 R_0$. Since also the complex impedance of the wire tends to R_0, the high-frequency limit simply corresponds to calculating the noise PSD using the usual Johnson-Nyquist expression. At very low frequencies ($f \ll f_p$), the thermal component of the voltage PSD becomes

$$S_{vn-th} = 4k_B T_0 R_0 \left| \frac{1}{1 - \alpha V_0 I_0 \gamma_0} \right|^2. \qquad (24)$$

For a positive TCR ($\alpha > 0$), the denominator can approach zero when the static heating power $W_0 = V_0 I_0$ is large enough. In that case, the voltage noise PSD can get much larger than the high-frequency limit. It can be easily verified that the low-frequency limit given by Equation (24) does not coincide with the value obtained by applying the Jonson-Nyquist expression with the low-frequency limit of the wire resistance (r_{DC}) given by Equation (18) for $s = 0$.

A similar boosting effect can be observed for the flicker component, represented by the resistance fluctuation component. At high frequency, k_R tends to I_0, so that the voltage noise is simply given by the product of the resistance fluctuations and the bias current I_0. At low frequency, this term is boosted by the same factor as the thermal noise.

The noise voltage density of the Thevenin model represents the actual noise that should be expected when the wire is biased at constant current. It is interesting to observe that the boosting factor tends to infinity when $\alpha V_0 I_0 \gamma_0$ tends to one. If $\alpha V_0 I_0 \gamma_0$ gets larger than one, the pole $s_p = -\omega_p$ in the denominator of both r_e and k_R becomes positive, denoting instability. In these conditions, a small variation due to noise
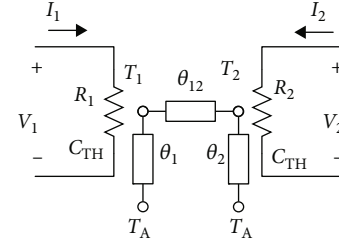

FIGURE 4: Elements of the electrothermal model for a thermally coupled wire pair.

triggers a catastrophic increase of the voltage, leading to failure. This phenomenon is the well-known thermal runaway. It is possible to find a notable expression for $\alpha V_0 I_0 \gamma_0$ when thermal conductance θ is assumed to be independent of temperature ($\beta = 0$). In that case, $\gamma_0 = 1/\theta_0$ and $\alpha V_0 I_0 \gamma_0 = \alpha(T_0 - T_A)$. As a result, the noise-boosting factor $(1 - \alpha V_0 I_0 \gamma_0)^{-1}$ tends to infinity when the product of the wire overheating $(T_0 - T_A)$ by the TCR tends to one. Thermal runaway occurs when this product is equal to or greater than one. For a negative TCR, Equation (24) predicts a noise reduction at low frequencies with respect to the $4k_B T_0 R_0$ limit and no thermal runaway.

The situation is reversed for the Norton equivalent model. The noise current source of the Norton model gives the current fluctuations when the wire is biased at constant voltage. Its value can be found setting $v = 0$ in Equation (17) and solving for current variations i, finding

$$i_n = -i = \frac{r_e}{r} i_e + \frac{k_R}{r} \delta R_e. \qquad (25)$$

Ratios r_e/r and k_R/r are now marked by a pole equal to $-\omega_z$. Instability, i.e., thermal runaway, occurs when the TCR is negative. This is a well-known difference between constant-current and constant-voltage biasing. Similarly, current noise boosting at low frequency occurs only for $\alpha < 0$. In particular, the thermal component of the noise current PSD in the low-frequency limit that can be found from Equation (25) is

$$S_{in-th} = 4k_B \frac{T_0}{R_0} \left| \frac{1}{1 + \alpha V_0 I_0 \gamma_0} \right|^2, \qquad (26)$$

where $4k_B(T_0/R_0)$ is the high-frequency limit which coincides with the PSD of the current fluctuation i_e that appears in Equation (1).

2.3. Electrothermal Model of Two Thermally Coupled Wires.
The elements of the model used for the pair of thermally coupled wires are illustrated in Figure 4.

The thermal and electrical quantities (V, I, R, T, and θ) are duplicated and an additional coupling thermal conductance θ_{12} is present. In this study, we assume that the system is symmetrical (the two wires are symmetrical) and are biased

in such a way that they reach a symmetrical OP, which is defined by the following values for the quantities of interest:

$$
\begin{aligned}
V_1 = V_2 = V_0, \\
I_1 = I_2 = I_0, \\
T_1 = T_2 = T_0, \\
R_1 = R_2 = R_0, \\
\theta_1 = \theta_2 = \theta_0.
\end{aligned}
\tag{27}
$$

In the majority of applications, thermally coupled wires are biased with a symmetrical operating point. On the other hand, variations are different between the two wires, so that the total values (OP plus variations) of the key quantities will be different from one wire to the other.

Equation (4), pertinent to a single wire, is replaced by the following set:

$$
\begin{cases}
C_{TH} \dfrac{dT_1}{dt} = W_1 - \theta_1(T_1 - T_A) - \theta_{12}(T_1 - T_2), \\[2mm]
C_{TH} \dfrac{dT_2}{dt} = W_2 - \theta_2(T_2 - T_A) + \theta_{12}(T_1 - T_2).
\end{cases}
\tag{28}
$$

In Equation (28), a heat exchange term due to conductance θ_{12} is clearly present. In terms of variations and Laplace transforms, we obtain

$$
\begin{cases}
sC_{TH}\delta T_1 = w_1 - [\theta_0 + \beta\theta_0(T_0 - T_A)]\delta T_1 - \theta_{12}(\delta T_1 - \delta T_2), \\[2mm]
sC_{TH}\delta T_2 = w_2 - [\theta_0 + \beta\theta_0(T_0 - T_A)]\delta T_2 + \theta_{12}(\delta T_1 - \delta T_2).
\end{cases}
\tag{29}
$$

Heat generation in the wires is described by the following set:

$$
\begin{cases}
w_1 = v_1 I_0 + i_1 V_0, \\
w_2 = v_2 I_0 + i_2 V_0,
\end{cases}
\tag{30}
$$

while Equation (14) (Ohm's law plus Jonson-Nyquist current fluctuations) for the two wires is replaced by the following set:

$$
\begin{cases}
I_1 = \dfrac{V_1}{R_1} - i_{e1}, \\[2mm]
I_2 = \dfrac{V_2}{R_2} - i_{e2},
\end{cases}
\iff
\begin{cases}
V_1 = I_1 R_1 + R_1 i_{e1}, \\[2mm]
V_2 = I_2 R_2 + R_2 i_{e2},
\end{cases}
\tag{31}
$$

which, in terms of variations, becomes

$$
\begin{cases}
v_1 = i_1 R_0 + \alpha R_0 I_0 \delta T_1 + I_0 \delta R_{e1} + R_0 i_{e1}, \\
v_2 = i_2 R_0 + \alpha R_0 I_0 \delta T_2 + I_0 \delta R_{e2} + R_0 i_{e2}.
\end{cases}
\tag{32}
$$

At this point, it is convenient to separate all variations into a differential mode and common mode component. For example, we will replace v_1 and v_2 by $v_d = v_1 - v_2$

and $v_c = (v_1 + v_2)/2$, respectively, where v_d is the differential component and v_c the common mode one. In the remainder of this document, differential mode and common mode quantities will be indicated with the "d" and "c" subscript, respectively. In this way, we can easily find decoupled equations for the differential mode and common mode variables. For the common mode components, the resulting equations are identical to those of the single wire. This is reasonable, since common mode components do not break the symmetry, and with no temperature difference, the two wires do not interact and behave as a single wire. Equations for the differential components are only slightly different, due to the presence of θ_{12}, so that from the Equation set (29), we can derive the following differential mode equation:

$$
sC_{TH}\delta T_d = w_d - [\theta_0 + \beta\theta_0(T_0 - T_A)]\delta T_d - 2\theta_{12}\delta T_d, \tag{33}
$$

while from the Equation sets (30) and (32), we find differential mode equations that are identical to Equations (14) and (15), respectively:

$$
\begin{cases}
v_d = i_d R_0 + \alpha R_0 I_0 \delta T_d + I_0 \delta R_{ed} + R_0 i_{ed}, \\
w_d = v_d I_0 + i_d V_0.
\end{cases}
\tag{34}
$$

From Equation (33), we can find the expression of δT_d, analogous to Equation (10):

$$
\delta T_d = \gamma_d(s)w_d, \tag{35}
$$

$$
\gamma_d(s) = \frac{\gamma_{0d}}{1 + s/\omega_{gd}}, \tag{36}
$$

$$
\gamma_{0d} = \frac{1}{\theta_0[1 + \beta(T_0 - T_A)] + 2\theta_{12}}, \tag{37}
$$

$$
\omega_{gd} = \frac{1}{C_{TH}\gamma_{0d}}. \tag{38}
$$

Since Equations (34)–(38) are formally equivalent to the equations of the single wire, with the sole difference of the expression of γ_{0d} (that replaces γ_0), the solution has the same form as Equation (17):

$$
v_d = i_d \cdot r_d + i_{ed} \cdot r_{ed} + k_{Rd}\delta R_{ed}, \tag{39}
$$

where

$$
\begin{cases}
r_d = R_0 \dfrac{1 + \alpha V_0 I_0 \gamma_{0d}}{1 - \alpha V_0 I_0 \gamma_{0d}} \cdot \dfrac{1 + s/\omega_{zd}}{1 + s/\omega_{pd}}, \\[3mm]
r_{ed} = R_0 \dfrac{1}{1 - \alpha V_0 I_0 \gamma_{0d}} \cdot \dfrac{1 + s/\omega_{gd}}{1 + s/\omega_{pd}}, \\[3mm]
k_{Rd} = \dfrac{I_0}{1 - \alpha V_0 I_0 \gamma_{0d}} \cdot \dfrac{1 + s/\omega_{gd}}{1 + s/\omega_{pd}}, \\[3mm]
\omega_{zd} = \omega_{gd}(1 + \alpha W_0 \gamma_{0d}), \\[1mm]
\omega_{pd} = \omega_{gd}(1 - \alpha W_0 \gamma_{0d}).
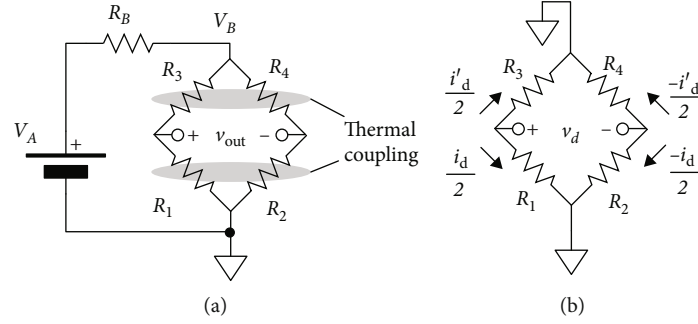\end{cases}
\tag{40}
$$

Figure 5: (a) Wheatstone bridge formed by two thermally coupled wire pairs; (b) equivalent circuit for differential mode variations.

In order to explain the way to use Equation (39) in a practical case, we can consider the very common situation in which the wires are biased with identical constant currents and the output signal is the voltage difference $v_d = v_1 - v_2$. In the next subsection, we will analyse the more complex case of a full Wheatstone bridge. With constant-current bias, both i_1 and i_2 are forced to be zero and then also i_d is zero. The forcing terms, i.e., Jonson-Nyquist current fluctuations i_{e1} and i_{e2} and resistance fluctuations δR_{e1} and δR_{e2}, are split into their common mode and differential mode components. Thanks to linearity of the small-signal equations and the fact that the equations are decoupled, we can calculate the effects of the two modes separately and then add them up. Common mode forcing terms produce only common mode variations, thus the effect on $v_{out} = v_d$ is null. Therefore, we can focus only on the differential mode terms. From Equation (39) with $i_d = 0$ and considering that i_{e1}, i_{e2}, δR_{e1}, and δR_{e2} are independent stochastic processes, we can find the PSD of the output voltage:

$$S_{vd}(f) = 2S_{ie}(f)|r_{ed}|^2 + 2S_{\delta Re}|k_{Rd}|^2, \tag{41}$$

where $S_{ie}(f) = 4k_B(T_0/R_0)$ and $S_{\delta Re}(f)$ are the PSD of the Johnson-Nyquist (thermal) current fluctuations and resistance fluctuations, respectively, of each single wire. Again, as in the case of the single wire, a boosting effect of both thermal and flicker noise at low frequencies is predicted if the TCR is positive. For the same heating power ($V_0 I_0$) and then the same overheating, we can expect a smaller noise increase with respect to the case of the single wire, due to the presence of the additional coupling term θ_{12} in γ_{0d}, compared to γ_0 of the single wire.

2.4. Noise in Wheatstone Bridges of Thermally Coupled Wire Pairs. Often, thermally coupled wire pairs are connected to form Wheatstone bridges as shown in Figure 5(a), where the two wire pairs are represented by resistors pairs R_1 and R_2 and R_3 and R_4. Since the aim is generally to sense a physical quantity, connection should be made in such a way that the effect of the quantity of interest contributes to the output voltage in a constructive way. The bridge can be biased with different approaches, which are all equivalent in terms of the effect of noise on the output voltage. In the example of Figure 5, the bridge is biased by a dc voltage source V_A (e.g., a battery) and a resistor R_B, which forms a voltage

divider with the bridge resistance setting the operating voltage of the bridge to V_B.

The equivalent circuit for differential mode variations is represented in Figure 5(b), where the differential currents of the two wire pairs are indicated. Equation (39) for the two wire pairs becomes

$$\begin{cases} v_d = i_d \cdot r_d + i_{ed} \cdot r_{ed} + k_{Rd}\delta R_{ed}, \\ v_d' = i_d' \cdot r_d + i_{ed}' \cdot r_{ed} + k_{Rd}\delta R_{ed}', \end{cases} \tag{42}$$

where variables with a prime character v_d', i_d', i_{ed}', and $\delta R_{ed}'$ belong to the upper wire pair of the bridge (R_3, R_4). By elementary analysis of the circuit in Figure 5(b), it is possible to find that $v_d' = v_d$ and $i_d' = -i_d$. Solving Equation set (42) with these relationships gives

$$2v_d = \left(i_{ed} - i_{ed}'\right) \cdot r_{ed} + k_{Rd}\left(\delta R_{ed} - \delta R_{ed}'\right). \tag{43}$$

Considering that i_{ed}, i_{ed}', δR_{ed}, and $\delta R_{ed}'$ can be reasonably considered independent stochastic processes, and recalling the dependence of each one of these quantities with current fluctuations (i_e) and resistance fluctuations (δR_e) of the single wires of the bridge, we can finally find

$$S_{vd}(f) = S_{ie}(f)|r_{ed}|^2 + S_{\delta Re}|k_{Rd}|^2, \tag{44}$$

where, again, $S_{ie}(f) = 4k_B T/R_0$. Equation (44) indicates that the output noise PSD of a Wheatstone bridge is subjected to noise-boosting effects caused by overheating and that this effect is characterized by the differential mode parameters r_{ed} and k_{Rd}.

2.5. Determination of the Main Parameters. In order to utilize the proposed model to predict the output noise of single hot wires or arrangements of thermally coupled wires, it is necessary to find the system parameters. Referring to Equation set (18), it is possible to estimate all required parameters of a single wire by measuring the small-signal impedance (r) as a function of frequency. Fitting the response by means of a bilinear (one pole, one zero) function, it is possible to find ω_p and ω_z. From these two singularities, we can find ω_g and the $\alpha V_0 I_0 \gamma_0$ term. By these four quantities, it is possible to calculate coefficients r, r_e, and k_R as a function of
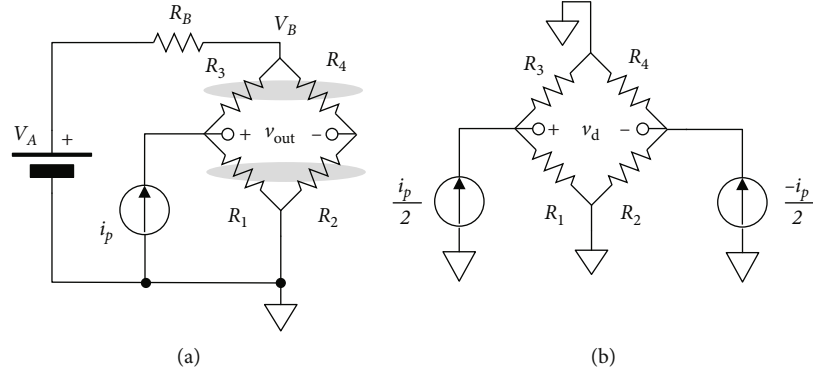
(a)   (b)

FIGURE 6: (a) Simulation of a Wheatstone bridge to calculate the differential mode parameters; (b) equivalent circuit for differential mode variations.

frequency (see Equation (18)). Measurements have to be performed by biasing the wire in the desired OP. To complete determination of the quantities present in Equation (17), it is also necessary to measure the spectrum of the resistance fluctuations ($S_{\delta Re}$) at different temperatures, by placing the wire in an oven to set the desired temperature without resorting to self-heating in order to avoid the mentioned noise-boosting effect.

The same parameters of a set of thermally coupled wires connected to form a Wheatstone bridge can be measured again from a single frequency sweep, using a current source i_p as in Figure 6(a).

Source i_p should have zero dc value and a sinusoidal ac component small enough to induce only a small displacement of the current and voltage of the bridge around the OP. Since we have demonstrated that only differential mode components contribute to the output PSD of the bridge, we can analyse only the differential mode equivalent circuit of Figure 6(b) where we can easily find that $i_d + i_d{'} = i_p$. Solving Equation set (42) with this condition and neglecting the noise components, we get

$$r_d = \frac{2v_d}{i_p}. \tag{45}$$

Sweeping the frequency of the source i_p and measuring voltage v_d, it is possible to use Equation (45) to calculate the frequency response of r_d from which the main parameters of the differential mode model can be determined.

3. Results and Discussion

In this section, we compare the predictions of our model with respect to those that can be obtained from the approach proposed in [15]. The comparison will be limited to the boosting factor of the thermal noise, since no effects of the electrothermal feedback on the flicker noise were proposed in the previous work.

Figure 7 shows the noise voltage PSD of the thermal noise, normalized with respect to the high-frequency limit. Note that this limit is the same for the two models and is
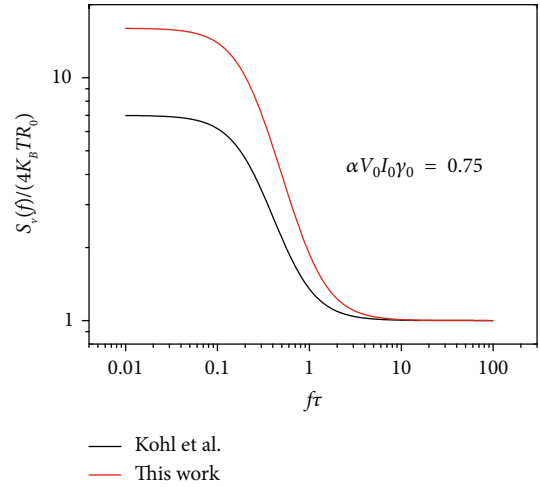

FIGURE 7: Calculated thermal noise PSD as a function of frequency, normalized to the high-frequency limit, for the proposed model and for the expression given in reference [15].

equal to $4k_B T_0 R_0$, where R_0 is the wire resistance (V/I) ratio at the operating temperature. Both curves have been calculated for a value of parameter $\alpha V_0 I_0 \gamma_0$ equal to 0.75. We recall here that in [15], the noise density is simply assumed to be $4k_B T_0 \operatorname{Re}(r)$, while in the proposed model, the PSD is given by $4k_B (T_0/R_0)|r_e|^2$ (see the thermal component in Equation (23)). Figure 7 clearly shows that the two models predict a similar frequency behaviour but with noise boosting occurring at low frequencies which is significantly larger for the proposed model.

The dependence of the noise-boosting factor, $S_v(0)/S_v(\infty)$ on the parameter $\alpha V_0 I_0 \gamma_0$ is shown in Figure 8 for the two models. Negative values of $\alpha V_0 I_0 \gamma_0$ occur for negative values of the TCR. In both models, thermal noise is boosted at low frequencies for $\alpha > 0$ and reduced for $\alpha < 0$, but the extent of this effect is different in the two cases. The proposed model predicts more noise boosting for $\alpha > 0$ and less noise reduction for $\alpha < 0$ than the model in [15], for which the noise PSD tends to zero when $\alpha V_0 I_0 \gamma_0$ approaches -1.
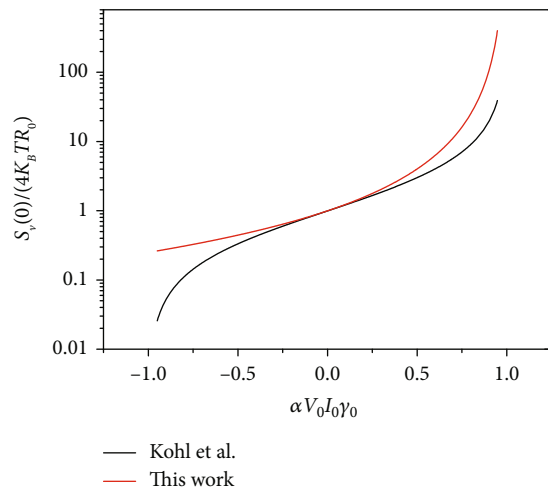
FIGURE 8: Ratio of the thermal noise PSD at 0 Hz (dc) over the high-frequency limit as a function of parameter $\alpha V_0 I_0 \gamma_0$, for the proposed model and for the model in reference [15].

Figures 7 and 8 demonstrate that the proposed model gives results that are significantly different from the previous model, and this enables discrimination between the two by means of noise measurements.

4. Conclusions

The analysis presented in this paper predicts in a quantitative way that the electrothermal feedback, resulting from the combination of self-heating with a nonzero TCR, changes the noise spectral density of a conducting wire. Both thermal noise and flicker noise are affected by a filtering effect that, depending on the sign of the TCR, boosts or dampens the noise density at low frequencies. This effect was already suggested in a previous work [15], where, however, an arbitrary assumption was made on the expression of the thermal noise PSD. The proposed model derives the thermal noise PSD with straightforward passages, starting from well-established properties of the thermal current fluctuations, and, in addition, is capable of predicting the effect also on the flicker noise spectrum. The approach is extended to pairs of thermally coupled wires, which constitute the core of thermal flow sensors and, more recently, have been proven capable of detecting acoustic particle velocity. In the proposed model, the filtering effect is characterized by parameters that can be easily determined by means of small-signal impedance measurements as a function of frequency.

Calculations of the thermal PSD performed using the proposed model and the previous approach revealed that the two models yield significantly different predictions of the noise modification occurring at low frequency. This should facilitate discriminating the two models through noise measurements, considering also that in both cases, the model parameters can be easily determined by means of small-signal impedance measurements as a function of frequency. These experiments should contribute to widen the knowledge of noise in out-of-equilibrium electrical systems.

Data Availability

The data used to support the findings of this study are included within the article.

Conflicts of Interest

The authors declare that there is no conflict of interest regarding the publication of this paper.

References

[1] J.-S. Shie, B. C. S. Chou, and Y.-M. Chen, "High performance Pirani vacuum gauge," *Journal of Vacuum Science & Technology A: Vacuum, Surfaces, and Films*, vol. 13, no. 6, pp. 2972–2979, 1995.

[2] P. Sturesson, L. Klintberg, and G. Thornell, "Pirani microgauge fabricated of high-temperature co-fired ceramics with integrated platinum wires," *Sensors and Actuators A: Physical*, vol. 285, pp. 8–16, 2019.

[3] J. Ruellan, J. Arcamone, D. Mercier, C. Dupré, and L. Duraffourg, "Pirani gauge based on alternative self-heating of silicon nanowire," in *2013 Transducers & Eurosensors XXVII: The 17th International Conference on Solid-State Sensors, Actuators and Microsystems (TRANSDUCERS & EUROSENSORS XXVII*, pp. 2568–2571, Barcelona, Spain, June 2013.

[4] A. Mahdavifar, M. Navaei, P. J. Hesketh, M. Findlay, J. R. Stetter, and G. W. Hunter, "Transient thermal response of micro-thermal conductivity detector (μTCD) for the identification of gas mixtures: an ultra-fast and low power method," *Microsystems & Nanoengineering*, vol. 1, no. 1, article 15025, 2015.

[5] A. Vatani, P. L. Woodfield, and D. V. Dao, "A miniaturized transient hot-wire device for measuring thermal conductivity of non-conductive fluids," *Microsystem Technologies*, vol. 22, no. 10, pp. 2463–2466, 2016.

[6] J. Chen and C. Liu, "Development and characterization of surface micromachined, out-of-plane hot-wire anemometer," *Journal of Microelectromechanical Systems*, vol. 12, no. 6, pp. 979–988, 2003.

[7] K. Kokmanian, S. Scharnowski, M. Bross et al., "Development of a nanoscale hot-wire probe for supersonic flow applications," *Experiments in Fluids*, vol. 60, no. 10, p. 150, 2019.

[8] B. Idjeri, M. Laghrouche, and J. Boussey, "Wind measurement based on MEMS micro-anemometer with high accuracy using ANN technique," *IEEE Sensors Journal*, vol. 17, no. 13, pp. 4181–4188, 2017.

[9] H.-E. de Bree, H. V. Jansen, T. S. J. Lammerink, G. J. M. Krijnen, and M. Elwenspoek, "Bi-directional fast flow sensor with a large dynamic range," *Journal of Micromechanics and Microengineering*, vol. 9, no. 2, pp. 186–189, 1999.

[10] H.-E. de Bree, P. Leussink, T. Korthorst, H. Jansen, T. S. J. Lammerink, and M. Elwenspoek, "The μ-flown: a novel device for measuring acoustic flows," *Sensors and Actuators A: Physical*, vol. 54, no. 1-3, pp. 552–557, 1996.

[11] O. Pjetri, R. J. Wiegerink, and G. J. Krijnen, "A 2D particle velocity sensor with minimal flow-disturbance," *IEEE Sensors Journal*, vol. 16, pp. 8706–8714, 2016.

[12] M. Piotto, F. Butti, E. Zanetti, A. Di Pancrazio, G. Iannaccone, and P. Bruschi, "Characterization and modeling of CMOS-compatible acoustical particle velocity sensors for applications

requiring low supply voltages," *Sensors and Actuators A: Physical*, vol. 229, pp. 192–202, 2015.

[13] M. Piotto, A. Ria, D. Stanzial, and P. Bruschi, "Design and characterization of acoustic particle velocity sensors fabricated with a commercial post-CMOS MEMS process," in *2019 20th International Conference on Solid-State Sensors, Actuators and Microsystems & Eurosensors XXXIII (TRANSDUCERS & EUROSENSORS XXXIII*, pp. 1839–1842, Germany, June 2019.

[14] N. R. Krishnaprasad, M. Contino, S. P. Chepuri, D. F. Comesana, and G. Leus, "DOA estimation and beamforming using spatially under-sampled AVS arrays," in *2017 IEEE 7th International Workshop on Computational Advances in Multi-Sensor Adaptive Processing (CAMSAP)*, pp. 1–5, Netherlands Antilles, December 2017.

[15] F. Kohl, F. Keplinger, A. Jachimowicz, and J. Schalko, "A model of metal film resistance bolometers based on the electro-thermal feedback effect," *Sensors and Actuators A: Physical*, vol. 115, no. 2-3, pp. 308–317, 2004.

[16] H. Neff, A. M. N. Lima, G. S. Deep et al., "Nonlinearity and electrothermal feedback of high T_c transition edge bolometers," *Applied Physics Letters*, vol. 76, no. 5, pp. 640–642, 2000.

[17] H. Neff, I. A. Khrebtov, A. D. Tkachenko et al., "Noise, bolometric performance and aging of thin high T_c superconducting films on silicon membranes," *Thin Solid Films*, vol. 324, no. 1-2, pp. 230–238, 1998.

[18] A. Ambrozy, *Electronic Noise*, McGraw-Hill, New-York, 1982.

[19] A. J. Dekker, H. Hickman, and T. M. Chen, "A tutorial approach to the thermal noise in metals," *American Journal of Physics*, vol. 59, no. 7, pp. 609–614, 1991.